

**NUMERICAL ANALYSIS OF HEAT CONDUCTION AND POTENTIAL
FLOW PROBLEMS OVER A SPHERE AND A 3- DIMENSIONAL
PROLATE SPHEROIDAL BODY**

M.Sc. Thesis by

Onur ÖLMEZ, B.Sc.

Department: Ocean Engineering

Programme: Ocean Engineering

Supervisor : Assist. Prof. Şafak Nur Ertürk

JUNE 2008

**NUMERICAL ANALYSIS OF HEAT CONDUCTION AND POTENTIAL
FLOW PROBLEMS OVER A SPHERE AND A 3- DIMENSIONAL
PROLATE SPHEROIDAL BODY**

M.Sc. Thesis by

Onur ÖLMEZ, B.Sc.

(508051107)

Date of submission : 21 April 2008

Date of defence examination: 10 June 2008

Supervisor (Chairman): Assist. Prof. Şafak Nur ERTÜRK (I.T.U)

Members of the Examining Committee: Prof. Dr. Ömer GÖREN (I.T.U)

Prof. Dr. Serdar BEJİ (I.T.U)

JUNE 2008

İSTANBUL TEKNİK ÜNİVERSİTESİ ★ FEN BİLİMLERİ ENSTİTÜSÜ

**KÜRESEL VE 3 BOYUTLU PROLAT KÜRESEL GÖVDE ÇEVRESİNDE
ISI TRANSFERİ VE POTANSİYEL AKIŞ PROBLEMLERİNİN
NUMERİK ANALİZİ**

YÜKSEK LİSANS TEZİ

Müh. Onur ÖLMEZ

(508051107)

Tezin Enstitüye Verildiği Tarih : 21 Nisan 2008

Tezin Savunulduğu Tarih : 10 Haziran 2008

Tez Danışmanı : Yrd. Doç. Dr. Şafak Nur ERTÜRK (İ.T.Ü.)

Diğer Jüri Üyeleri: Prof. Dr. Ömer GÖREN (İ.T.Ü.)

Prof. Dr. Serdar BEJİ (İ.T.Ü.)

HAZİRAN 2008

ACKNOWLEDGEMENTS

I would like to thank to my advisor Assist. Prof. Şafak Nur ERTÜRK who supported me to complete this study and illuminated me whenever I encountered with problems. I would also wish to thank to my friends for sophisticated discussions. Of course, special appreciation goes to my parents who provide me such a special life and never quit supporting me whatever I do.

Onur ÖLMEZ

May/2008

CONTENTS

ACKNOWLEDGEMENT	ii
ABBREVIATIONS	v
LIST OF TABLES	vii
LIST OF FIGURES	viii
LIST OF SYMBOLS	xi
ÖZET	xii
SUMMARY	xiii
1. INTRODUCTION	1
2. MATHEMATICAL MODELING AND NUMERICAL METHODS IN SPHERICAL COORDINATES	5
2.1 The Jakobi Iteration Method	7
2.2 Gauss Seidel Iteration Method	9
2.3 Successive Over Relaxation	10
2.4 The Alternating Direction Implicit (ADI) Method	11
3. MATHEMATICAL MODELLING IN PROLATE SPHERICAL COORDINATE SYSTEM	20
4. GRID GENERATION	23
4.1 General Methods	24
4.2 Forming Computational Domain	26
5. COMPUTATIONAL RESULTS	33
5.1 Solution of Heat Equation in Spherical Coordinates	33
5.2. Solution of Heat Equation in Prolate Spheroidal Coordinates	39
5.3. Solution of 3-D Potential Flow in Spherical Coordinates	43
5.4. Solution of 3-D Potential Flow in Prolate Spheroidal Coordinates	54
6. COMPARISOF RESULTS	64
6.1. In House Code versus Fluent and Symlab for a Sphere	64
6.2. In House Code versus Fluent and Symlab for Prolate Spheroidal Body	70
6.3 Comparison of In-House Code Results for Different Grid Densities	74
7. CONCLUSIONS	77
REFERENCES	79
APPENDICES	81
A Theoretical Pressure Coefficient Variation	81

B Node Number, Error, Computational Time Graphs	82
C Comparative Cp Presentation of Sphere Results	84
CURRICULUM VITAE	85

ABBREVIATIONS

GRAD	: Gradient
ADI	: Alternating Direction Implicit
ADIE	: ADI coefficient at geographic east
ADIL	: ADI coefficient at geographic lower position
ADIN	: ADI coefficient at geographic north
ADIP	: ADI coefficient at point
ADIS	: ADI coefficient at geographic south
ADIU	: ADI coefficient at geographic upper position
ADIW	: ADI coefficient at geographic west
CFD	: Computational Fluid Dynamics
G-S	: Gauss-Seidel
GSE	: Gauss-Seidel coefficient at geographic east
GSL	: Gauss-Seidel coefficient at geographic lower position
GSN	: Gauss-Seidel coefficient at geographic north
GSP	: Gauss-Seidel coefficient at point
GSS	: Gauss-Seidel coefficient at geographic south
GSU	: Gauss-Seidel coefficient at geographic upper position
GSW	: Gauss-Seidel coefficient at geographic west
NR	: Number of Nodes in r-ordinate
NPHI	: Number of Nodes in ϕ -ordinate
NTHETA	: Number of Nodes in θ -ordinate
PE	: Prolate Gauss-Seidel coefficient at geographic east
PL	: Prolate Gauss-Seidel coefficient at geographic lower position
PN	: Prolate Gauss-Seidel coefficient at geographic north
PP	: Prolate Gauss-Seidel coefficient at point
PS	: Prolate Gauss-Seidel coefficient at geographic south
PU	: Prolate Gauss-Seidel coefficient at geographic upper position
PW	: Prolate Gauss-Seidel coefficient at geographic west
JE	: Jakobi coefficient at geographic east
JL	: Jakobi coefficient at geographic lower position
JN	: Jakobi coefficient at geographic north
JP	: Jakobi coefficient at point
JS	: Jakobi coefficient at geographic south
JU	: Jakobi coefficient at geographic upper position
JW	: Jakobi coefficient at geographic west
RANS	: Reynolds-Avaraged Navier Stokes
FDM	: Finite Difference Method
FEM	: Finite Element Method
BEM	: Boundary Element Method
FVM	: Finite Volume Method
Cp	: Pressure Coefficient
DDR	: Double Data Rate

RAM : Random Access Memory
AIAA : American Institute of Aeronautics and Astronautics
DFVLR : Deutsche Forschungs- und Versuchsanstalt für Luft- und Raumfahrt
(German Research & Development Institute for Air & Space Travel)
3-D : Three Dimensional
2-D : Two Dimensional
PDE : Partial Differential Equation
BC : Boundary Condition

LIST OF TABLES

	<u>Page Number</u>
Table 6.1 : Sphere Flow Results Comparison for Different Grid Densities.....	74
Table A.1 : Angle-Theoretical Pressure Coefficient Variation Datas.....	81

LIST OF FIGURES

	<u>Page Number</u>
Figure 2.1 : 2-D View of the Coefficient Notation.....	8
Figure 2.2 : Gauss-Seidel Iteration Schema.....	9
Figure 2.3 : Schematical View of ADI x-direction sweep.....	12
Figure 2.4 : Schematical View of ADI x-direction sweep	14
Figure 2.5 : 2-D View of 7x3 Grid.....	17
Figure 4.1 : Transformation of coordinate systems.....	24
Figure 4.2 : Form-Fitted Grid Example (Blazek 2001. p.31).....	24
Figure 4.3 : Cartesian Grid Example (Blazek 2001. p.31).....	25
Figure 4.4 : Spherical Coordinate's Projection (Thomas 1998. p.534).....	27
Figure 4.5 : 2-D View of Generated Fan.....	28
Figure 4.6 : 3-D View of Generated Grid.....	28
Figure 4.7 : Prolate Spheroidal Coordinate's Projection (Moon 1988. p.31)....	29
Figure 4.8 : 2-D View of Generated Fan.....	29
Figure 4.9 : 3-D View of Generated Grid.....	30
Figure 4.10 : Form-Fitted Grid Around a Prolate Spheroidal Body.....	30
Figure 4.11 : Enlarged View of the Pole Region.....	31
Figure 4.12 : Cross-Sectional View of the Prolate Spheroidal Body.....	32
Figure 5.1 : Schematic 2-D View of Subsection 5.1.....	35
Figure 5.2 : Algorithm for the Heat Conduction Problems.....	36
Figure 5.3 : Grid View of Half Domain in Spherical Coordinates.....	37
Figure 5.4 : Different Aspect of Grid Domain in Spherical Coordinates.....	37
Figure 5.5 : Half View of the Results with Grid in Spherical Coordinates.....	38
Figure 5.6 : Another View of the Results without Grid in Spherical Coordinates.....	38
Figure 5.7 : Schematic 2-D View of Subsection 5.2.....	40
Figure 5.8 : Grid View of Half Domain in Prolate Spheroidal Coordinates.....	41
Figure 5.9 : Different Aspect of Grid Domain in Prolate Spheroidal Coordinate.....	41
Figure 5.10 : Half View of the Results with Grid in Prolate Spheroid Coordinates.....	42
Figure 5.11 : Another View of the Results without Grid in Prolate Spheroidal Coordinates.....	42
Figure 5.12 : Schematic 2-D View of Subsection 5.3.....	44
Figure 5.13 : Quarter Portion of a Half Sphere (Moon 1988. p.24).....	45
Figure 5.14 : Algorithm for Potential Flow Problems.....	47
Figure 5.15 : 2-D Presentation of Velocity Potentials.....	48
Figure 5.16 : 3-D Presentation of Velocity Potentials.....	48

Figure 5.17	: Transformation from Spherical Coordinates to Cartesian Coordinates.....	49
Figure 5.18	: Transformation for r-direction (Thomas 1998. p.844).....	50
Figure 5.19	: Velocity Distribution in the Domain.....	51
Figure 5.20	: Another View of Velocity Distribution.....	51
Figure 5.21	: Velocity Distribution Contours Around a Sphere.....	52
Figure 5.22	: Pressure Coefficient Around a Sphere.....	53
Figure 5.23	: Schematic 2-D View of Subsection 5.4.....	55
Figure 5.24	: 2-D Presentation of Velocity Potentials.....	56
Figure 5.25	: 3-D Presentation of Velocity Potentials.....	57
Figure 5.26	: Transformation from Prolate Spheroidal Coordinates to Cartesian Coordinates.....	58
Figure 5.27	: Transformation for η -direction.....	59
Figure 5.28	: Velocity Distribution in the Domain.....	60
Figure 5.29	: Another View of Velocity Distribution.....	61
Figure 5.30	: Velocity Distribution Contours Around a Prolate Spheroidal Body.....	62
Figure 5.31	: Pressure Coefficient Around Sphere.....	62
Figure 6.1	: Streamlines and Potential Lines for Inviscid Flow Past a Sphere (White 1995. p.538).....	64
Figure 6.2	: Vectorial Presentation of Velocity Results Around a Sphere.....	65
Figure 6.3	: Contoural Presentation of Velocity Results Around a Sphere.....	66
Figure 6.4	: Fluent Contoural Pressure Coefficient Distribution Results Around a Sphere.....	67
Figure 6.5	: Symlab Contoural Pressure Coefficient Distribution Results Around a Sphere.....	68
Figure 6.6	: Fluent Graphical Pressure Coefficient Distribution Results Around a Sphere.....	69
Figure 6.7	: Symlab Graphical Pressure Coefficient Distribution Results Around a Sphere.....	69
Figure 6.8	: In-House Code Pressure Coefficient Distribution Results Around A Sphere.....	69
Figure 6.9	: Theoric Graphical Pressure Coefficient Distribution Results Around A Sphere.....	69
Figure 6.10	: Vector Presentation of Velocity Results Around Prolate Spheroidal Body.....	70
Figure 6.11	: Contour Presentation of Velocity Results Around Prolate Spheroidal Body.....	71
Figure 6.12	: Fluent Contoural Pressure Coefficient Distribution Results Around Prolate Spheroidal Body.....	72
Figure 6.13	: Symlab Contoural Pressure Coefficient Distribution Results Around Prolate Spheroidal Body.....	72
Figure 6.14	: Fluent Graphical Pressure Coefficient Distribution Results Around Prolate Spheroidal Body	73
Figure 6.15	: Symlab and Theoric Graphical Pressure Coefficient Distribution Results Around Prolate Spheroidal Body.....	73
Figure 6.16	: In-House Code Pressure Coefficient Distribution Results Around Prolate Spheroidal Body.....	73

Figure 6.17	: In-House Code Sphere Cp Results with Different Grid Densities and Theoretical Graph.....	75
Figure 6.18	: In-House Code Prolate Spheroidal Body Cp Results with Different Grid Densities and Theoretical Graph.....	76
Figure B.1	: Node Number/Error Graph.....	82
Figure B.2	: Node Number/Computational Time Graph.....	83
Figure C	: Degree/Cp Results of Sphere	84

LIST OF SYMBOLS

r	: Radial Dimension in Spherical Coordinates
θ	: Angular Dimension in Spherical or Prolate Spheroidal Coordinates
Φ	: Angular Dimension in Spherical or Prolate Spheroidal Coordinates
η	: Radial Dimension in Prolate Spheroidal Coordinates
α	: Thermal Coefficient
V_x	: X direction Velocity Component in Cartesian Coordinates
V_y	: Y direction Velocity Component in Cartesian Coordinates
V_z	: Z direction Velocity Component in Cartesian Coordinates
V_r	: Radial Velocity Component in Spherical Coordinates
V_η	: Radial Velocity Component in Prolate Spheroidal Coordinates
V_θ	: Angular Velocity Component in Spherical or Prolate Spheroidal Coordinates
V_Φ	: Angular Velocity Component in Spherical or Prolate Spheroidal Coordinates
V_∞	: Velocity of Uniform flow
V_s	: Surface Velocity
Ψ	: Potential Function
∇^2	: Laplacian Operator
d	: Radius
T	: Temperature
t	: Time
π	: Pi-number
ω	: Relaxation Parameter
$\bar{\omega}$: Vorticity
$ V $: Resultant Velocity

KÜRESEL VE 3 BOYUTLU PROLAT KÜRESEL GÖVDE ÇEVRESİNDE ISI TRANSFERİ VE POTANSİYEL AKIŞ PROBLEMLERİNİN NUMERİK ANALİZİ

ÖZET

Bu tez, küre ve 3-boyutlu prolat küresel koordinat sisteminde oluşturulmuş gövde çevresinde ısı transferi ve potansiyel akış problemlerinin sayısal olarak analizini incelemektedir. Prolat koordinat sistemi; denizaltı, torpido ve sualtında faaliyet gösteren diğer araçların bir çoğunun gövde şekillerine benzerliği nedeniyle özellikle seçilmiştir. Prolat Küresel Koordinat sistemi, Küresel Koordinat sisteminde bir sabit ile ifade edilen r -yönündeki parametrenin -bir odak noktası uzaklığı (sabit bir uzaklık) ile sinus hiperbolik fonksiyonunun çarpımını içeren- bir değişken ile yer değiştirmesi sonucunda oluşturulmuş bir koordinat sistemidir. Programlama esnasında,

1. Çalışmaya daha fazla aşına olunması,
2. Yazılan kodun daha kısa olması,
3. Doğrulama işleminin daha az meşakkatli olması,

gibi nedenlerden dolayı algoritma ilk olarak Küresel Koordinatlarda oluşturulmuş ve bu nedenle tezin oluşumunda çeşitli küre örneklerine yer verilmiştir.

Birtakım sadeleştirme/kabul yapılması sonrasında ısı transferi ve potansiyel akış diferansiyel denklemlerinin birbirlerine benzerliğinden yararlanılmak istenmiş ve ilk olarak sınır şartları daha basit olan ısı transferi probleminin çözümü yapılmış ardından potansiyel akış problemine geçilmiştir.

Küre ve Prolat cisim çevresinde gerçekleşen ısı tranferi ve potansiyel akış olaylarının gözlenmesi için geliştirilmiş olan kodların sayısal çözümleri deneysel sonuçlar ve paket programlar ile karşılaştırılarak, tez çalışması için kullanılan sayısal çözüm algoritmalarının doğruluğu ve sağlamlığı gösterilmiştir.

Kompleks diferansiyel denklemlerin sayısal çözümlerini gerektiren günümüz problemlerinin çözümünde, ana mantığın oluşturulmasını ve bilgisayar teknolojisinden en verimli şekilde yararlanılmasını amaç edinmiş mevcut çalışmanın çözüm felsefesinin bundan sonra yapılacak benzer çalışmalara yol gösterici nitelikte bir deniz feneri olacağı tahmin edilmektedir.

NUMERICAL ANALYSIS OF HEAT CONDUCTION AND POTENTIAL FLOW PROBLEMS OVER A SPHERE AND A 3- DIMENSIONAL PROLATE SPHERICAL BODY

SUMMARY

This thesis presents numerical analysis of heat conduction and potential flow problems over a sphere and a 3-D prolate spheroidal body. Prolate Spheroidal Coordinate system is particularly selected because the shape of the submarines, torpedos and other underwater vehicles are very similar to the form of the body that constituted with mentioned coordinate system. Prolate Spheroidal Coordinate System is constituted with the substitution of a constant through r-direction in Spherical Coordinate System with a variable –the product of focus distance and sinus hyperbolic function-. Fundamental program algorithm first formed in Spherical Coordinates for,

1. More familiarity to Spheric Coordinate System,
2. Less complexity of code,
3. Less effort is needed for verification,

reasons. Therefore various type of sphere examples are given place in thesis content. After certain number of simplification/acceptance, utilization of resemblance between heat transfer and potential flow phenomenons is considered. First heat transfer problem analysis is executed because of less complexity in boundaries and then passed on to potential flow problem.

Robustness and accuracy of the algorithm is proved with the execution of comparison between the numerical results of in-house code which is generated to give output for the heat transfer and potential flow phonemenon around sphere and prolate body with teorical results and commercial codes.

It has been considered that present thesis solution methodology which is aspired to establish the basic logic and to utilize the computer technology in most efficient manner will be the lighthouse for the further similar investigations and nowadays problems that will require numerical solutions of sophisticated differential equations.

1. INTRODUCTION

Computational Fluid Dynamics, commonly known by the acronym CFD, started at the beginning of the 1970's. It became an acronym for a combination of physics, numerical mathematics, and to some extent of computer sciences which employed to stimulate fluid flows. Existence of more massive computer, commenced the CFD and progress in CFD is still coupled to the development in computer technology. Non-linear potential equation solutions, which interested in transonic flows, were the preliminary visualization of the CFD (**Blazek, 2001**).

First two dimensional (2-D) and then three dimensional (3-D) Euler equation solution become possible at the beginning of the 1980's. It was feasible to calculate inviscid flows over entire aeroplane or internal side of the turbomachines after the improvement of variety numerical acceleration techniques like multigrid and high speed supercomputers. Popularity area of the computations changed to the viscous flows conducted by the Navier-Stokes equations in the middle of 1980's. At the end of 1980's the solution of flow problems which is interested in real gas simulations also became possible by the improvement of numerical system, especially in the implicit scheme. The numerical simulation of the combustion and specially flame modelling is the still main investigation subjects of the most research activities. Necessity of more complicated grid output is the conclusion of the continually increasing desire in exactness and complexity of flow simulations (**Blazek, 2001**). Fluid flow problems shortly CFD was the interest area of academic, post doctoral, post graduate researcher or similarity expert who has enormously experience in the 1980's. Existence of many engineering computer softwares with robust solution algorithms and advanced pre- and post- processing features make easier the use of CFD programmes for design, research and development purposes by graduate engineers (**Versteeg and Malalasekera, 1995**).

The grow up process was initiated with fairly formed meshes either formed by algebraic methods or by using partial differential equations. The grids had to be

splitted up into more plainer portions because of the more complicated assemblies. Giving permission to assign lightened constraints to the grid constitution for a lone block which has inappropriate faces between the others in the grid assembly was the subsequent sensible step. Solution techniques that can interest in overlapped grid blocks were met at the end (**Blazek, 2001**).

Nowadays aircraft, turbomachinery, car and ship design are the common areas of CFD techniques. Nevertheless, meteorology, oceanography, astrophysics, architecture and oil recovery are the other interests (**Blazek, 2001**). Moreover, **Anderson (1995)** state that “Computational fluid dynamics is a major tool in solving hydrodynamic problems associated with ships, submarines, torpedos etc.”

Thus far, the history and development of the CFD is investigated and compiled. As known, partial differential equations, which cannot be solved analytically except special cases, are the fundamental way to express the flows and related phenomena. However, for the entire complex and complicated problems (geometries) there is not any possibility to obtain exact analytic solution. Discretization method, which proximates the differential equations by systems of algebraic equations, have to be used to obtain approximate solution. Numerical solution provides results at discrete regions in time and space due to the approximations that are applied to small domains in time or space. Accuracy of the numerical solutions are strictly based upon the quality of the discretizations that used for domain.

Another crucial point of the CFD analysis lay on the mesh algorithms. **Thomson et. al (1985)** were focused on forming different types of mesh algorithms. In their studies many detailed mesh algorithms were investigated and experimented over 2-D and 3-D surfaces or volumetric bodies. **Knupp (1993)** executed different applications on these methodologies. These exercises guided and illuminated many researchers/investigators who is interested in CFD simulations and analysis.

Many distinct sources mention the concept of finite difference approximations to partial derivatives eg. in **Lomax et. al. (1999)** or **Hoffman (1989)**. Either spatial derivatives or time derivatives can be performed to these approximations. Various types of meshes expressed in general curvilinear coordinates in physical space might be transformed to a uniform Cartesian mesh with equally spaced intervals and it is called computational space.

An object of this thesis is to examine and investigate numerically the heat conduction and potential flow over both a sphere and a 3-D prolate body. Additionally, the comparison of results between in-house code and theoretical results and the commercial codes which were both applied for sphere and a 3-D prolate body have been executed to prove the results. Prolate spheroidal coordinate system is particularly selected because the shape of the submarines, torpedos and other underwater vehicles are very similar to the form of the body that constituted with mentioned coordinate system.

Flow past prolate spheroids has been studied by many others both experimentally and numerically. On experimental side, **Meier et al. (1984,1986)**, **Chesnakas and Simpson (1997)**, **Wetzel et. al. (1998)** and **Goody et. al. (2000)** provided invaluable data-sets to validate CFD codes for flow around a prolate spheroids. On numerical side, **Vatsa et. al. (1989)**, **Deng et. al. (1990)**, **Kim and Patel (1991)**, **Gee et. al. (1992)**, **Zheng et. al. (1997)**, **Rhee and Hino (2000)** and **Rhee et. al. (2003)** studies are interested in flow around a prolate spheroids that they used full Navier-Stokes or Reynolds-averaged Navier Stokes (RANS) equations. Many of these articles can be found at United States Department of Defence Internet archives.

First part of this dissertation is the introduction part. In the second section, mathematical modelling in the spherical coordinate system is investigated. Solution methodology with the principles of solution of the governing equations, including the discretization and arrangement with different iterative methods, are briefly introduced. Examples and applications of the iterative methods are elaborated. They initiated from cartesian coordinates to spherical coordinates in order to establish the fundamentals on reliable basis. Mathematical modelling and the description of the iteration coefficients in the Prolate Spheroidal Coordinate System is formed in the third section. Section two and section three can be used together to get acquainted with the solution algorithm rudiments.

As mentioned before, grid is one of the most important parameter for the analysis. Hence the fourth section is allocated to the grid generation. In this section grid generation is shortly described. Then formed meshes around sphere and prolate spheroidal body are depicted.

Fifth section content is comprise of explanation of heat conduction, potential flow domains, application of boundary conditions to these domains and presentation of numerical results (velocity potentials, velocity vectors, pressure coefficient distribution) around concerned bodies. Moreover vectorial transformation from spherical coordinates to cartesian coordinates and prolate coordinates to cartesian coordinates are given place in this section.

Potential flow over a sphere is the well-known and popular example for the external flow problems and it's effortless to find solution of potential velocity, velocity vectors and pressure distributions results even in the fundamental fluid mechanics books (**White 1995, Panton 1984, Owczarek 1968, etc.**) but it is hard to express the same for a prolate shape. Considerably similar problem was solved analitically by **Sabuncu (1962)**, however different bodies are taken into account. Therefore only pictural comparison for a sphere domain is made with literature sources. Notwithstanding comparison of results between in house-code and two commercial codes -Fluent and SymLab-are given in section six. Last section is assigned to conclusion part.

2. MATHEMATICAL MODELING AND NUMERICAL METHODS IN SPHERICAL COORDINATES

A special class of inviscid flows occurs when the vorticity is zero. A fluid flow that is both inviscid and irrotational is called an ideal flow or equivalently a potential flow. The velocity field of an ideal flow is completely determined by two kinematic considerations: the rate of particle expansion and the rate of particle rotation are both zero (**Panton, 1984**). Mathematically these conditions can be shown as;

$$\nabla \cdot \mathbf{v} = 0 \quad (2.1)$$

$$\nabla \times \mathbf{v} = \vec{\omega} = 0 \quad (2.2)$$

The solution of equations (2.1), (2.2) is most easily found by using the velocity potential defined by;

$$\mathbf{v} = \nabla \psi \quad (2.3)$$

The equation for ψ is found by substituting (2.3) into (2.1). The result is the Laplace equation.

$$\nabla^2 \psi = 0 \quad (2.4)$$

where

$$\psi = \psi(r, \theta, \phi) \quad (2.5)$$

r, θ, ϕ designate the ordinates and the dimensions are,

$$0 \leq r \leq \infty \quad (2.6a)$$

$$0 \leq \theta \leq \pi \quad (2.6b)$$

$$0 \leq \phi \leq 2\pi \quad (2.6c)$$

Spherical Coordinate system and its derivatives (Prolate Spheroidal and Oblate Spheroidal) ordinates follow the same trajectories. θ sweeps from 0 to π and ϕ sweeps from 0 to 2π radians. Special attention should be paid to border of the angles during forming grid and iteration phases.

Conversion from spherical polar coordinates to the Cartesian coordinates can be made substituting the following equations into the fundamental equations;

$$x = r\sin(\theta)\cos(\phi) \quad (2.7)$$

$$y = r\sin(\theta)\sin(\phi) \quad (2.8)$$

$$z = r\cos(\theta) \quad (2.9)$$

The explicit formulation of finite difference equation in cartesian coordinate system for Laplace Equation is;

$$\nabla^2\psi = \frac{\partial^2\psi}{\partial x^2} + \frac{\partial^2\psi}{\partial y^2} = 0 \quad (2.10)$$

If first order central difference approximation is used, equation (2.10) can be expressed as,

$$\frac{\psi_{i+1,j} - 2\psi_{i,j} + \psi_{i-1,j}}{(\Delta x)^2} + \frac{\psi_{i,j+1} - 2\psi_{i,j} + \psi_{i,j-1}}{(\Delta y)^2} = 0 \quad (2.11)$$

The Laplace equation can be expressed in the spherical polar coordinates that takes the form;

$$\nabla^2\psi = \frac{\partial^2\psi}{\partial r^2} + \frac{2}{r} \frac{\partial\psi}{\partial r} + \frac{1}{r^2} \frac{\partial^2\psi}{\partial \theta^2} + \frac{\cot(\theta)}{r^2} \frac{\partial\psi}{\partial \theta} + \frac{1}{r^2 \sin^2\theta} \frac{\partial^2\psi}{\partial \phi^2} = 0 \quad (2.12)$$

Trigonometric term in equation (2.12) denominator causes a problem in the numerical calculations and therefore it should be eliminated from the equation. Because it leads to singularity when $\theta = 0$ in the discretized form. Hence multiplying both sides of equation (2.12) by $r^2 \sin^2(\theta)$;

$$r^2 \sin^2\theta \frac{\partial^2\psi}{\partial r^2} + 2r \sin^2\theta \frac{\partial\psi}{\partial r} + \sin^2\theta \frac{\partial^2\psi}{\partial \theta^2} + \sin\theta \cos\theta \frac{\partial\psi}{\partial \theta} + \frac{\partial^2\psi}{\partial \phi^2} = 0 \quad (2.13)$$

If first order central difference approximation is used, the following equation will be obtained;

$$\begin{aligned}
& r_{i,j,k}^2 \text{Sin}^2 \theta_{i,j,k} \left[\frac{\Psi_{i+1,j,k} - 2\Psi_{i,j,k} + \Psi_{i-1,j,k}}{\Delta r_{i,j,k}^2} \right] + 2r_{i,j,k} \text{Sin}^2 \theta_{i,j,k} \left[\frac{\Psi_{i+1,j,k} - \Psi_{i-1,j,k}}{2\Delta r_{i,j,k}} \right] \\
& + \text{Sin}^2 \theta_{i,j,k} \left[\frac{\Psi_{i,j+1,k} - 2\Psi_{i,j,k} + \Psi_{i,j-1,k}}{\Delta \theta_{i,j,k}^2} \right] + \text{Sin} \theta_{i,j,k} \text{Cos} \theta_{i,j,k} \left[\frac{\Psi_{i,j+1,k} - \Psi_{i,j-1,k}}{2\Delta \theta_{i,j,k}} \right] \\
& + \left[\frac{\Psi_{i,j,k+1} - 2\Psi_{i,j,k} + \Psi_{i,j,k-1}}{\Delta \phi^2} \right] = 0 \tag{2.14}
\end{aligned}$$

The solution to equation (2.14) can be obtained by both direct methods or iterative methods. Cramer's rule and Gaussian Elimination are some of the acquaintance direct methods. Almost all of direct methods have problems such as the rectangular domain, a large storage requirement, the size of the coefficient matrix, boundary conditions, difficulty of programming or cartesian coordinate system. On the other hand iterative methods are more plain and easy to program. Iterative methods can be splitted into two types. Potential iterative methods when equation results in one unknown and Line iterative methods when equation results in more than one unknowns. Generally, iteration starts with guessed solution and new values based on former calculated step for the solution domain. Iteration loop produces new values until a designated convergence criteria has been attained (**Hoffmann 1989**).

2.1 The Jakobi Iteration Method

The main idea behind this method is; to use a beginning guess solution and sought to correct solution by solving the equations in an order. Correction process initiates at point $i=j=1$ and advances either line by line or column by column throughout the formed mesh in the domain (**Hirsch 1989**).

If prosedure is applied to the laplace equation in cartesian coordinates which can be seen equation (2.11). Take $\Delta x = \Delta y = 1$ and by rearranging

$$\Psi_{i+1,j} + \Psi_{i-1,j} + \Psi_{i,j+1} + \Psi_{i,j-1} - 4\Psi_{i,j} = 0 \tag{2.15}$$

$$\Psi_{i,j}^{\text{new}} = \frac{1}{4} \left[\Psi_{i-1,j} + \Psi_{i+1,j} + \Psi_{i,j-1} + \Psi_{i,j+1} \right]^{\text{old}} \quad (2.16)$$

After an initial guess of the solution is applied, the procedure initiate to obtain the solution for the domain. $\Psi_{i,j}^0$ denotes initial guess, $\Psi_{i,j}^1$ denotes first iteration (which was determined from $\Psi_{i,j}^0$. $\Psi_{i,j}^2$ denotes the second iteration which was determined from $\Psi_{i,j}^1$ and process goes on. So, general designation of the Laplace equation for (m+1)st iteration can be shown as (**Haberman 1983**);

$$\Psi_{i,j}^{m+1} = \frac{1}{4} \left[\Psi_{i-1,j}^m + \Psi_{i+1,j}^m + \Psi_{i,j-1}^m + \Psi_{i,j+1}^m \right] \quad (2.17)$$

Application can be formed for the spherical coordinate system. Revert back to equation. (2.14) and express the coefficient with using notation which is shown in Figure (2.1.1). (Upper and Lower denotes the former and subsequent steps in third dimension)

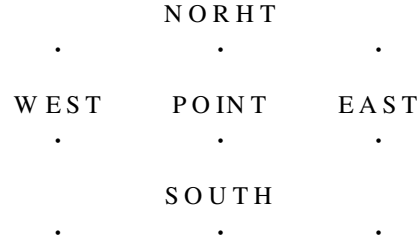


Figure 2.1: 2-D view of the coefficient notation.

$$\Psi_{i,j,k} \rightarrow \frac{-2r^2 \text{Sin}^2(\theta)}{\Delta r^2} + \frac{-2 \text{Sin}^2(\theta)}{\Delta \theta^2} + \frac{-2}{\Delta \phi^2} \rightarrow \text{JP (coefficient at Point)} \quad (2.18a)$$

$$\Psi_{i-1,j,k} \rightarrow \frac{r^2 \text{Sin}^2(\theta)}{\Delta r^2} - \frac{r \text{Sin}^2(\theta)}{\Delta r} \rightarrow \text{JW (coefficient at West)} \quad (2.18b)$$

$$\Psi_{i+1,j,k} \rightarrow \frac{r^2 \text{Sin}^2(\theta)}{\Delta r^2} + \frac{r \text{Sin}^2(\theta)}{\Delta r} \rightarrow \text{JE (coefficient at East)} \quad (2.18c)$$

$$\Psi_{i,j-1,k} \rightarrow \frac{\text{Sin}^2(\theta)}{\Delta \theta^2} - \frac{\text{Sin}(\theta) \text{Cos}(\theta)}{2 \Delta \theta} \rightarrow \text{JS (coefficient at South)} \quad (2.18d)$$

$$\Psi_{i,j+1,k} \rightarrow \frac{\text{Sin}^2(\theta)}{\Delta \theta^2} + \frac{\text{Sin}(\theta) \text{Cos}(\theta)}{2 \Delta \theta} \rightarrow \text{JN (coefficient at North)} \quad (2.18e)$$

$$\Psi_{i,j,k-1} \rightarrow \frac{1}{\Delta\phi^2} \rightarrow \text{JL (coefficient at Lower layer)} \quad (2.18f)$$

$$\Psi_{i,j,k+1} \rightarrow \frac{1}{\Delta\phi^2} \rightarrow \text{JU (coefficient at Upper layer)} \quad (2.18g)$$

Substituting the coefficient into the governing Laplace equation which was denoted in discrete form in equation (2.14) takes the form;

$$\begin{aligned} \text{JP} \bullet \Psi_{i,j,k} + \text{JW} \bullet \Psi_{i-1,j,k} + \text{JE} \bullet \Psi_{i+1,j,k} + \text{JS} \bullet \Psi_{i,j-1,k} \\ + \text{JN} \bullet \Psi_{i,j+1,k} + \text{JL} \bullet \Psi_{i,j,k-1} + \text{JU} \bullet \Psi_{i,j,k+1} = 0 \end{aligned} \quad (2.19)$$

If terms are rearranged in equation (2.19) takes form like;

$$\begin{aligned} \Psi_{i,j,k}^{m+1} = \frac{-1}{\text{JP}} \left[\text{JW} \bullet \Psi_{i-1,j,k}^m + \text{JE} \bullet \Psi_{i+1,j,k}^m + \text{JS} \bullet \Psi_{i,j-1,k}^m \right. \\ \left. + \text{JN} \bullet \Psi_{i,j+1,k}^m + \text{JL} \bullet \Psi_{i,j,k-1}^m + \text{JU} \bullet \Psi_{i,j,k+1}^m \right] = 0 \end{aligned} \quad (2.20)$$

2.2 Gauss Seidel Iteration Method

There is a methodology which needs less calculation to reach the approximate solution for the discretized Laplace's equation. Every Jacobi iteration needs new values, which calculated in the previous iteration, for each mesh point respectively in the domain. However, Gauss-Seidel iteration method uses the new values while advancing on the same iteration plane.

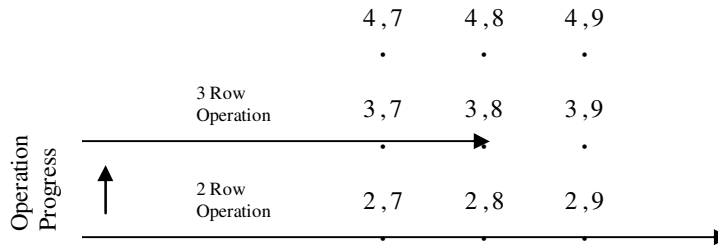


Figure 2.2: Gauss-Seidel Iteration Schema

For example, in Jacobi iteration $\Psi_{2,8}^m$, $\Psi_{3,7}^m$, $\Psi_{3,9}^m$, $\Psi_{4,8}^m$ has to be used in order to complete iteration even new values have already been obtained for points $\Psi_{2,8}^m$ and

$\psi_{3,7}^m$. If old values are demolished after a new one is calculated, computation shall be more easy (**Haberman 1983**). Difference between Gauss-Seidel and the Jakobi iteration methods is; usage of the new values in the calculation while progressing in the same iteration step. It can be shown for the cartesian coordinates like,

$$\psi_{i,j}^{m+1} = \frac{1}{4} \left[\psi_{i-1,j}^{m+1} + \psi_{i+1,j}^m + \psi_{i,j-1}^{m+1} + \psi_{i,j+1}^m \right] \quad (2.21)$$

Same notation and coefficient, which was used in section 2.1 (equation (2.18a) to equation (2.18g)), can be applied for the Laplace Equation which is opened in spherical coordinate system.

$$\begin{aligned} \psi_{i,j,k}^{m+1} = \frac{-1}{GSP} \left[GSW \bullet \psi_{i-1,j,k}^{m+1} + GSE \bullet \psi_{i+1,j,k}^m + GSS \bullet \psi_{i,j-1,k}^{m+1} \right. \\ \left. + GSN \bullet \psi_{i,j+1,k}^m + GSL \bullet \psi_{i,j,k-1}^{m+1} + GSU \bullet \psi_{i,j,k+1}^m \right] = 0 \end{aligned} \quad (2.22)$$

2.3 Successive Over Relaxation

Solution by iteration can be thought of as a process beginning at an initial state and approaching a steady state. During the solution process if tendency in the calculated values of the dependent variable is noted then, the direction of change can be used to extrapolate for the next iteration and thus, reduce the solution time. This procedure is known as Successive Over-Relaxation (**Hoffmann 1989**).

First, apply it to the cartesian coordinate and add $+\psi_{i,j}^m, -\psi_{i,j}^m$ to the right hand side of the equation (2.21)

$$\psi_{i,j}^{m+1} = \psi_{i,j}^m + \frac{1}{4} \left[\psi_{i-1,j}^{m+1} + \psi_{i+1,j}^m + \psi_{i,j-1}^{m+1} + \psi_{i,j+1}^m - 4\psi_{i,j}^m \right] \quad (2.23)$$

$\psi_{i,j}^m$ must approach $\psi_{i,j}^{m+1}$, as the solution proceed. To accelerate the solution the term in bracket is multiplied by ω ,

$$\psi_{i,j}^{m+1} = \psi_{i,j}^m + \omega \left[\psi_{i-1,j}^{m+1} + \psi_{i+1,j}^m + \psi_{i,j-1}^{m+1} + \psi_{i,j+1}^m - 4\psi_{i,j}^m \right] \quad (2.24)$$

If it is applied to the discretized Laplace's equation which is in spherical coordinates (above mentioned notation is taken into consideration), it will take form;

$$\begin{aligned} \Psi_{i,j,k}^{m+1} = \Psi_{i,j,k}^m + \omega \left[\text{GSW} \cdot \Psi_{i-1,j,k}^{m+1} + \text{GSE} \cdot \Psi_{i+1,j,k}^m + \text{GSS} \cdot \Psi_{i,j-1,k}^{m+1} \right. \\ \left. + \text{GSN} \cdot \Psi_{i,j+1,k}^m + \text{GSL} \cdot \Psi_{i,j,k-1}^{m+1} + \text{GSU} \cdot \Psi_{i,j,k+1}^m + \text{GSP} \cdot \Psi_{i,j,k}^m \right] = 0 \end{aligned} \quad (2.25)$$

Generally, it is hard to determine optimum ω . There is not any usual technique to obtain the relaxation parameter, it's value depends on the fundamental equation and the domain of the problem. Hence, in most cases numerical experimentation is the only way to determine the relaxation parameter (**Hoffmann 1989**).

2.4 The Alternating Direction Implicit (ADI) Method

Alternating Direction Implicit (ADI) Method is slightly different from above mentioned methods. Single cycle in Alternating Direction Method consist of three distinct sweeps in the three ordinates (r, θ, ϕ) of the coordinate system. A sweep is arranged in each time interval, all points that are not located in the direction of the sweep are assumed to be known values from the previous iteration cycle. These values are hence gathered on the right side of the equation at each cycle. An iteration cycle is considered complete once the resulting tridiagonal system is solved for entire domain. (**Anderson 1995**).

First, apply the method for cartesian coordinate system which considered as 2-D, afterward obtain the equations in spherical coordinates.

First Step: x-Sweep

$$\frac{\Psi_{i+1,j}^{n+1/2} - 2\Psi_{i,j}^{n+1/2} + \Psi_{i-1,j}^{n+1/2}}{(\Delta x)^2} + \frac{\Psi_{i,j+1}^n - 2\Psi_{i,j}^n + \Psi_{i,j-1}^n}{(\Delta y)^2} = 0 \quad (2.26)$$

$$\left(\frac{\Delta y}{\Delta x}\right)^2 \Psi_{i+1,j}^{n+1/2} - 2\left(\frac{\Delta y}{\Delta x}\right)^2 \Psi_{i,j}^{n+1/2} + \left(\frac{\Delta y}{\Delta x}\right)^2 \Psi_{i-1,j}^{n+1/2} = -\left[\Psi_{i,j+1}^n - 2\Psi_{i,j}^n + \Psi_{i,j-1}^n\right] \quad (2.27)$$

Anderson stated that; although, Laplace's equation can be solved by equation (2.26), however much computational time is needed than tridiagonalized system. Equation (2.26) can be reduced to tridiagonal form like;

$$A \cdot \psi_{i+1,j}^{n+1/2} - B \cdot \psi_{i,j}^{n+1/2} + A \cdot \psi_{i-1,j}^{n+1/2} = K_i \quad (2.28)$$

where

$$A = \left(\frac{\Delta y}{\Delta x} \right)^2 \quad (2.29a)$$

$$B = 2 \left(\frac{\Delta y}{\Delta x} \right)^2 \quad (2.29b)$$

$$K_i = -[\psi_{i,j+1}^n - 2\psi_{i,j}^n + \psi_{i,j-1}^n] \quad (2.29c)$$

Equation (2.28) yields a solution for $\psi_{i,j}^{n+1/2}$ for all i , with keeping j fixed. X-direction sweep continues until the last grid point in the domain line. This calculation philosophy is shown schematically in Figure (2.4.1).

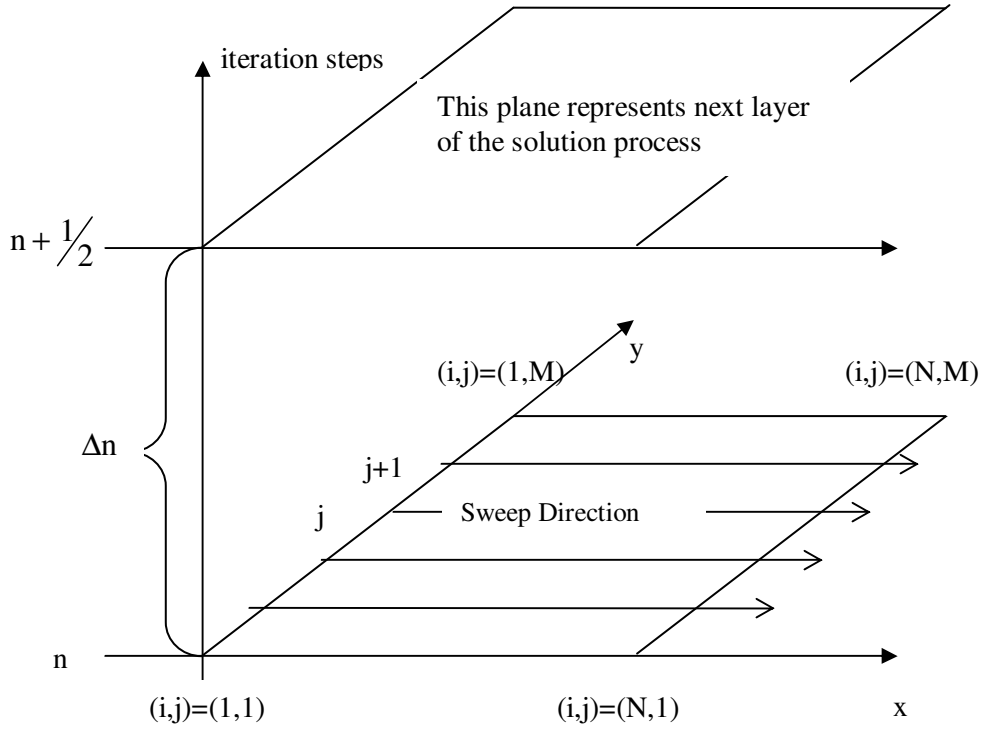


Figure 2.3: Schematical view of ADI x direction sweep

The second step of ADI method is solving equation (2.26) for the y-direction which is being represented with step $n+1$. Second step uses the step $\psi_{i,j}^{n+1/2}$ values.

Second Step: y-Sweep

$$\frac{\Psi_{i+1,j}^{n+1/2} - 2\Psi_{i,j}^{n+1/2} + \Psi_{i-1,j}^{n+1/2}}{(\Delta x)^2} + \frac{\Psi_{i,j+1}^{n+1} - 2\Psi_{i,j}^{n+1} + \Psi_{i,j-1}^{n+1}}{(\Delta y)^2} = 0 \quad (2.30)$$

$$\left(\frac{\Delta x}{\Delta y}\right)^2 \Psi_{i,j+1}^{n+1} - 2\left(\frac{\Delta x}{\Delta y}\right)^2 \Psi_{i,j}^{n+1} + \left(\frac{\Delta x}{\Delta y}\right)^2 \Psi_{i,j-1}^{n+1} = -\left[\Psi_{i+1,j}^{n+1/2} - 2\Psi_{i,j}^{n+1/2} + \Psi_{i-1,j}^{n+1/2}\right] \quad (2.31)$$

Equation (2.26) reduces to tridiagonal form;

$$C \cdot \Psi_{i,j-1}^{n+1} - D \cdot \Psi_{i,j}^{n+1} + C \cdot \Psi_{i,j+1}^{n+1} = L_i \quad (2.32)$$

where

$$C = \left(\frac{\Delta x}{\Delta y}\right)^2 \quad (2.33a)$$

$$D = 2\left(\frac{\Delta x}{\Delta y}\right)^2 \quad (2.33b)$$

$$L_i = -\left[\Psi_{i+1,j}^{n+1/2} - 2\Psi_{i,j}^{n+1/2} + \Psi_{i-1,j}^{n+1/2}\right] \quad (2.33c)$$

Equation (2.32) yields a solution for $\Psi_{i,j}^{n+1}$ for all j , with keeping i fixed. Y-direction sweep continues until the last grid point in the domain line. This calculation is shown schematically in Figure (2.4.2).

Application can be formed for the spherical coordinate system. Revert to Equation (2.14) and rewrite the same procedure with using a slightly different notation for the coefficients which belongs to Alternating Direction Implicit procedure.

$$\Psi_{i,j,k} \rightarrow \frac{-2r^2 \sin^2(\theta)}{\Delta r^2} + \frac{-2 \sin^2(\theta)}{\Delta \theta^2} + \frac{-2}{\Delta \phi^2} \rightarrow \text{ADIP (coefficient at Point)} \quad (2.34a)$$

$$\Psi_{i-1,j,k} \rightarrow \frac{r^2 \sin^2(\theta)}{\Delta r^2} - \frac{r \sin^2(\theta)}{\Delta r} + \rightarrow \text{ADIW (coefficient at West)} \quad (2.34b)$$

$$\Psi_{i+1,j,k} \rightarrow \frac{r^2 \sin^2(\theta)}{\Delta r^2} + \frac{r \sin^2(\theta)}{\Delta r} + \rightarrow \text{ADIE (coefficient t East)} \quad (2.34c)$$

$$\Psi_{i,j-1,k} \rightarrow \frac{\sin^2(\theta)}{\Delta \theta^2} - \frac{\sin(\theta) \cos(\theta)}{2\Delta \theta} + \rightarrow \text{ADIS (coefficient at South)} \quad (2.34d)$$

$$\Psi_{i,j+1,k} \rightarrow \frac{\sin^2(\theta)}{\Delta\theta^2} + \frac{\sin(\theta)\cos(\theta)}{2\Delta\theta} + \rightarrow \text{ADIN (coefficient at North)} \quad (2.34e)$$

$$\Psi_{i,j,k-1} \rightarrow \frac{1}{\Delta\phi^2} \rightarrow \text{ADIL (coefficient at Lower layer)} \quad (2.34f)$$

$$\Psi_{i,j,k+1} \rightarrow \frac{1}{\Delta\phi^2} \rightarrow \text{ADIU (coefficient at Upper layer)} \quad (2.34g)$$

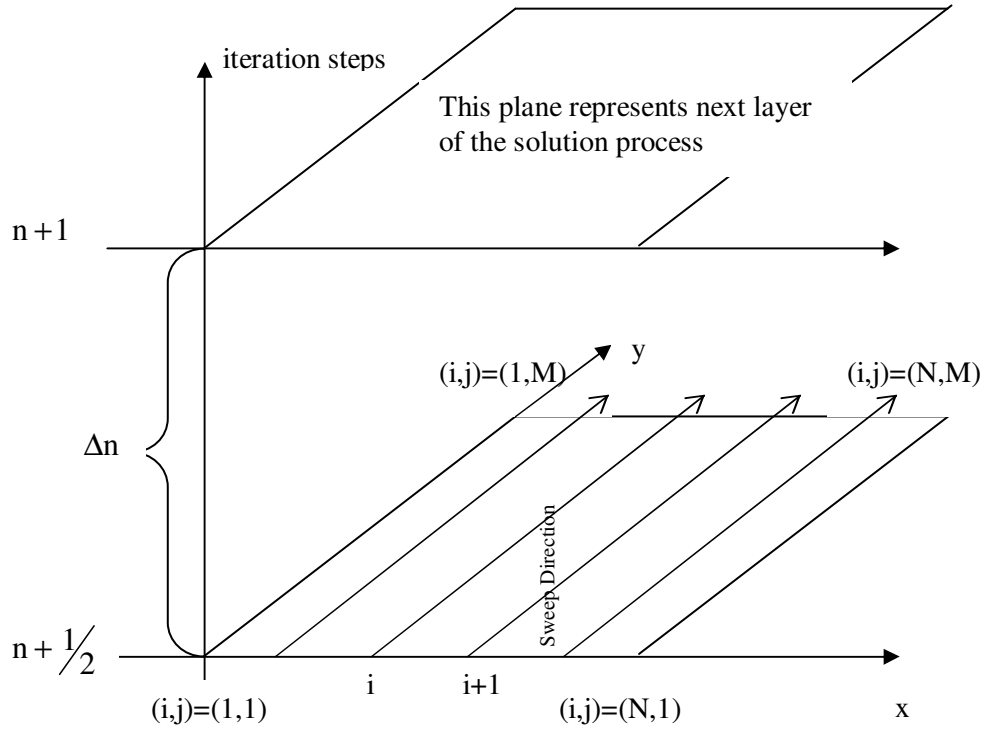


Figure 2.4: Schematical view of ADI y direction sweep

If it is applied to the discretized Laplace's equation which is in spherical coordinates, it will take form as;

First step: r-Sweep

$$\begin{aligned} & \text{ADIW} \cdot \Psi_{i-1,j,k}^{n+\frac{1}{3}} + \text{ADIP} \cdot \Psi_{i,j,k}^{n+\frac{1}{3}} + \text{ADIE} \cdot \Psi_{i+1,j,k}^{n+\frac{1}{3}} = \\ & - \left(\text{ADIN} \cdot \Psi_{i,j+1,k}^n + \text{ADIS} \cdot \Psi_{i,j-1,k}^n + \text{ADIU} \cdot \Psi_{i,j,k+1}^n + \text{ADIL} \cdot \Psi_{i,j,k-1}^n \right) \end{aligned} \quad (2.35)$$

Note: The superscript $n + \frac{1}{3}$ designates the first ordinate's sweep.

Anderson (1995) stated that; although, Laplace's equation can be solved by equation (2.35), however much computational time is needed than tridiagonalized system.

Equation (2.35) can be reduced to tridiagonal form like;

$$A_i \cdot \psi_{i-1,j,k}^{n+1/3} - B_i \cdot \psi_{i,j,k}^{n+1/3} + C_i \cdot \psi_{i+1,j,k}^{n+1/3} = K_i \quad (2.36)$$

where

$$A_i = \text{ADIW} \quad (2.37a)$$

$$B_i = \text{ADIP} \quad (2.37b)$$

$$C_i = \text{ADIE} \quad (2.37c)$$

$$K_i = -\left(\text{ADIN} \cdot \psi_{i,j+1,k}^n + \text{ADIS} \cdot \psi_{i,j-1,k}^n + \text{ADIU} \cdot \psi_{i,j,k+1}^n + \text{ADIL} \cdot \psi_{i,j,k-1}^n \right) \quad (2.37d)$$

Second Step: θ -Sweep

$$\begin{aligned} & \text{ADIN} \cdot \psi_{i,j+1,k}^{n+2/3} + \text{ADIP} \cdot \psi_{i,j,k}^{n+2/3} + \text{ADIS} \cdot \psi_{i,j-1,k}^{n+2/3} = \\ & -\left(\text{ADIW} \cdot \psi_{i-1,j,k}^{n+1/3} + \text{ADIE} \cdot \psi_{i+1,j,k}^{n+1/3} + \text{ADIU} \cdot \psi_{i,j,k+1}^n + \text{ADIL} \cdot \psi_{i,j,k-1}^n \right) \end{aligned} \quad (2.38)$$

Note: The superscript $n + \frac{2}{3}$ designates the second ordinate's sweep.

Equation (2.38) can be reduced to tridiagonal form like;

$$D_j \cdot \psi_{i,j+1,k}^{n+2/3} - E_j \cdot \psi_{i,j,k}^{n+2/3} + F_j \cdot \psi_{i,j-1,k}^{n+2/3} = L_j \quad (2.39)$$

where

$$D_j = \text{ADIN} \quad (2.40a)$$

$$E_j = \text{ADIP} \quad (2.40b)$$

$$F_j = \text{ADIS} \quad (2.40c)$$

$$L_j = -\left(\text{ADIW} \cdot \psi_{i-1,j,k}^{n+1/3} + \text{ADIE} \cdot \psi_{i+1,j,k}^{n+1/3} + \text{ADIU} \cdot \psi_{i,j,k+1}^n + \text{ADIL} \cdot \psi_{i,j,k-1}^n \right) \quad (2.40d)$$

Third Step: ϕ -Sweep

$$\begin{aligned} & \text{ADIU} \cdot \psi_{i,j,k+1}^{n+1} + \text{ADIP} \cdot \psi_{i,j,k}^{n+1} + \text{ADIL} \cdot \psi_{i,j,k-1}^{n+1} = \\ & -\left(\text{ADIW} \cdot \psi_{i-1,j,k}^{n+1/3} + \text{ADIE} \cdot \psi_{i+1,j,k}^{n+1/3} + \text{ADIN} \cdot \psi_{i,j+1,k}^{n+2/3} + \text{ADIS} \cdot \psi_{i,j-1,k}^{n+2/3} \right) \end{aligned} \quad (2.41)$$

Note: The superscript $n+1$ designates the third ordinate's sweep.

Equation (2.41) can be reduced to tridiagonal form like;

$$G_k \cdot \Psi_{i,j,k+1}^{n+1} - H_k \cdot \Psi_{i,j,k}^{n+1} + I_k \cdot \Psi_{i,j,k-1}^{n+1} = P_k \quad (2.42)$$

where

$$G_k = \text{ADIU} \quad (2.43a)$$

$$H_k = \text{ADIP} \quad (2.43b)$$

$$I_k = \text{ADIL} \quad (2.43c)$$

$$P_k = -\left(\text{ADIW} \cdot \Psi_{i-1,j,k}^{n+1/3} + \text{ADIE} \cdot \Psi_{i+1,j,k}^{n+1/3} + \text{ADIS} \cdot \Psi_{i,j-1,k}^{n+2/3} + \text{ADIN} \cdot \Psi_{i,j+1,k}^{n+2/3} \right) \quad (2.43d)$$

In this methodology, equation. (2.36) is solved implicitly for the unknown in the r direction, equation (2.39) is solved implicitly for the unknown in the θ direction and equation (2.42) is solved implicitly for the unknown in the ϕ direction.

As mentioned in the previous paragraphs, obtained equation has to form a tridiagonal matrix whose first element on the first row and the last element in the last row are known values from the boundary conditions to achieve the solution easily. Thusfar, the fundamental equations for the solution have introduced, in this order next step is constitute tridiagonal matrix for the algorithm.

Examine the construction process for the diabolization of the Laplace equation in 2-Dimensional cartesian coordinate system with simple example. Revert to equation (2.28) and apply the formulation only for x-sweep in scope of Figure 2.43.

$$i=2, j=2 \quad \rightarrow \quad A \cdot \Psi_{1,2}^{n+1/2} - B \cdot \Psi_{2,2}^{n+1/2} + A \cdot \Psi_{3,2}^{n+1/2} = K_2 \quad (2.44a)$$

$$i=3, j=2 \quad \rightarrow \quad A \cdot \Psi_{2,2}^{n+1/2} - B \cdot \Psi_{3,2}^{n+1/2} + A \cdot \Psi_{4,2}^{n+1/2} = K_3 \quad (2.44b)$$

$$i=4, j=2 \quad \rightarrow \quad A \cdot \Psi_{3,2}^{n+1/2} - B \cdot \Psi_{4,2}^{n+1/2} + A \cdot \Psi_{5,2}^{n+1/2} = K_4 \quad (2.44c)$$

$$i=5, j=2 \quad \rightarrow \quad A \cdot \Psi_{4,2}^{n+1/2} - B \cdot \Psi_{5,2}^{n+1/2} + A \cdot \Psi_{6,2}^{n+1/2} = K_5 \quad (2.44d)$$

$$i=6, j=2 \quad \rightarrow \quad A \cdot \Psi_{5,2}^{n+1/2} - B \cdot \Psi_{6,2}^{n+1/2} + A \cdot \Psi_{7,2}^{n+1/2} = K_6 \quad (2.44e)$$

Revert to equations (2.44a) and (2.44e). If the value for boundaries are known (consider boundaries have dirichlet boundary constraint) formulation for beginning and end points will take the form;

$$i=2, j=2 \quad \rightarrow \quad -B \cdot \Psi_{2,2}^{n+1/2} + A \cdot \Psi_{3,2}^{n+1/2} = K_2 - A \cdot \Psi_{1,2}^{n+1/2} \quad (2.45a)$$

$$-B \cdot \psi_{2,2}^{n+1/2} + A \cdot \psi_{3,2}^{n+1/2} = K'_2 \quad (2.45b)$$

where

$$K'_2 = K_2 - A \cdot \psi_{1,2}^{n+1/2} \quad (2.45c)$$

$$i=6, j=2 \quad \rightarrow \quad A \cdot \psi_{5,2}^{n+1/2} - B \cdot \psi_{6,2}^{n+1/2} = K_6 - A \cdot \psi_{7,2}^{n+1/2} \quad (2.46a)$$

$$A \cdot \psi_{5,2}^{n+1/2} - B \cdot \psi_{6,2}^{n+1/2} = K'_6 \quad (2.46b)$$

where

$$K'_6 = K_6 - A \cdot \psi_{7,2}^{n+1/2} \quad (2.46c)$$

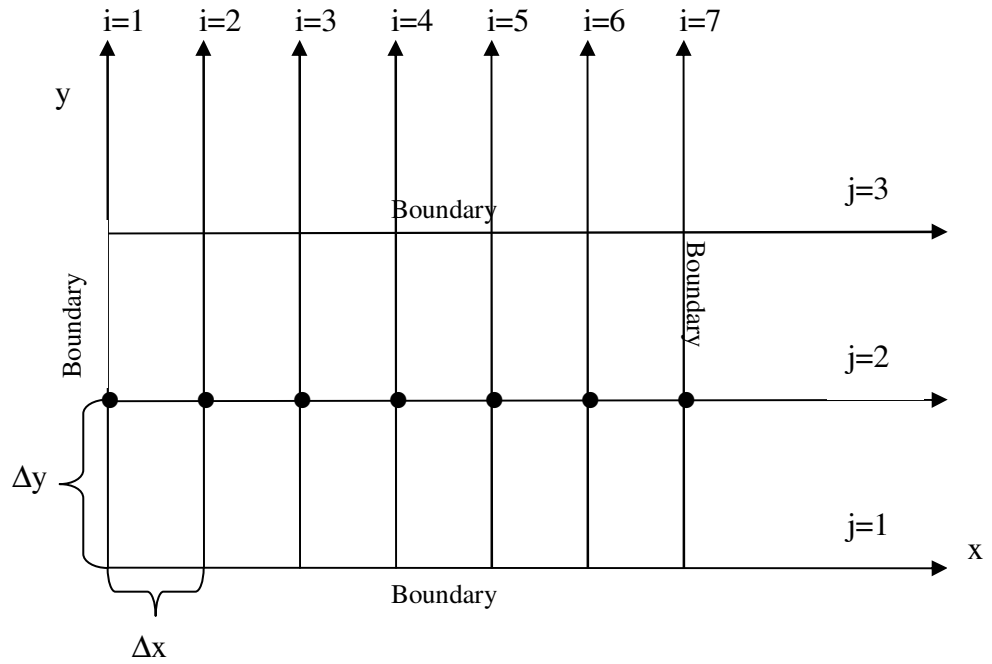


Figure 2.5: 2-D View of 7x3 grid

Hereafter, the superscripts of the equations between (2.44a) to (2.45f) have been dropped out for convenience. Because it is obvious that same procedure can be applied any step of the ADI method which coordinate system is considered for the problem.

$$\begin{bmatrix} -B & A & 0 & 0 & 0 \\ A & -B & A & 0 & 0 \\ 0 & A & -B & A & 0 \\ 0 & 0 & A & -B & A \\ 0 & 0 & 0 & A & -B \end{bmatrix} \begin{bmatrix} \Psi_{2,2} \\ \Psi_{3,2} \\ \Psi_{4,2} \\ \Psi_{5,2} \\ \Psi_{6,2} \end{bmatrix} = \begin{bmatrix} K'_2 \\ K_3 \\ K_4 \\ K_5 \\ K'_6 \end{bmatrix} \quad (2.47)$$

Known values are carried to the right side of the equation, coefficient matrix and vector of the unknown values are stayed on the left side of the matrix.

ADI methodology is going to be used for the spherical coordinate system sweep by sweep in r, θ, ϕ ordinates respectively with previously defined coefficients in equations (2.36), (2.39) and (2.42).

The resulting system can be illustrated in the following way; in which dimensions of the coefficients matrix is $(NR-2) \times (NR-2)$ in its original form. Boundary values has to be taken into consideration because they are going to effect the first and the last row of the matrix which is going to constitute the right hand side of the equation. NR is the number of nodes in the r -direction. This will be replaced by NTETA and NPHI in the subsequent θ and ϕ sweeps.

First Step: r-Sweep

Boundary conditions are known in this problem (consider boundaries have dirichlet boundary constraint) and investigate formulation for beginning and end points. Revert to equation (2.36);

$$i=2, j=2, k=2 \rightarrow -B_2 \cdot \Psi_{2,2,2}^{n+1/3} + C_2 \cdot \Psi_{3,2,2}^{n+1/3} = K_2 - A_2 \cdot \Psi_{1,2,2}^{n+1/3} \quad (2.47a)$$

$$-B_2 \cdot \Psi_{2,2}^{n+1/3} + C_2 \cdot \Psi_{3,2}^{n+1/3} = K'_2 \quad (2.47b)$$

where

$$K'_2 = K_2 - A \cdot \Psi_{1,2,2}^{n+1/3} \quad (2.47c)$$

$$i=NR-1, j=2, k=2 \rightarrow A_{NR-1} \cdot \Psi_{NR-2,2,2}^{n+1/3} - B_{NR-1} \cdot \Psi_{NR-1,2,2}^{n+1/3} = K_{NR-1} - C_{NR-1} \cdot \Psi_{NR,2}^{n+1/3} \quad (2.47d)$$

$$A_{NR-1} \cdot \Psi_{NR-2,2}^{n+1/3} - B_{NR-1} \cdot \Psi_{NR-1,2}^{n+1/3} = K'_{NR-1} \quad (2.47e)$$

where

3. MATHEMATICAL MODELING IN PROLATE SPHEROIDAL COORDINATE SYSTEM

In this section, potential flow equation in prolate spheroidal system and numerical approach to the equations are going to be investigated. Start again with the Laplace equation which is a elliptic second order partial differential equation.

$$\nabla^2\psi = 0 \quad (3.1)$$

ψ is a potential function in three spatial dimensions,

$$\psi = \psi(\eta, \theta, \phi) \quad (3.2)$$

where

$$0 \leq \eta \leq \infty \quad (3.3a)$$

$$0 \leq \theta \leq \pi \quad (3.3b)$$

$$0 \leq \phi \leq 2\pi \quad (3.3c)$$

Conversion from prolate spheroidal coordinates to the Cartesian coordinates can be made using following equations;

$$x = a\text{Sinh}(\eta)\text{Sin}(\theta)\text{Cos}(\phi) \quad (3.4)$$

$$y = a\text{Sinh}(\eta)\text{Sin}(\theta)\text{Sin}(\phi) \quad (3.5)$$

$$z = a\text{Cosh}(\eta)\text{Cos}(\theta) \quad (3.6)$$

The Laplace equation (3.1) expressed in the prolate spheroidal coordinates takes the form;

$$\nabla^2\psi = \frac{1}{a^2(\text{Sinh}^2(\eta) + \text{Sin}^2(\theta))} \left[\frac{\partial^2\psi}{\partial\eta^2} + \text{Coth}(\eta)\frac{\partial\psi}{\partial\eta} + \frac{\partial^2\psi}{\partial\theta^2} + \text{Cot}(\theta)\frac{\partial\psi}{\partial\theta} \right]$$

$$+\frac{1}{a^2\text{Sinh}^2(\eta)\text{Sin}^2(\theta)}\frac{\partial^2\Psi}{\partial\phi^2}=0 \quad (3.7)$$

Trigonometric term in equation (3.7) denominator causes a problem in the numerical calculations and therefore it should be eliminated from the equation. It will lead to singularity when $\eta=0$ or $\theta=0$ in the discretized form. Hence multiplying both sides of equation (3.7) by $a^2\text{Sinh}^2(\eta)\text{Sin}^2(\theta)$; then we obtain ;

$$\nabla^2\Psi = \frac{\text{Sinh}^2(\eta)\text{Sin}^2(\theta)}{\text{Sinh}^2(\eta)+\text{Sin}^2(\theta)}\left[\frac{\partial^2\Psi}{\partial\eta^2}+\text{Coth}(\eta)\frac{\partial\Psi}{\partial\eta}+\frac{\partial^2\Psi}{\partial\theta^2}+\text{Cot}(\theta)\frac{\partial\Psi}{\partial\theta}\right]+\frac{\partial^2\Psi}{\partial\phi^2} \quad (3.8)$$

Simplification for the equation (3.8) will ease the discretization, hence, define a dummy function $Z(\eta,\theta)$

$$Z(\eta,\theta) = \frac{\text{Sinh}^2(\eta)\text{Sin}^2(\theta)}{\text{Sinh}^2(\eta)+\text{Sin}^2(\theta)} \quad (3.9)$$

After substitution of the dummy function to equation (3.8), discretized Laplace equation with first order finite difference approximation, we obtain;

$$Z(\eta,\theta)\left[\frac{\Psi_{i+1,j,k}-2\Psi_{i,j,k}+\Psi_{i-1,j,k}}{(\Delta\eta)^2}+\text{Coth}(\eta)\left(\frac{\Psi_{i+1,j,k}-\Psi_{i-1,j,k}}{2\Delta\eta}\right)+\frac{\Psi_{i,j+1,k}-2\Psi_{i,j,k}+\Psi_{i,j-1,k}}{(\Delta\theta)^2}+\text{Cot}(\theta)\frac{\Psi_{i,j+1,k}-\Psi_{i,j-1,k}}{2\Delta\theta}\right]+\frac{\Psi_{i,j,k+1}-2\Psi_{i,j,k}+\Psi_{i,j,k-1}}{(\Delta\phi)^2}=0 \quad (3.10)$$

There is still trigonometric term in the denominator of equation (3.10). It will cause discontinuity while θ approaches 0. Therefore, multiply both side of the equation with $\text{Sin}(\theta)$,

$$Z(\eta,\theta)\left[\text{Sin}(\theta)\left(\frac{\Psi_{i+1,j,k}-2\Psi_{i,j,k}+\Psi_{i-1,j,k}}{(\Delta\eta)^2}\right)+\text{Sin}(\theta)\text{Coth}(\eta)\left(\frac{\Psi_{i+1,j,k}-\Psi_{i-1,j,k}}{2\Delta\eta}\right)\right. \\ \left.\text{Sin}(\theta)\frac{\Psi_{i,j+1,k}-2\Psi_{i,j,k}+\Psi_{i,j-1,k}}{(\Delta\theta)^2}+\text{Cos}(\theta)\frac{\Psi_{i,j+1,k}-\Psi_{i,j-1,k}}{2\Delta\theta}\right] \\ +\text{Sin}(\theta)\frac{\Psi_{i,j,k+1}-2\Psi_{i,j,k}+\Psi_{i,j,k-1}}{(\Delta\phi)^2}=0 \quad (3.11)$$

If the notation stated in Figure (2.1.1), equation (3.11) coefficients can be obtained as follows ;

$$PP = \left[-\frac{2Z(\eta, \theta)\text{Sin}(\theta)}{(\Delta\eta)^2} - \frac{2Z(\eta, \theta)\text{Sin}(\theta)}{(\Delta\theta)^2} - \frac{2\text{Sin}(\theta)}{(\Delta\phi)^2} \right] \quad (3.12a)$$

$$PW = \left[\frac{Z(\eta, \theta)\text{Sin}(\theta)}{(\Delta\eta)^2} - \frac{Z(\eta, \theta)\text{Coth}(\eta)\text{Sin}(\theta)}{2\Delta\eta} \right] \quad (3.12b)$$

$$PE = \left[\frac{Z(\eta, \theta)\text{Sin}(\theta)}{(\Delta\eta)^2} + \frac{Z(\eta, \theta)\text{Coth}(\eta)\text{Sin}(\theta)}{2\Delta\eta} \right] \quad (3.12c)$$

$$PN = \left[\frac{Z(\eta, \theta)\text{Sin}(\theta)}{(\Delta\theta)^2} + \frac{Z(\eta, \theta)\text{Cos}(\theta)}{2\Delta\theta} \right] \quad (3.12d)$$

$$PS = \left[\frac{Z(\eta, \theta)\text{Sin}(\theta)}{(\Delta\theta)^2} - \frac{Z(\eta, \theta)\text{Cos}(\theta)}{2\Delta\theta} \right] \quad (3.12e)$$

$$PL = \left[\frac{\text{Sin}(\theta)}{(\Delta\phi)^2} \right] \quad (3.12f)$$

$$PU = \left[\frac{\text{Sin}(\theta)}{(\Delta\phi)^2} \right] \quad (3.12g)$$

Substituting the coefficient to the governing Laplace Equation which was denoted in discrete form in equation (3.11) takes the form;

$$\begin{aligned} PP \bullet \psi_{i,j,k} + PW \bullet \psi_{i-1,j,k} + PE \bullet \psi_{i+1,j,k} + PN \bullet \psi_{i,j+1,k} \\ + PS \bullet \psi_{i,j-1,k} + PU \bullet \psi_{i,j,k+1} + PL \bullet \psi_{i,j,k-1} = 0 \end{aligned} \quad (3.13)$$

If terms are rearranged with Gauss-Seidel iteration method, equation (3.13) takes form;

$$\begin{aligned} \psi_{i,j,k}^{m+1} = \frac{-1}{PP} \left[PW \bullet \psi_{i-1,j,k}^{m+1} + PE \bullet \psi_{i+1,j,k}^m + PS \bullet \psi_{i,j-1,k}^{m+1} \right. \\ \left. + PN \bullet \psi_{i,j+1,k}^m + PL \bullet \psi_{i,j,k-1}^{m+1} + PU \bullet \psi_{i,j,k+1}^m \right] = 0 \end{aligned} \quad (3.13)$$

For further vector algebra and mathematical operations in fluid mechanics please look in **Owczarek (1968)** Appendix A section.

4. GRID GENERATION

The partial differential equations that governs fluid flow and heat transfer are not usually proper to analytical solutions, except for very plain cases. Therefore, in order to analyze fluid flows, flow domains are split into smaller subdomains and discretized governing equations are solved inside each of these portions of the domain. Typically, one of three methods is used to solve the approximate version of the system of equations: finite volume, finite elements or finite differences. In this thesis finite difference method is selected and in the preceding sections, the fundamental equations that belongs to velocity potential for the cartesian, spherical and prolate spheroidal coordinates are solved. Commencement process should be start with defining the physical space and computational space of the region. **Knupp (1993)** stated that before a grid can be generated that, a physical object must be specified mathematically; this can be done by specifying its boundaries. Then, care must be taken to ensure proper continuity of solution across the common interfaces between two subdomains, so that the approximate solution inside various portions can be put together to give a complete picture of fluid flow in the entire domain. Each of these portions of the domain are known as elements or cells, and the collection of all elements is known as grid or mesh.

There are too many possibilities to determine the boundaries for physical objects. For Example **Knupp (1993)** stated that there is a possibility to transform the physical region to a square in two dimensions or a cube in three dimensions for many complicated application. Boundary conditions of the physical region is going to be coincident with the square or the cube boundaries which is transformed (see Figure 4.1 for square example).

Hoffmann (1989) stated that boundaries of the physical domain can be associated with the grid points, therefore boundary conditions specification can be done with less effort. Unfortunately, most of the physical domains of interest are

nonrectengular. Hence, boundary conditions need some interpolation for implementation while physical domain transforming to rectangular domain

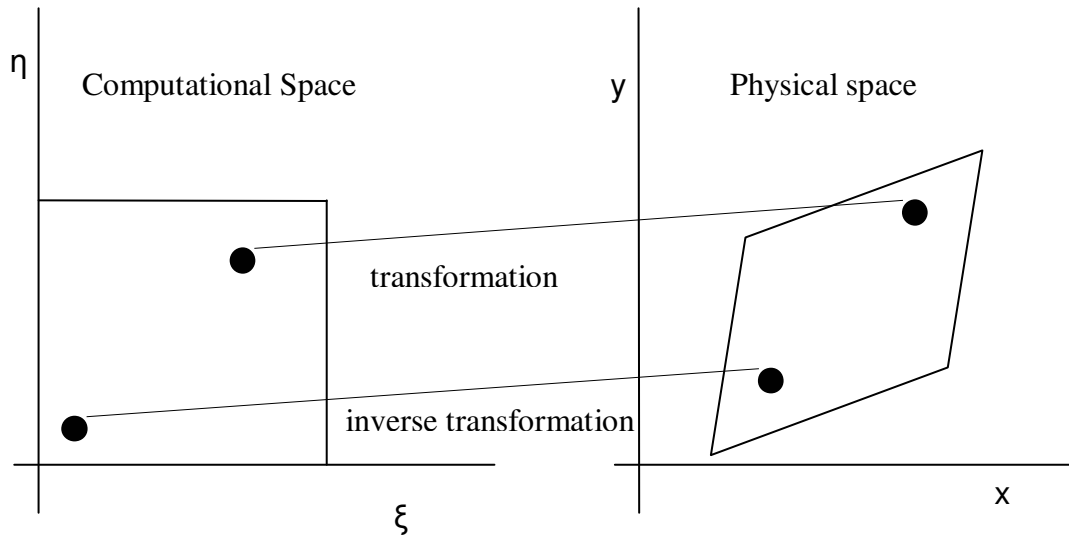


Figure 4.1: Transformation of coordinate system

4.1 General Methods

The region where the flow is going to be investigated, is splitted up into a geometrical elements. As said before, these elements is called grid cells and this process named as grid generation. Also, the grid generation can be examined by putting grid points into the physical space then connecting them by straight lines (these lines are termed grid lines). There are 2 crucial points while generating grids in the physical space;

- 1.) There must no holes between the grid cells
- 2.) Grid cells do not overlap

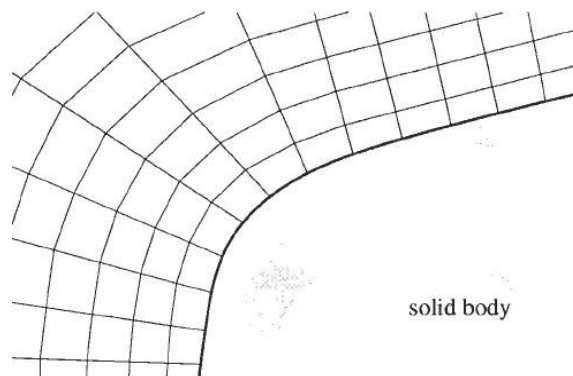


Figure 4.2: Form Fitted Grid Example (Blazek 2001 p.31)

Moreover, the structure of grid should be smooth as possible. If abrupt changes in the volume and in the stretching ratio between sequential cells occur, it will increase significant numerical errors. The grid generation can be formed either by form-fitted type which follows closely the boundaries of the physical space (shown in figure 4.2) and cartesian type where the edges of the grid cells are oriented in parallel to the cartesian coordinates (shown in figure 4.3) (**Blazek, 2001**).

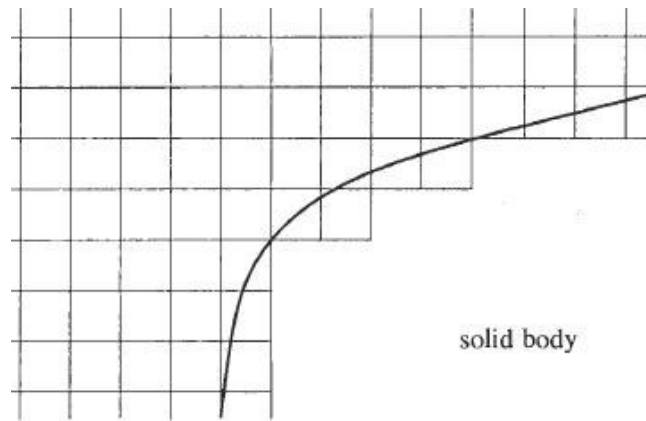


Figure 4.3: Cartesian Grid Example (Blazek 2001 p.31)

Main advantage of the form-fitted grid is; at the boundaries flow can be monitored precisely, it is very important while investigating shear layer along solid bodies. However, grid construction in the domain and calculation of fluid flux operations can be done with performing less effort with Cartesian Grid even it is harder to examine flow treatment near boundaries (**Coirier, 1995**). Body-fitted grid schema is preferred for the industrial problems, generally which have more sophisticated configuration, because behaviour of the fluid near boundaries is desired to observe with higher accuracy (**Blazek, 2001**).

In a typical manner, rectangular shape where distribution of grid points are in sequence order along grid lines is preferred for the computational domain. Hence, the reference of grid points may be easily identified with using appropriate grid lines. Nevertheless, uniform grid interval can ease the process of grid generation in a rectangular physical domain (**Hoffmann 1989**).

As mentioned before, element structure is the another crucial point for grid generation. The elements in a mesh can be classified in various ways. The easiest is based upon the dimension and type of the elements. Common elements in 2-D are triangles or rectangles, and common elements in 3-D are tetrahedra or bricks. The

most basic form of mesh classification is based upon the connectivity of the mesh and algorithms shortly be summarized as,

A) Structured Methods

1. Algebraic Grid Generation
2. Elliptic Grid Generation
3. Conformal Mappings

B) Unstructured Methods

1. Octree Method
2. Delaunay Method
3. Advancing Front

C) Hybrid Methods

Another categorization can be made to the solution based point of view and it called fixed or adaptive type. Grid which discretizes the continuous domain of interest may be static, established once and for all the domain at the beginning of the computation that it is called as fixed or it may be dynamic tracking the features of results while the calculation still in progress. Adaptive grid domain evolve itself to establish best approximation around the problematic vicinity (**Plewa et. al. 2005**).

As a consequence, in this study formed grids should satisfy both body-fitted and rectangular shaped element features as possible as could it be and it is considered to be fixed type. Moreover, the generated grids are formed with algebraic methods which is introduced under structured methods.

4.2 Forming Computational Domain

As mentioned before two kind of fundamental equation is going to be investigated;

1. Heat Conduction
2. Potential Flow

Below mentioned fundamental equations will be solved on node points and both of the equations will be applied to the spherical and the prolate spheroidal physical domains respectively. Therefore, two kinds of transformation is going to be placed in this thesis.

Transformation to spherical coordinates to rectangular coordinates for axes can be done with the below mentioned equations (**Moon 1988**);

$$x = r\sin(\theta)\cos(\phi) \quad (4.1)$$

$$y = r\sin(\theta)\sin(\phi) \quad (4.2)$$

$$z = r\cos(\theta) \quad (4.3)$$

θ is the angle between Z and Y ordinates, ϕ is the angle between X and Y ordinates and r is the radius of the sphere inside the below designated borders.

$$0 \leq r \leq \infty \quad (4.4a)$$

$$0 \leq \theta \leq \pi \quad (4.4b)$$

$$0 \leq \phi \leq 2\pi \quad (4.4c)$$

Ordinates and related angles can be seen in Figure (4.4).

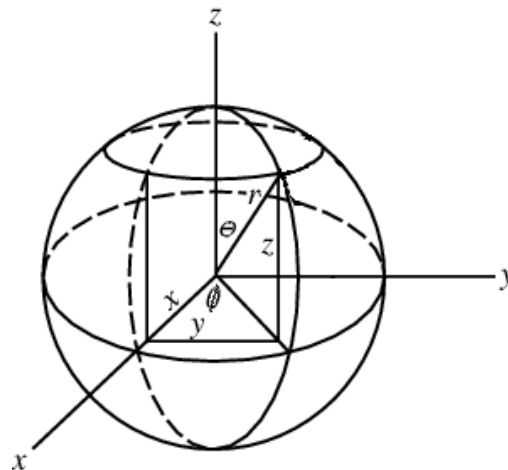


Figure 4.4: Spherical Coordinate's Projection (Calculus 1998 p.534)

Beginning stage of grid generation in spherical coordinate system is the determination of the borders. In first experiment there would be two spheres. One sphere is encompassed by another sphere. Sphere bodies are symmetric in three ordinate. Therefore it will be easy to implement sweep philosophy. In second stage, determination of location of the node points in r-ordinate is executed. Then, sweep operation is applied to the line, which node points previously localized, between 0 to π in θ -direction. Generated fan is shown in Figure (4.5).

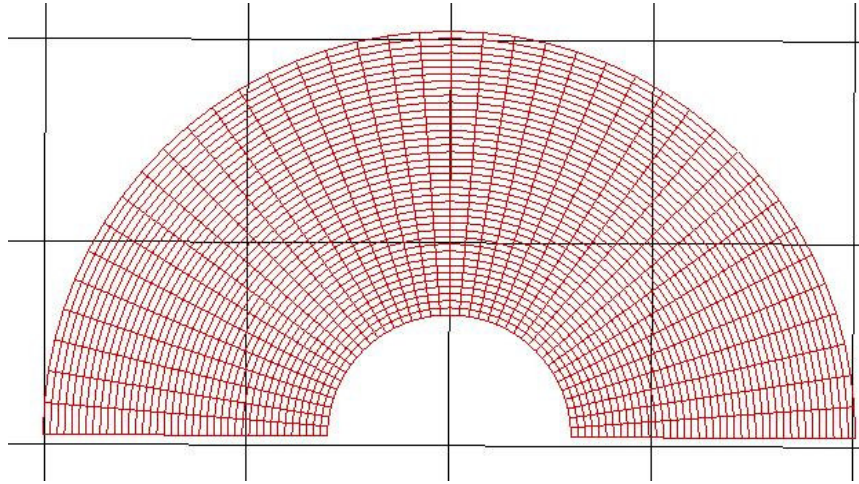


Figure 4.5: 2-D View of Generated Fan

Last step is the revolving fan through its edges around ϕ angle from 0 to 2π . Revolved fan in 2 dimensions and formed grid in 3 dimensions is shown in Figure (4.6). As clearly seen Figure (4.5) and Figure (4.6), form fitted grid type is successfully generated around inner sphere. Additionally desired rectangular shaped elements perfectly generated inside the domain.

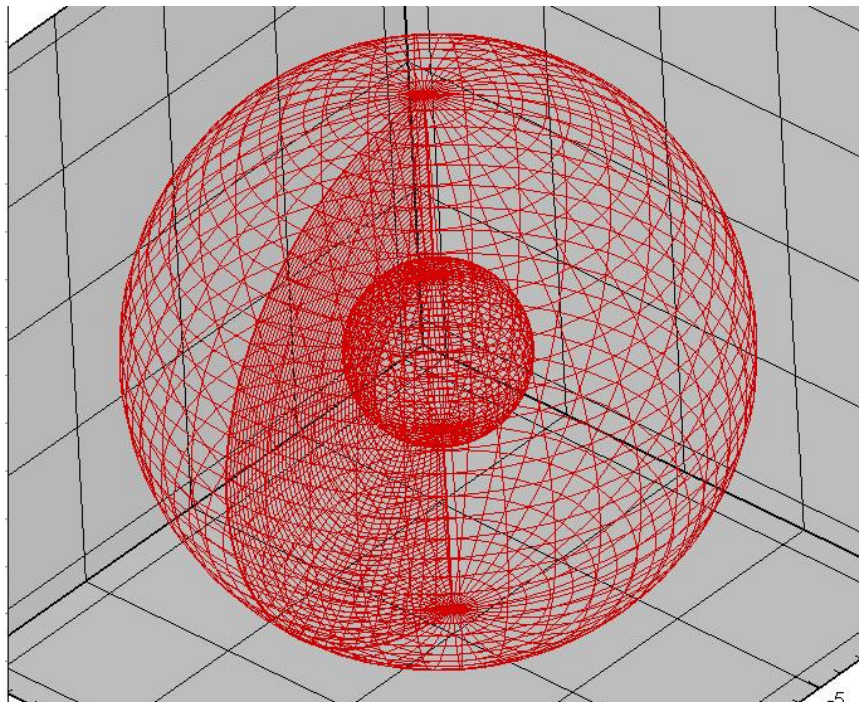


Figure 4.6: 3-D View of Generated Grid

Transformation to prolate spheroidal coordinates to rectangular coordinates for axes can be done with the below mentioned equations (**Moon 1988**) within previously

mentioned borders (Equation 3.3a to 3.3c). Ordinates and related angles can be seen in Figure (4.7).

$$x = a\text{Sinh}(\eta)\text{Sin}(\theta)\text{Cos}(\phi) \quad (4.4)$$

$$y = a\text{Sinh}(\eta)\text{Sin}(\theta)\text{Sin}(\phi) \quad (4.5)$$

$$z = a\text{Cosh}(\eta)\text{Cos}(\theta) \quad (4.6)$$

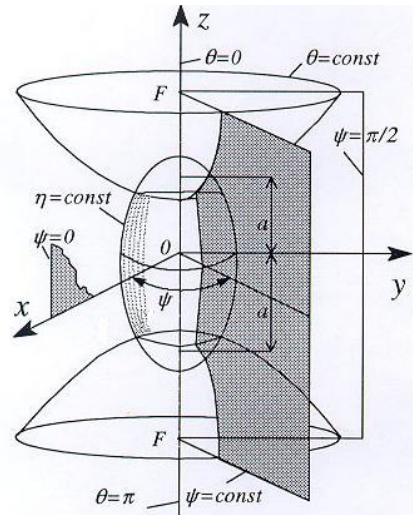


Figure 4.7: Prolate Spheroidal Coordinate's Projection (Moon 1988 p. 31)

Beginning stage of grid generation in prolate spheroidal coordinate system is the determination of the borders. This time there would be a Prolate Spheroidal body which is encompassed by a sphere. Prolate Spheroidal body is symmetric to Z ordinate. Therefore, after determination of location of the node points in η -ordinate, sweep operation will be executed in θ -direction between 0 to π . Generated fan is shown in Figure (4.8).

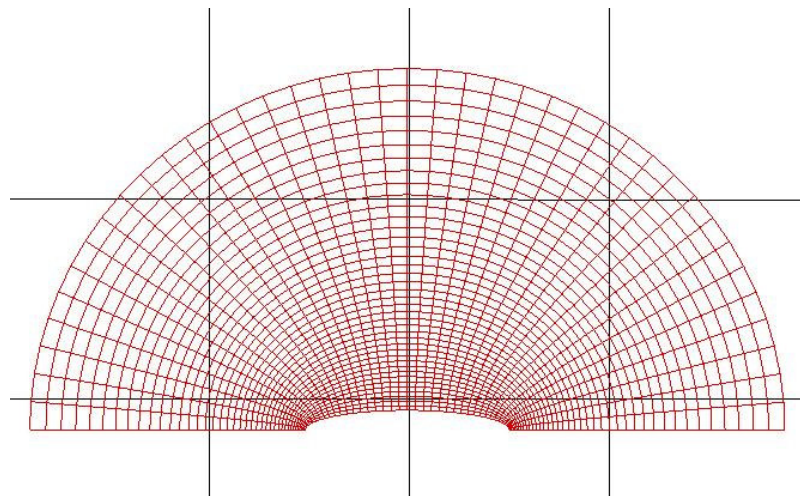


Figure 4.8: 2-D View of Generated Fan

Last step is the revolving fan through it's edges around ϕ angle from 0 to 2π . Revolved fan in 2 dimensions and formed grid in 3 dimensions is shown in Figure (4.9).

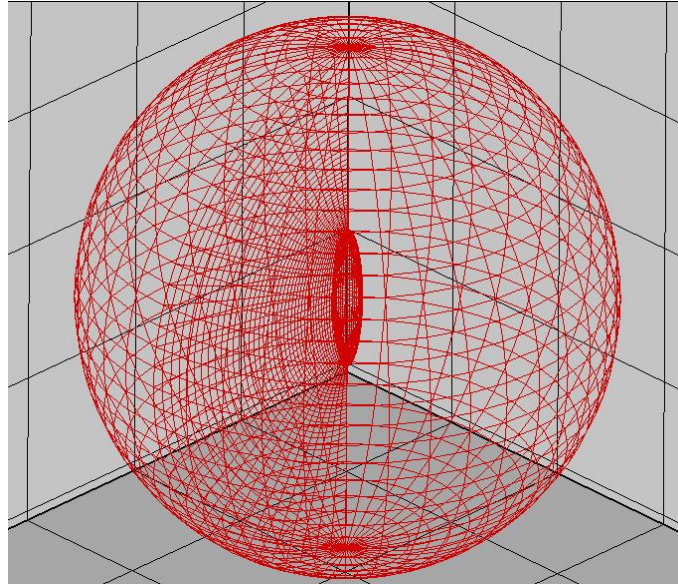


Figure 4.9: 3-D View of Generated Grid.

Form fitted grid type around prolate spheroidal body is accomplished. Moreover, desired rectangular shaped elements perfectly generated inside the domain. More detailed pictures around body and the pole point which can not clearly seen in Figure (4.8) and (4.9) are given in Figures (4.10) and (4.11).

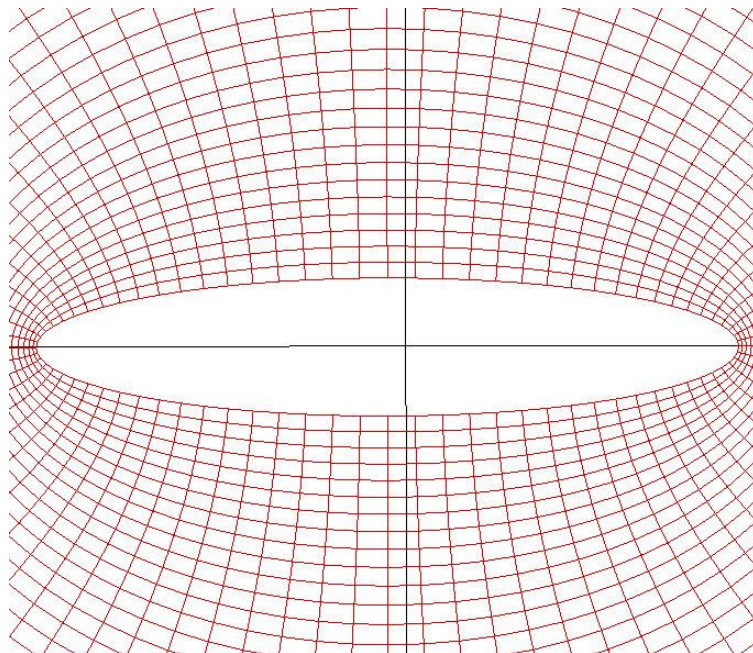


Figure 4.10: Form Fitted Grid Around a Prolate Spheroidal Body

Adjacent view of the pole region is shown in Figure (4.11).

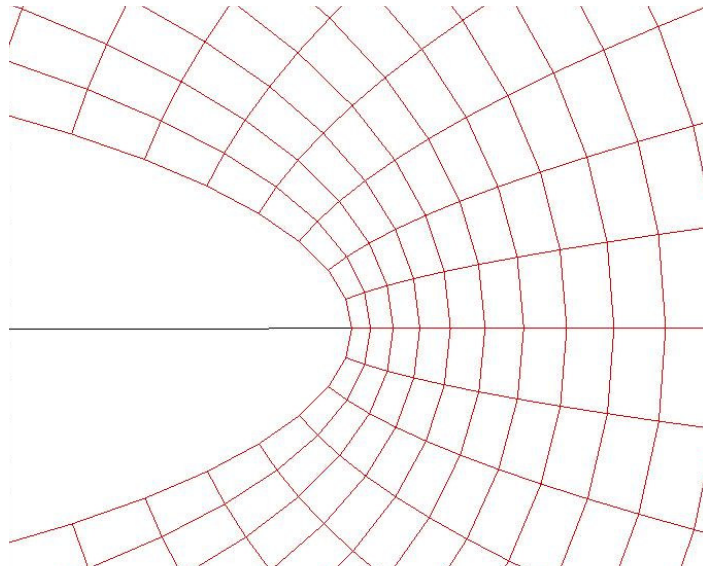


Figure 4.11: Enlarged View of the Pole Region

In Figure (4.11) it is seen that outer border of the prolate spheroid body is formed with the conjunction of the lines. Exact shape can be achieved, if the amount of the node number is increased. However, there is a major problem which is related with the node number for external flows. **Hoffmann (1989)** summarize problem as; any given problem may be considered either as an internal flow problem or an external flow problem. The selection of the computational domain for internal flows is relatively simple, because the domain of the solution can be uniquely identified based on the well defined physical domain. On the other hand, the selection of computational domain for external flow is not simple. The boundaries of such domains will include artificial boundaries set in the free stream (far field). The difficulty is primarily associated with the specifications of farfield boundary associated with external flow. Ideally, the location of the farfield boundary should be set as far as possible. However, from the practical point of view, this is not a viable option. Since one is limited in the number of grid points and since one ideally would like to maximize the grid points density to increase accuracy, a finite computational domain must be selected.

Therefore, from efficiency point of view, number of grid points and computational domain must be selected in parallelism of the needs. If accuracy requirement are excessive, node number will be enhanced but, it extends computational time. To abate the time problem for external flow problems, grid reduction should be applied

and grids close to the free stream (far field) are formed coarse as it could be (Ferziger 2002).

Proportional node spans' increment in θ direction while advancing to the free stream (far field) is clearly shown in Figure (4.12).

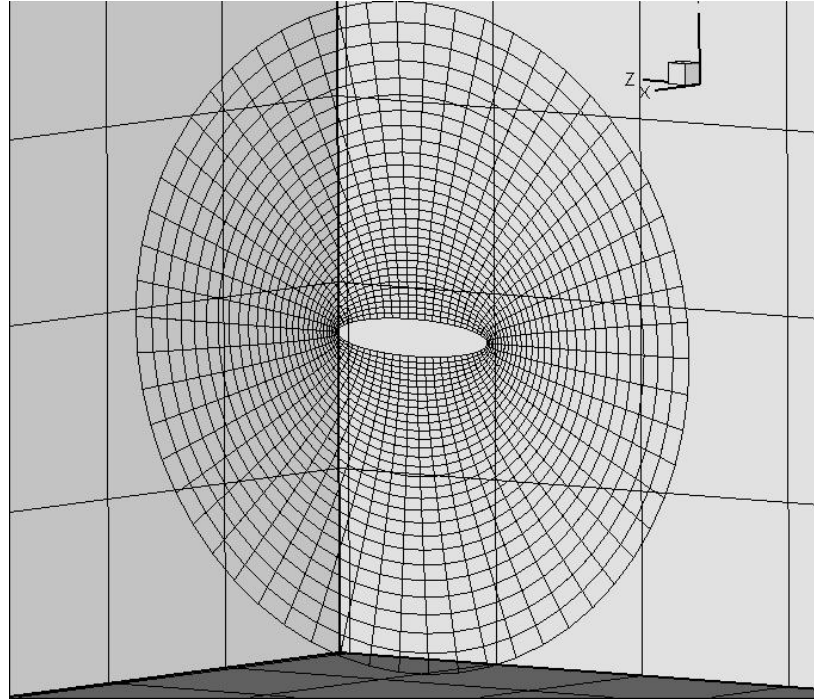


Figure 4.12: Cross Sectional View of the Prolate Spheroidal Body Grid

5. NUMERICAL RESULTS

In this section, the Fortran codes which are written to solve 3-D heat and potential flow problems are going to be introduced. Codes, have modules to produce grid for desired geometries which are briefly mentioned in previous section and solve discretized fundamental equations inside the interior domains and give results which are arranged in matrix form. After obtaining data from Fortran code, Tech Plot program which enables to monitor the data is used for postprocessing phase of the heat conduction and potential flow equations results around concerned bodies both in constructed in spherical and prolate spheroidal coordinates.

In first two subsections, heat transfer equation in spherical and oblate spheroidal layout are investigated. In last two subsections, potential flow around both in spherical and prolate spheroidal bodies are investigated. Additionally, boundary conditions –both for interior and exterior borders- which have important role while the iteration proceeding are mentioned in this section.

5.1 Solution of the Heat Equation in Spherical Polar Coordinates

First of all, physical domain is going to be constructed. Assume a domain between two 3-D sphere shells. One of them is smaller than the other one and the smaller sphere located in the middle of the larger sphere. Smaller one is assumed to be a rigid 3-D body. Nevertheless, assume interior/exterior spheres have a steady temperature values and they do not change in time domain. Heat conduction is going to be solved in the volume which is between two spheres. Schematic view of the problem is given in Figure (5.1).

Heat Conduction equation in spherical coordinates is,

$$\frac{\partial T}{\partial t} = \alpha \left(\frac{\partial^2 T}{\partial r^2} + \frac{2}{r} \frac{\partial T}{\partial r} + \frac{1}{r^2} \frac{\partial^2 T}{\partial \theta^2} + \frac{\cot(\theta)}{r^2} \frac{\partial T}{\partial \theta} + \frac{1}{r^2 \sin^2 \theta} \frac{\partial^2 T}{\partial \phi^2} \right) \quad (5.1)$$

If heat conduction problem assumed as steady, equation (5.1) becomes;

$$\left(\frac{\partial^2 T}{\partial r^2} + \frac{2}{r} \frac{\partial T}{\partial r} + \frac{1}{r^2} \frac{\partial^2 T}{\partial \theta^2} + \frac{\text{Cot}(\theta)}{r^2} \frac{\partial T}{\partial \theta} + \frac{1}{r^2 \text{Sin}^2 \theta} \frac{\partial^2 T}{\partial \phi^2} \right) = 0 \Leftrightarrow \nabla^2 T = 0 \quad (5.2)$$

If first order central difference approximation is applied with using same considerations for equation (2.14), the following equation will be obtained for steady heat conduction which is in spherical coordinate system;

$$\begin{aligned} r_{i,j,k}^2 \text{Sin}^2 \theta_{i,j,k} \left[\frac{T_{i-1,j,k} - 2T_{i,j,k} + T_{i+1,j,k}}{\Delta r_{i,j,k}^2} \right] + 2r_{i,j,k} \text{Sin}^2 \theta_{i,j,k} \left[\frac{T_{i+1,j,k} - T_{i-1,j,k}}{2\Delta r_{i,j,k}} \right] \\ + \text{Sin}^2 \theta_{i,j,k} \left[\frac{T_{i,j-1,k} - 2T_{i,j,k} + T_{i,j+1,k}}{\Delta \theta_{i,j,k}^2} \right] + \text{Sin} \theta_{i,j,k} \text{Cos} \theta_{i,j,k} \left[\frac{T_{i,j+1,k} - T_{i,j-1,k}}{2\Delta \theta_{i,j,k}} \right] \\ + \left[\frac{T_{i,j,k-1} - 2T_{i,j,k} + T_{i,j,k+1}}{\Delta \phi^2} \right] = 0 \end{aligned} \quad (5.3)$$

Revert back to Equation (2.22) and rewrite the same for solution of the three dimensional heat conduction.

$$\begin{aligned} T_{i,j,k}^{m+1} = \frac{-1}{\text{GSP}} \left[\text{GSW} \cdot T_{i-1,j,k}^{m+1} + \text{GSE} \cdot T_{i+1,j,k}^m + \text{GSS} \cdot T_{i,j-1,k}^{m+1} \right. \\ \left. + \text{GSN} \cdot T_{i,j+1,k}^m + \text{GSL} \cdot T_{i,j,k-1}^{m+1} + \text{GSU} \cdot T_{i,j,k+1}^m \right] = 0 \end{aligned} \quad (5.4)$$

Open forms of the coefficients GSW, GSE, GSN, GSS, GSU, GSL and GSP have already been given in Chapter (2).

Regarding the boundary conditions **Hoffmann (1989)** stated that, a unique and accurate solution for a given system of PDEs within a domain can be obtained only when proper boundary conditions are specified. Depending on the particular application, some of the boundary conditions are provided from the physics of the problem, however, in general not all the boundary conditions are known apriori. Therefore, not only the flow properties may be unknown within the domain of the solution, some of the unknowns on the boundaries can not be arbitrarily specified. These values depend on the solution of the interior domain as well as information provided from the exterior. The boundaries of any domain may be composed of;

1. Solid Surface
2. Free Stream Boundary of Far Field Boundary Composed of inflow and/or outflow
3. Symmetric Boundary
4. Branch Cut
5. Periodic Boundary.

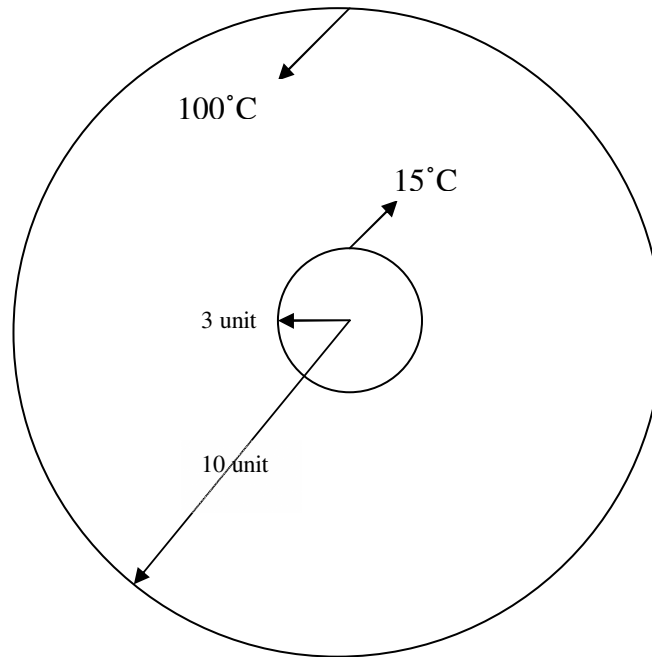


Figure 5.1: Schematic 2-D view of Subsection (5.1).

Solid Surface boundary condition is convenient for investigated heat conduction problem. Because, the value of the boundaries do not change in time domain in other words they are steady. Therefore, this type of boundary condition is named Dirichlet condition (**Blazek, 2001**).

In this case (as mentioned before) smaller sphere is assumed to be a solid body, the inner volume of the smaller sphere is out of interest. Outer sphere and smaller sphere conduct heat continuously so, both sphere boundaries are considered as Dirichlet boundary condition. Eventually, present case can be assumed to be heat-conduction problem between the two shells.

Fortran code run the iterative cycle of Equation (5.4). Algorithm of the Fortran program for the heat conduction case is given in Figure (5.4). The code generates the 3-D mesh in desired type and obtain results for all nodes between the mentioned

volume. While obtaining results from the computer following boundary conditions are used;

- 1) Temperature on the surface of the inner sphere: 15°C
- 2) Temperature on the surface of the outer sphere: 100°C

where geometries for the spheres are taken as;

- 1) Inner sphere has a radius of 3 cm
- 2) Outer sphere has a radius of 10 cm

Additionally, an initial guess has been made for the nodes in the region because of faster convergence. 5°C is appointed as initial condition for all nodes in the region.

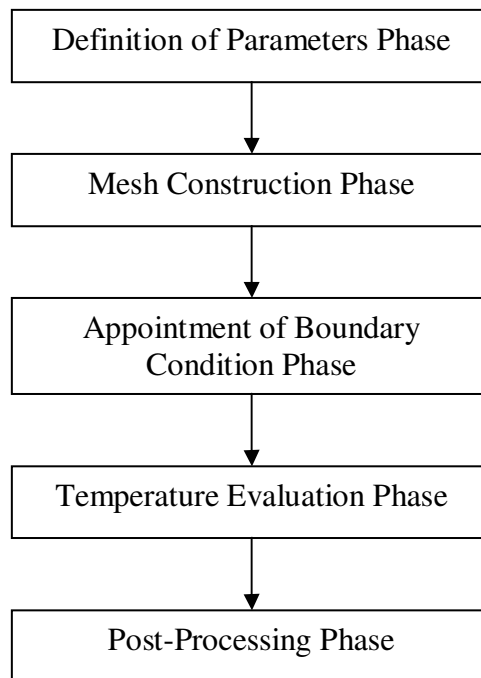


Figure 5.2: Algorithm for the Heat Conduction Problems

Different grid density can be determined by changing node numbers in ordinates, but homogeneous grid distribution is requested for the reasons,

- 1) Sphere domain is axisymmetric (Geometry of domain has same cross-sections in every ordinates).
- 2) Same accuracy is requested in every dimensions (Comparison can be made between the ordinates)

If $41 \times 41 \times 41$ nodes used for the domain; half grid view of the domain is given in Figure (5.3);

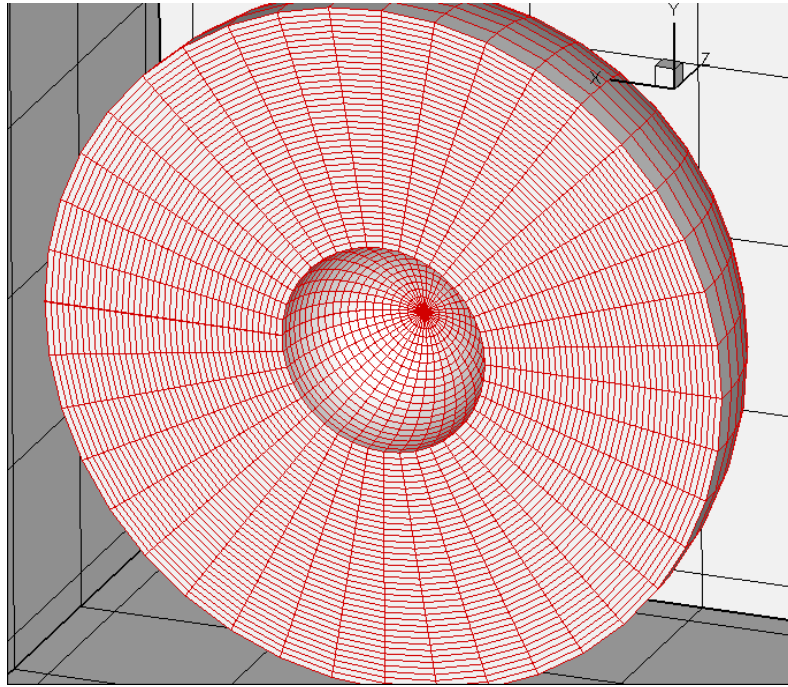


Figure 5.3: Grid View of Half Domain in Spherical Coordinates

Another illustration of the domain is presented in Figure (5.4).

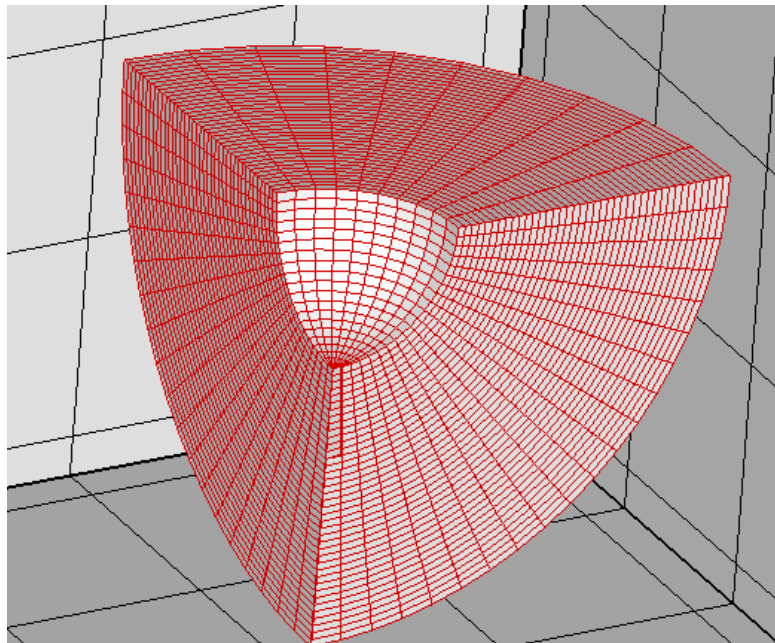


Figure 5.4: Different Aspect of Grid Domain in Spherical Coordinates.

The inner sphere surface which has a uniform temperature at 15°C is represented with blue color and the outer sphere surface which has a uniform temperature at 100°C is represented with red color. Temperature distribution between two sphere

shells is shown in Figure (5.5). Symmetrical temperature distribution can be monitored via legend.

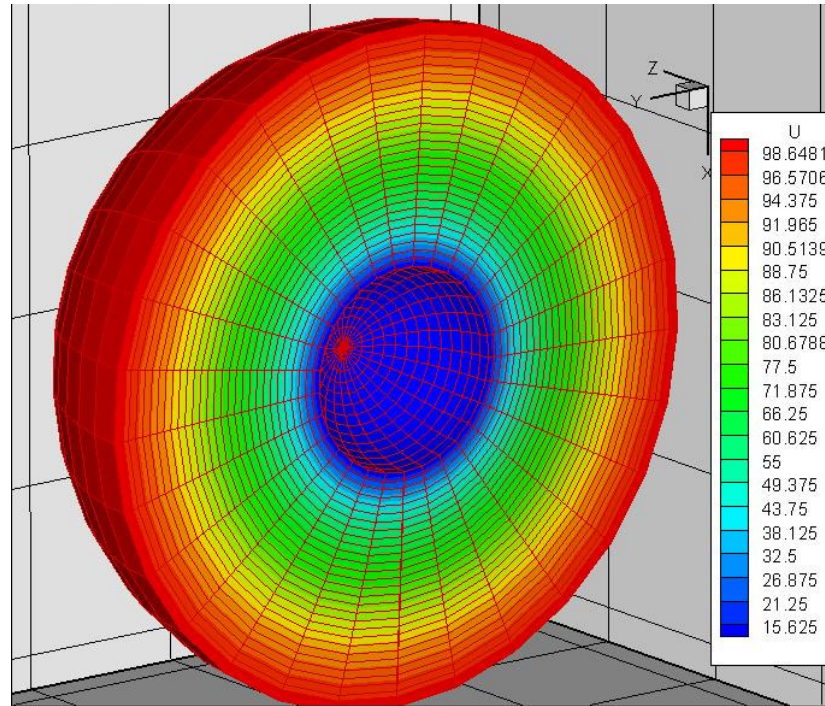


Figure 5.5: Half View of the Results with Grid in Spherical Coordinate

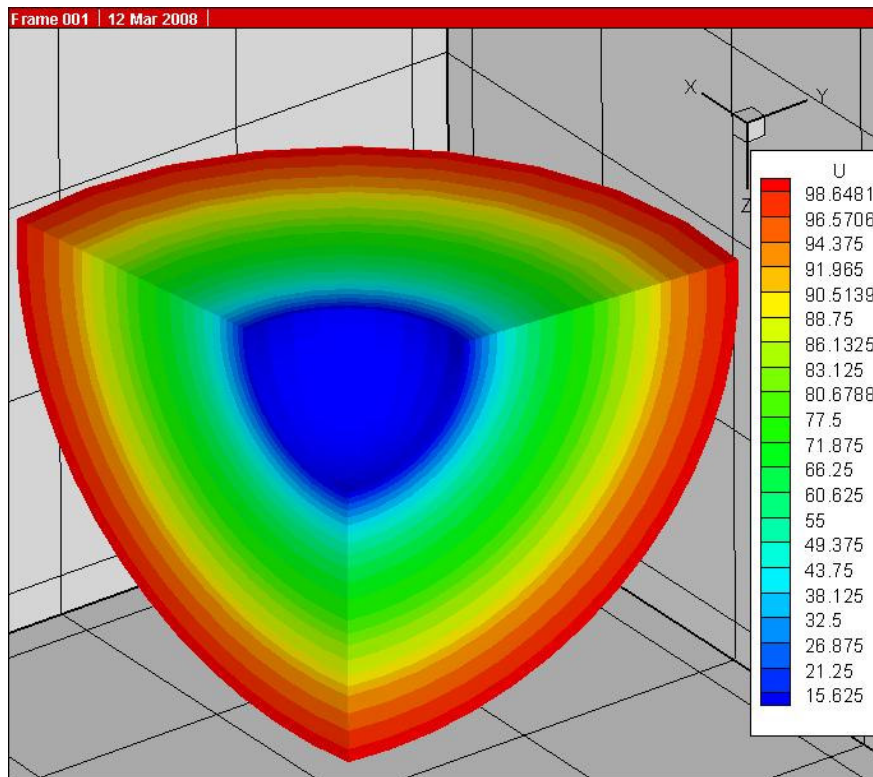


Figure 5.6: Another View of the Results without Grid in Spherical Coordinates

Another cross section of the 3-D physical space is shown in Figure (5.6), homogeneous temperature distribution in 3 dimension precisely can be seen easily in the region.

5.2 Solution of the Heat Equation in Prolate Spheroidal Coordinates

Now same procedure which is applied for spherical coordinates in subsection 5.1 is going to be implemented for the body which is defined in Prolate Spheroidal Coordinates.

If first order central difference approximation is used for heat conduction in prolate spheroidal coordinate, the following equation will be obtained;

$$\begin{aligned}
 Z(\eta, \theta) \left[\sin(\theta) \left(\frac{T_{i-1,j,k} - 2T_{i,j,k} + T_{i+1,j,k}}{(\Delta\eta)^2} \right) + \sin(\theta) \operatorname{Coth}(\eta) \left(\frac{T_{i+1,j,k} - T_{i-1,j,k}}{2\Delta\eta} \right) \right. \\
 \left. \sin(\theta) \frac{T_{i,j-1,k} - 2T_{i,j,k} + T_{i,j+1,k}}{(\Delta\theta)^2} + \cos(\theta) \frac{T_{i,j+1,k} - T_{i,j-1,k}}{2\Delta\theta} \right] \\
 + \sin(\theta) \frac{T_{i,j,k-1} - 2T_{i,j,k} + T_{i,j,k+1}}{(\Delta\phi)^2} = 0 \quad (5.5)
 \end{aligned}$$

* Remember that (see Chapter 3);

$$Z(\eta, \theta) = \frac{\operatorname{Sinh}^2(\eta) \operatorname{Sin}^2(\theta)}{\operatorname{Sinh}^2(\eta) + \operatorname{Sin}^2(\theta)} \quad (5.6)$$

Same iteration approximation which is mentioned in equation (5.4) is used for the Prolate Spheroidal Coordinates except GSW, GSE, GSS, GSN, GSL, GSU coefficients. Open forms of the coefficients for Prolate Spheroidal Body are given in Chapter 3.

Same assumption is going to be done for the Prolate Spheroidal Domain. Again inner body is cold, has a continuous value and outer boundary is warm, has a continuous value. Prolate Spheroidal body is located in the middle of the larger sphere. Additionally, the smaller one is assumed to be a rigid 3-D body. While obtaining results from the computer following boundary conditions are used;

- 1) Temperature on the surface of the inner sphere: 15°C
- 2) Temperature on the surface of the outer sphere: 100°C

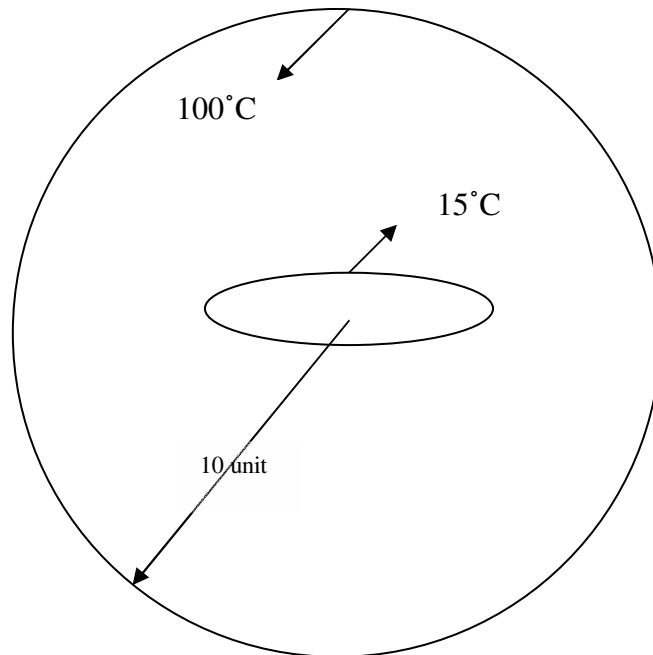


Figure 5.7: Schematic 2-D View of Subsection (5.2)

An initial guess has been made for the nodes in the region because of faster convergence. 20°C is appointed as initial condition for all nodes in the region. Same Algorithm was used which is shown in Figure (5.2) to obtain results.

If $41 \times 41 \times 41$ nodes used for the domain; half grid view of the domain is given in Figure (5.8);

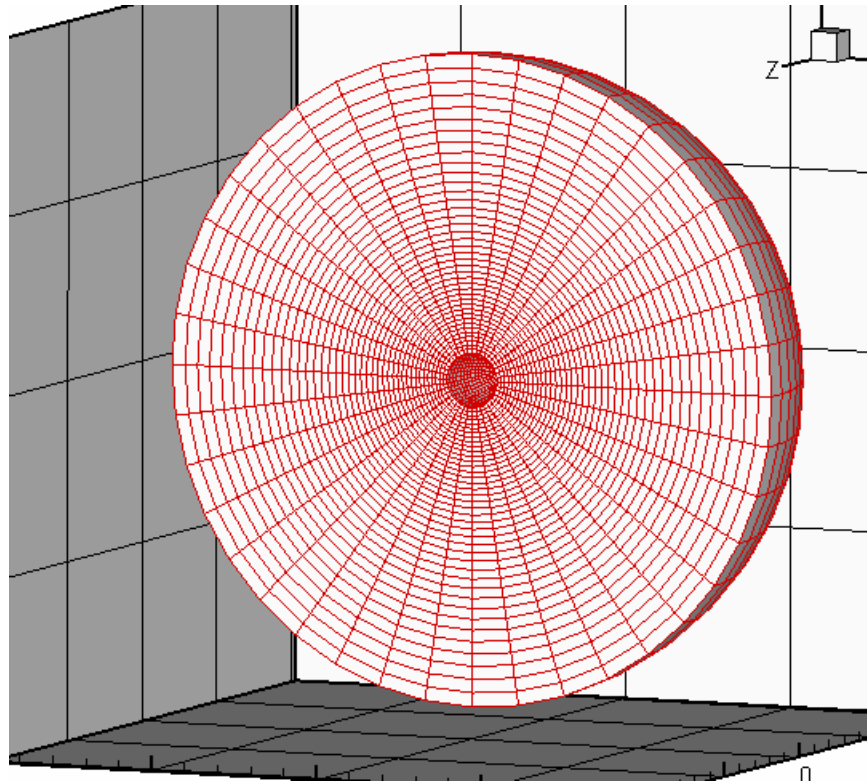


Figure 5.8: Grid View of Half Domain in Prolate Spheroidal Coordinates

Another illustration of the domain is presented in Figure (5.4).

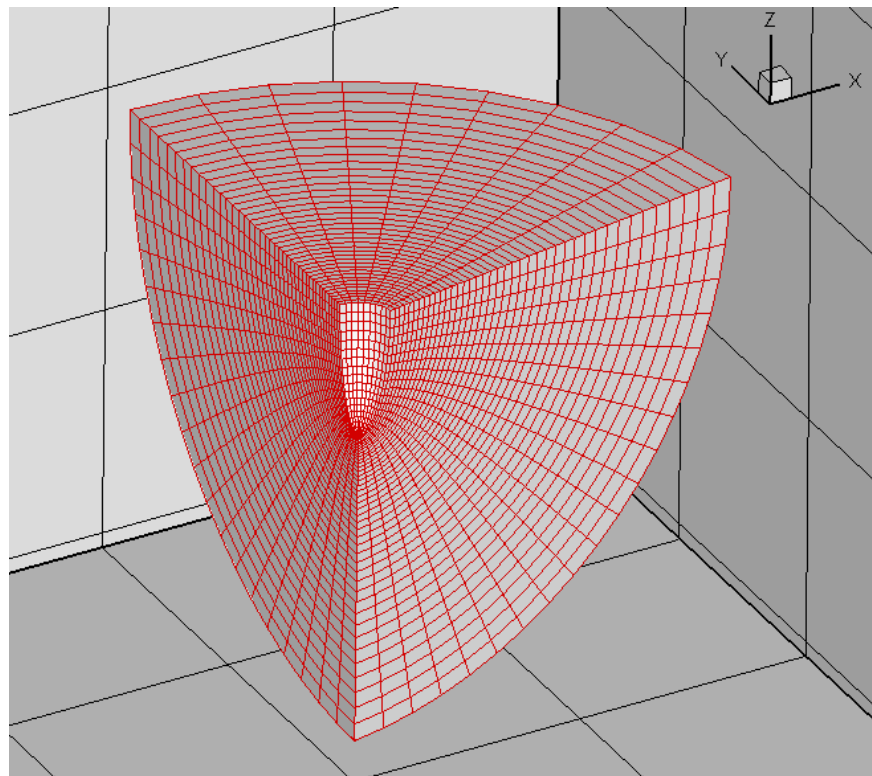


Figure 5.9: Different Aspect of Grid Domain in Prolate Spheroidal Coordinates

The inner sphere surface which has a uniform temperature at 15°C is represented with blue color and the outer sphere surface which has a uniform temperature at 100°C is represented with red color. Temperature distribution between two sphere shells is shown in Figure (5.5). Symmetrical temperature distribution can be monitored via legend.

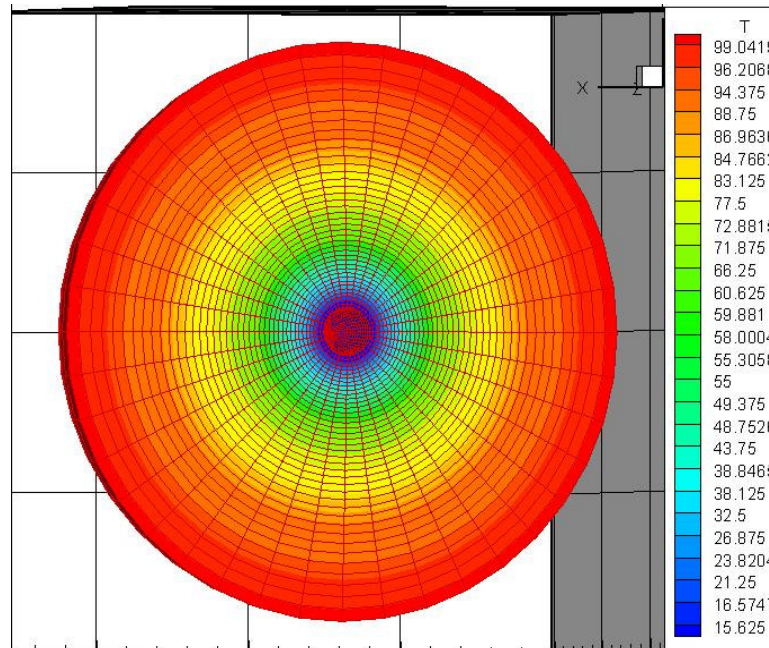


Figure 5.10: Half View of the Results with Grid in Prolate Spheroidal Coordinates

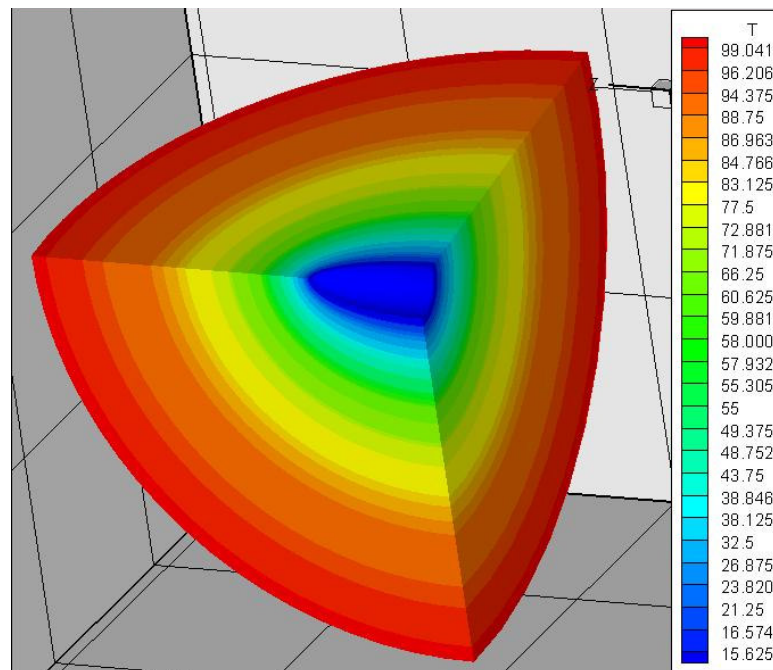


Figure 5.11: Another view of the results without Grid in Prolate Spheroidal Coordinates

Another portion of the region which is shown in Figure (5.11). Homogeneous temperature distribution with values can be seen in this Figure.

5.3 Solution of 3-D Potential Flow in Spherical Polar Coordinates

In this section, same physical domain which was used in subsection 5.1 -heat conduction problem- is going to be used but, this time external flow problem is going to be investigated. The surface of the spherical body is considered to be immersed in a uniform flow which is infinite extent. The flow passes over the outside surface of the body and is unconfined.

First, velocity potential function around the body will be solved, then velocities and pressure coefficient values on the node points will be obtained respectively. However the value of the potential function around vicinity of the boundaries are not known either on the surface of the inner sphere and the outer sphere encompasses the entire domain. Therefore, boundary conditions gain more important role than before.

The 2-D model of the problem is illustrated in Figure (5.12). Outer body shown in Figure 5.12 is taken as sphere and it has been contemplated as control volume. Control volume explained in various sources. For example **White (1995)** define control volume as, control volume is an attentively selected finite region by the analyst regarding the features of the boundaries. Moreover, **Mironer (1976)** stated that control volume boundaries has to be open and they have to allow quantities even it could be scalar or vectorial like mass, momentum and energy to cross through.

Same as the heat conduction problem inner sphere is presumed as solid so there will not be any penetration into inner body.

The velocity component normal to the surface of the solid boundary should be taken as 0 (**Gören, 2007**). Therefore, normal derivative of the velocity potential according to Fig 5.12 – in other words inner boundary condition on the small sphere r direction - can be shown as;

$$\frac{\partial \psi}{\partial r} = V_r = 0 \quad (5.7)$$

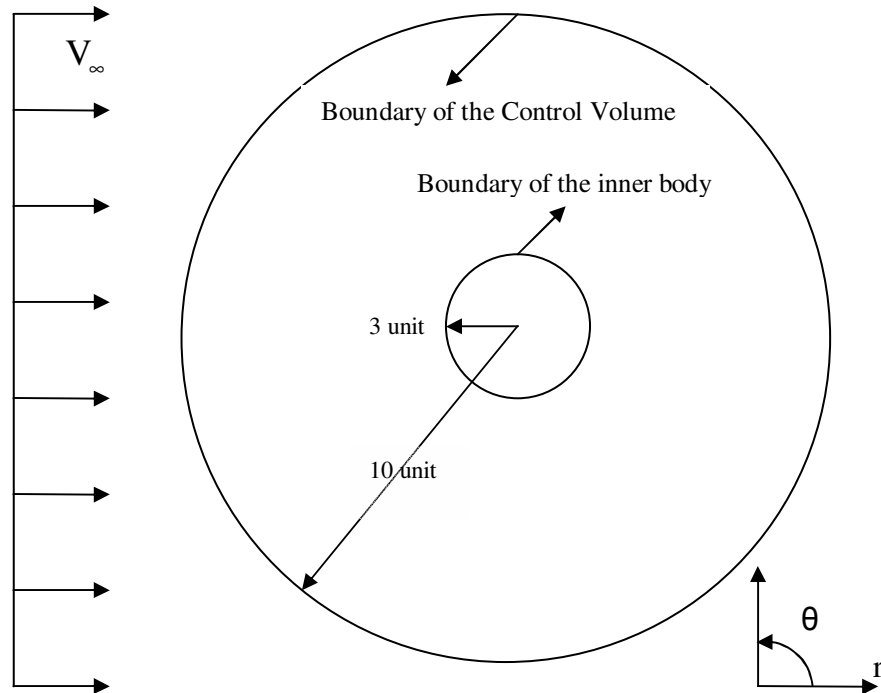


Figure 5.12: Schematic 2-D View of Subsection (5.3).

On contrary to subsections (5.1) and (5.2) boundary condition is now containing derivative of the potential function. **Blazek (2001)** stated that if specification of the boundary includes a derivatives of the dependent variables it is named as Neumann condition.

As mentioned in previous pages outer sphere taken as control volume and it is assumed that border and its close vicinity are enough far away in such manner the resultant velocity vectors on the outer sphere do not corrupted. Therefore, according to Fig (5.13) there will not be any velocity components in radial and angular directions. According to **Moon (1988)** the gradient of the velocity potential function in spherical coordinates is given below,

$$\text{grad}\psi = \frac{\partial\psi}{\partial r} + \frac{1}{r} \frac{\partial\psi}{\partial\theta} + \frac{1}{r \sin\theta} \frac{\partial\psi}{\partial\phi} \quad (5.8)$$

Radial velocity component on the outer sphere is;

$$V_r = \frac{\partial\psi}{\partial r} a_r \quad (5.9)$$

On the other hand radial component of the velocity can be expressed in terms of the uniform flow which was designated as V_∞ in Figure 5.12.

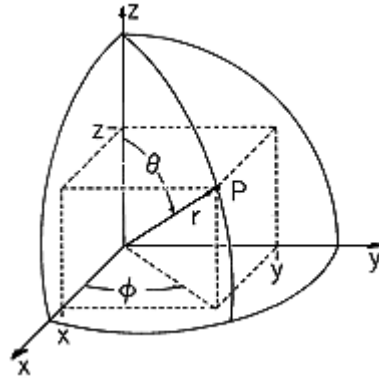


Figure 5.13: Quarter Portion of a Half Sphere (Moon, 1988, p.24)

Figure (5.13) is given to illustrate the vector transformations from Spherical Coordinates (r, θ, ϕ) to Cartesian Coordinates (x, y, z) . If uniform flow is given in z -direction, trigonometric relation between V_∞ and V_r can be expressed according to Figure (5.13) as follows;

$$V_r = -V_\infty \cos(\theta) \quad (5.10)$$

If Equations (5.9) and (5.10) equalize then;

$$\frac{\partial \psi}{\partial r} = -V_\infty \cos(\theta) \quad (5.11)$$

Equation (5.11) will be discretized with backward euler because absence of fictive nodes around domain. Therefore, outer nodes in domain form border of the problem.

$$\frac{\psi_N - \psi_{N-1}}{\Delta r} = -V_\infty \cos(\theta) \quad (5.12)$$

Eventually, outer boundary condition can be expressed as,

$$\psi_N = \psi_{N-1} - V_\infty \cos(\theta) \Delta r \quad (5.13)$$

Main iteration for the velocity potential around sphere is deduced in Section 2. Revert back and recall velocity potential in the spherical polar coordinates.

$$\nabla^2 \psi = \frac{\partial^2 \psi}{\partial r^2} + \frac{2}{r} \frac{\partial \psi}{\partial r} + \frac{1}{r^2} \frac{\partial^2 \psi}{\partial \theta^2} + \frac{\text{Cot}(\theta)}{r^2} \frac{\partial \psi}{\partial \theta} + \frac{1}{r^2 \text{Sin}^2 \theta} \frac{\partial^2 \psi}{\partial \phi^2} = 0 \quad (5.14)$$

Trigonometric term in equation (5.14) denominator causes a problem in the numerical calculations and therefore it should be eliminated from the equation. Because it will lead to singularity when $\theta = 0$ in the discretized form. Hence multiplying both sides of equation (5.14) by $r^2 \sin^2(\theta)$;

$$r^2 \text{Sin}^2 \theta \frac{\partial^2 \psi}{\partial r^2} + 2r \text{Sin}^2 \theta \frac{\partial \psi}{\partial r} + \text{Sin}^2 \theta \frac{\partial^2 \psi}{\partial \theta^2} + \text{Sin} \theta \text{Cos} \theta \frac{\partial \psi}{\partial \theta} + \frac{\partial^2 \psi}{\partial \phi^2} = 0 \quad (5.15)$$

If first order central difference approximation applied to Equation (5.15),

$$\begin{aligned} \nabla^2 \psi = & r_{i,j,k}^2 \text{Sin}^2 \theta_{i,j,k} \left[\frac{\psi_{i+1,j,k} - 2\psi_{i,j,k} + \psi_{i-1,j,k}}{\Delta r_{i,j,k}^2} \right] + 2r_{i,j,k} \text{Sin}^2 \theta_{i,j,k} \left[\frac{\psi_{i+1,j,k} - \psi_{i-1,j,k}}{2\Delta r_{i,j,k}} \right] \\ & + \text{Sin}^2 \theta_{i,j,k} \left[\frac{\psi_{i,j+1,k} - 2\psi_{i,j,k} + \psi_{i,j-1,k}}{\Delta \theta_{i,j,k}^2} \right] + \text{Sin} \theta_{i,j,k} \text{Cos} \theta_{i,j,k} \left[\frac{\psi_{i,j+1,k} - \psi_{i,j-1,k}}{2\Delta \theta_{i,j,k}} \right] \\ & + \left[\frac{\psi_{i,j,k+1} - 2\psi_{i,j,k} + \psi_{i,j,k-1}}{\Delta \phi^2} \right] = 0 \end{aligned} \quad (5.16)$$

If Gauss-Seidel iteration schema with same notation and coefficients, which was used in section 2.1 is applied for the velocity potential which is opened in spherical coordinate system, Equation (5.16) takes the form,

$$\begin{aligned} \psi_{i,j,k}^{m+1} = & \frac{-1}{\text{GSP}} \left[\text{GSW} \cdot \psi_{i-1,j,k}^{m+1} + \text{GSE} \cdot \psi_{i+1,j,k}^m + \text{GSS} \cdot \psi_{i,j-1,k}^{m+1} \right. \\ & \left. + \text{GSN} \cdot \psi_{i,j+1,k}^m + \text{GSL} \cdot \psi_{i,j,k-1}^{m+1} + \text{GSU} \cdot \psi_{i,j,k+1}^m \right] = 0 \end{aligned} \quad (5.17)$$

Open forms of the coefficients GSW, GSE, GSN, GSS, GSU, GSL and GSP have already been given in Chapter (2).

Fortran code has been developed to execute the iteration cycle of Equation (5.17). Algorithm of the problem for the potential flow case is depicted in Figure (5.14). The code generates the 3-D grid in desired type and calculates velocity potential values for all nodes within the desired volume. Then, gives graph of the velocity vectors and pressure coefficient distribution around sphere.

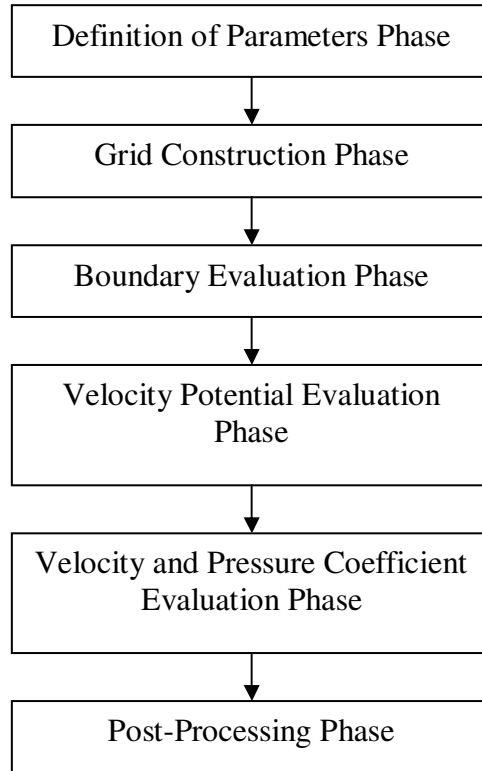


Figure 5.14: Algorithm for Potential Flow Problems

Grid algorithm which is used in potential flow around sphere problem is the same as the heat conduction problem around sphere body so there is no need to mention and present any view of the domain. If $41 \times 41 \times 41$ nodes used for the domain; velocity potential lines and contour representation are shown in Figure (5.15) and Figure (5.16). Figure (5.15) illustrates 2 dimensional cross-sectional view of the domain.

Regions shown in red color represents high potential values while regions having lower potential values are represented in blue colour. Moreover, velocity potential function gradually decreases while advancing to the outlet of the flow. The expected colour distribution is seen obviously via legend. Another view of the domain is given in Figure (5.16). That figure illustrates 3 dimensional view of the $1/8^{\text{th}}$ portion. Same slope of the velocity potential lines and symmetrical distribution in 3 dimensions is clearly seen in Figure (5.16).

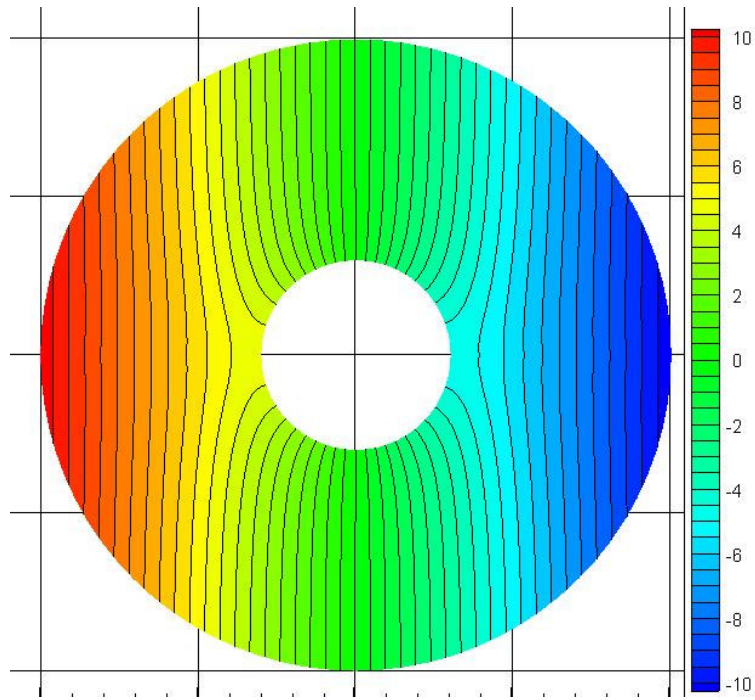


Figure 5.15: 2-D Presentation of Velocity Potential.

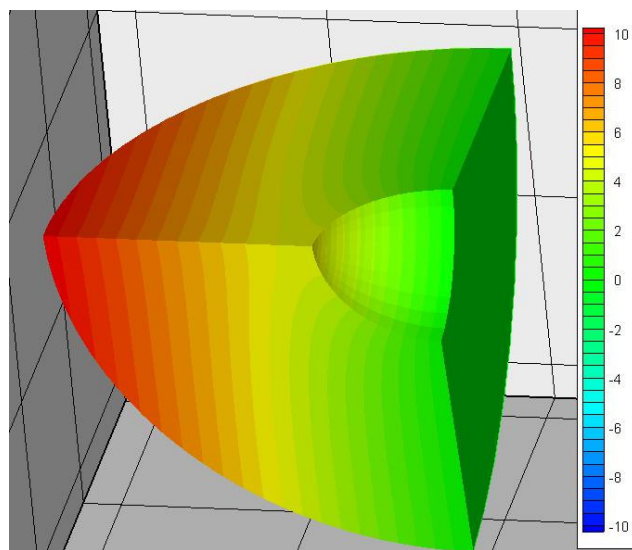


Figure 5.16: 3-D Presentation of Velocity Potential.

In order to determine the velocity components in spherical coordinate system, revert back to the gradient of the velocity potential function (ψ) which is given in Equation (5.8).

$$\nabla\psi = \frac{\partial\psi}{\partial r} + \frac{1}{r} \frac{\partial\psi}{\partial\theta} + \frac{1}{r \sin\theta} \frac{\partial\psi}{\partial\phi} \quad (5.18)$$

If Equation (5.18) is separated into velocity components, we obtain ;

$$V_r = \frac{\partial \psi}{\partial r} \quad (5.19)$$

$$V_\theta = \frac{1}{r} \frac{\partial \psi}{\partial \theta} \quad (5.20)$$

$$V_\phi = \frac{1}{r \sin \theta} \frac{\partial \psi}{\partial \phi} \quad (5.21)$$

If discretization with first order central differencing is applied to equations (5.19) (5.20) and (5.21) velocity components can be shown as;

$$V_r = \left(\frac{\Psi_{i+1,j,k} - \Psi_{i-1,j,k}}{2\Delta r} \right) \quad (5.18)$$

$$V_\theta = \frac{1}{r} \left(\frac{\Psi_{i,j+1,k} - \Psi_{i,j-1,k}}{2\Delta \theta} \right) \quad (5.19)$$

$$V_\phi = \frac{1}{r \sin \theta} \left(\frac{\Psi_{i,j,k+1} - \Psi_{i,j,k-1}}{2\Delta \phi} \right) \quad (5.20)$$

As mentioned before, for the postprocessing Tecplot program will be used. For the meaningful assessment of the for velocity vectors results, velocity vectors have to be expressed in cartesian coordinates. Therefore, Fortran velocity output datas have to be given in cartesian coordinates.

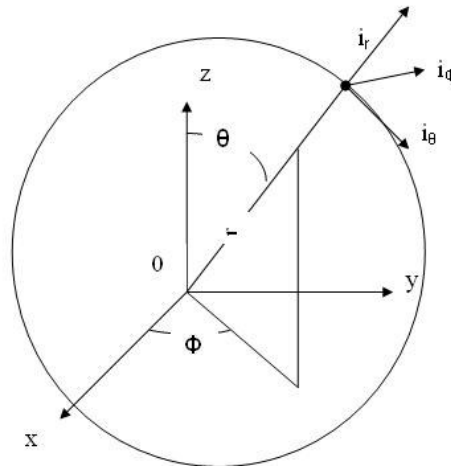


Figure 5.17: Transformation from Spherical Coordinates to Cartesian Coordinates.

Vectors in spherical coordinates is illustrated in Figure (5.17). Conversion in r-direction in spherical coordinates to x-direction in cartesian coordinates is given specifically in Figure (5.18).

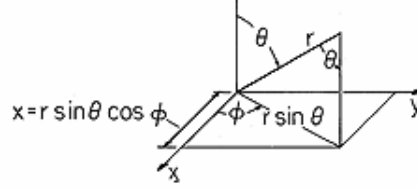


Figure 5.18: Transformation for r-direction (Thomas, 1998, p.844)

If same conversion is applied for other variables y and z, below mentioned equations are obtained,

$$y = r \sin \theta \sin \phi \quad (5.21)$$

$$z = r \cos \theta \quad (5.22)$$

Transformation for r-component briefly summarized above, but vector transformations can be done only after by resolving each of unit vectors i_r , i_θ , i_ϕ in terms of unit vectors in cartesian coordinates. Exact formulas regarding to transformation can be given as;

$$i_x = \sin \theta \cos \phi i_r + \cos \theta \cos \phi i_\theta + \sin \phi i_\phi \quad (5.23a)$$

$$i_y = \sin \theta \sin \phi i_r + \cos \theta \sin \phi i_\theta + \cos \phi i_\phi \quad (5.23b)$$

$$i_z = \cos \theta i_r - \sin \theta i_\theta \quad (5.23c)$$

Within the path of obtained vectorial transformation formulas (Equations 5.23a to 5.23c) let's apply them to discretized velocity components in spherical coordinates which were given in equations (5.18) to (5.20).

$$\begin{aligned} V_x = \sin \theta \cos \phi \left(\frac{\Psi_{i+1,j,k} - \Psi_{i-1,j,k}}{2\Delta r} \right) + \cos \theta \cos \phi \frac{1}{r} \left(\frac{\Psi_{i,j+1,k} - \Psi_{i,j-1,k}}{2\Delta \theta} \right) \\ + \sin \phi \frac{1}{r \sin \theta} \left(\frac{\Psi_{i,j,k+1} - \Psi_{i,j,k-1}}{2\Delta \phi} \right) \end{aligned} \quad (5.24)$$

$$\begin{aligned} V_y = \sin \theta \sin \phi \left(\frac{\Psi_{i+1,j,k} - \Psi_{i-1,j,k}}{2\Delta r} \right) + \cos \theta \sin \phi \frac{1}{r} \left(\frac{\Psi_{i,j+1,k} - \Psi_{i,j-1,k}}{2\Delta \theta} \right) \\ + \cos \phi \frac{1}{r \sin \theta} \left(\frac{\Psi_{i,j,k+1} - \Psi_{i,j,k-1}}{2\Delta \phi} \right) \end{aligned} \quad (5.25)$$

$$V_z = \cos \theta \left(\frac{\Psi_{i+1,j,k} - \Psi_{i-1,j,k}}{2\Delta r} \right) - \sin \theta \frac{1}{r} \left(\frac{\Psi_{i,j+1,k} - \Psi_{i,j-1,k}}{2\Delta \theta} \right) \quad (5.26)$$

Obtained equations will be used the for vectoral representation of the velocity components. Figure (5.19) illustrates the 2-D cross-sectional slice of the domain.

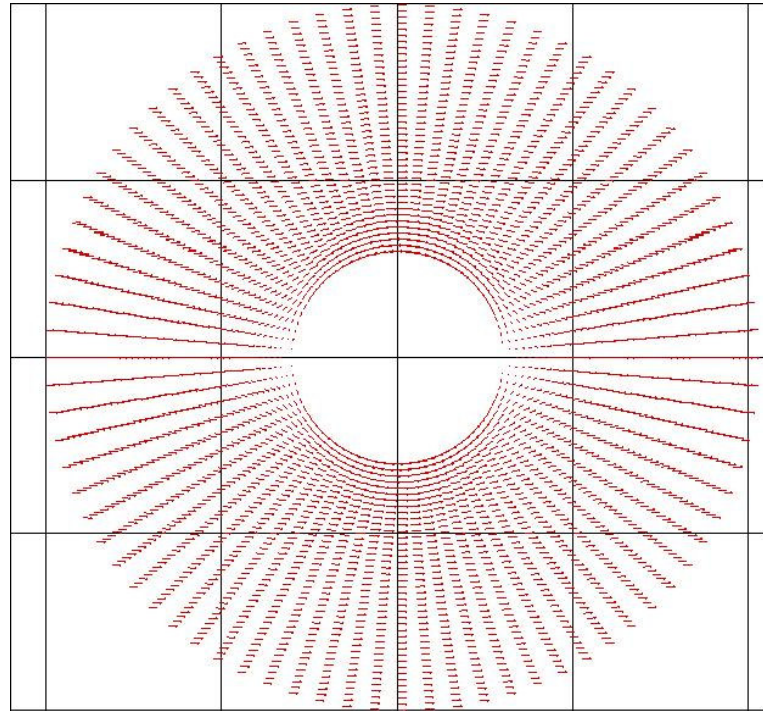


Figure 5.19: Velocity Distribution in the Domain

Figure (5.19) prove that selection of control volume and application of outer boundary condition is perfectly provided. Because the directions and magnitudes of the vectors on the outer sphere are same.

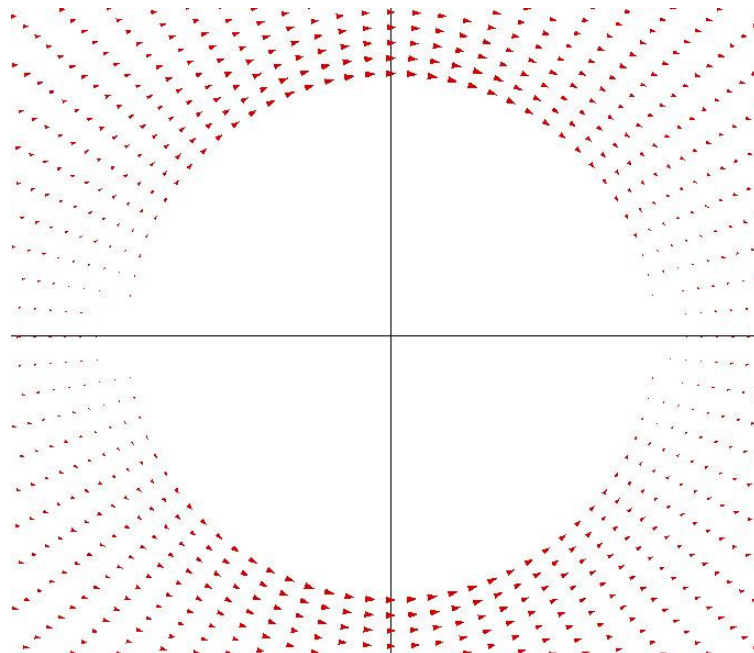


Figure 5.20: Another View of Velocity distribution

Closer view of the inner body is shown in Figure (5.20). In this Figure, velocity vectors is represented with arrow heads to obtain better view. Shown velocity vectors in Figure (5.20) prove that there is no penetration into the innerbody and parallel flow to the surface condition is provided. Therefore, compliance of the algorithm for inner boundary condition is guaranteed.

For the contoural representation resultant velocities have to be calculated. Resultant velocity can be obtained by Equation (5.27),

$$|V| = \sqrt{V_x^2 + V_y^2 + V_z^2} \quad (5.27)$$

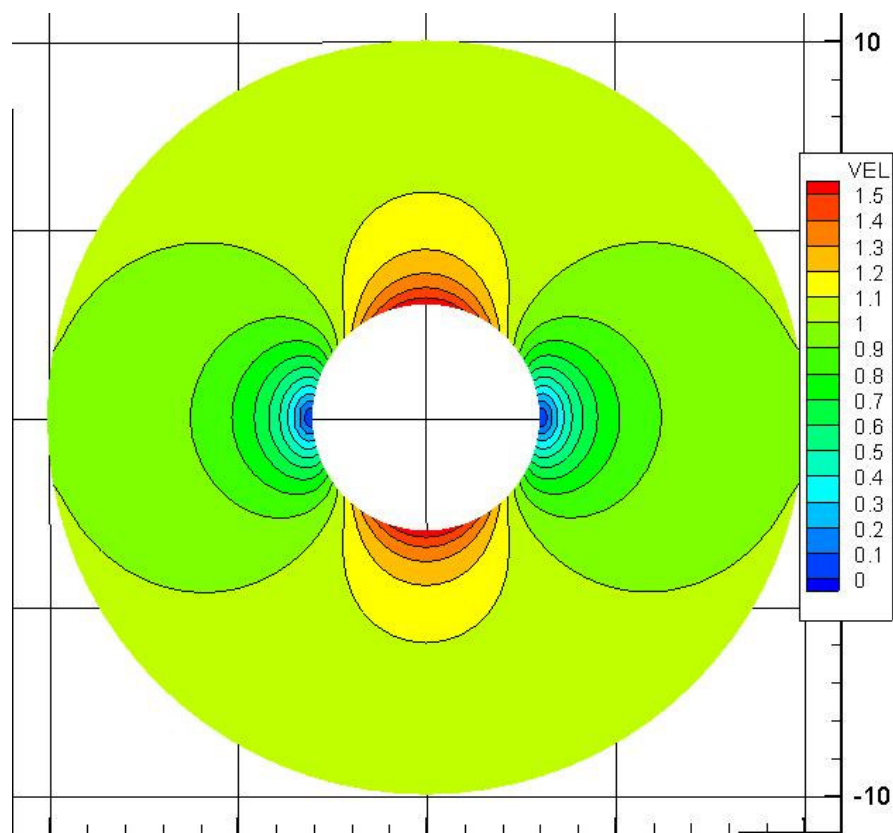


Figure 5.21: Velocity Distribution Contours Around a Sphere.

Velocity distribution between two sphere shells is shown in Figure (5.21). Red colour represents the speedy flows and the blue colour represents stagnation points. Symmetrical velocity distribution can be monitored via legend. Legend represents proportional velocities inside the domain ($\frac{V_{node}}{V_{\infty}}$).

After obtain resultant velocities around sphere now it is easy to find Pressure Coefficient distribution around sphere. The nondimensional Pressure coefficient (also known as the Euler number) is defined as,

$$C_p = \frac{p - p_\infty}{\frac{1}{2} \rho V_\infty^2} \quad (5.28)$$

The Bernoulli equation for steady flow is;

$$p_1 + \frac{1}{2} \rho v_1^2 = p_\infty + \frac{1}{2} \rho V_\infty^2 \quad (5.29)$$

Inserting the Bernoulli equation into Equation (5.28), this definition results in,

$$C_p = 1 - \frac{v_1^2}{V_\infty^2} \quad (5.30)$$

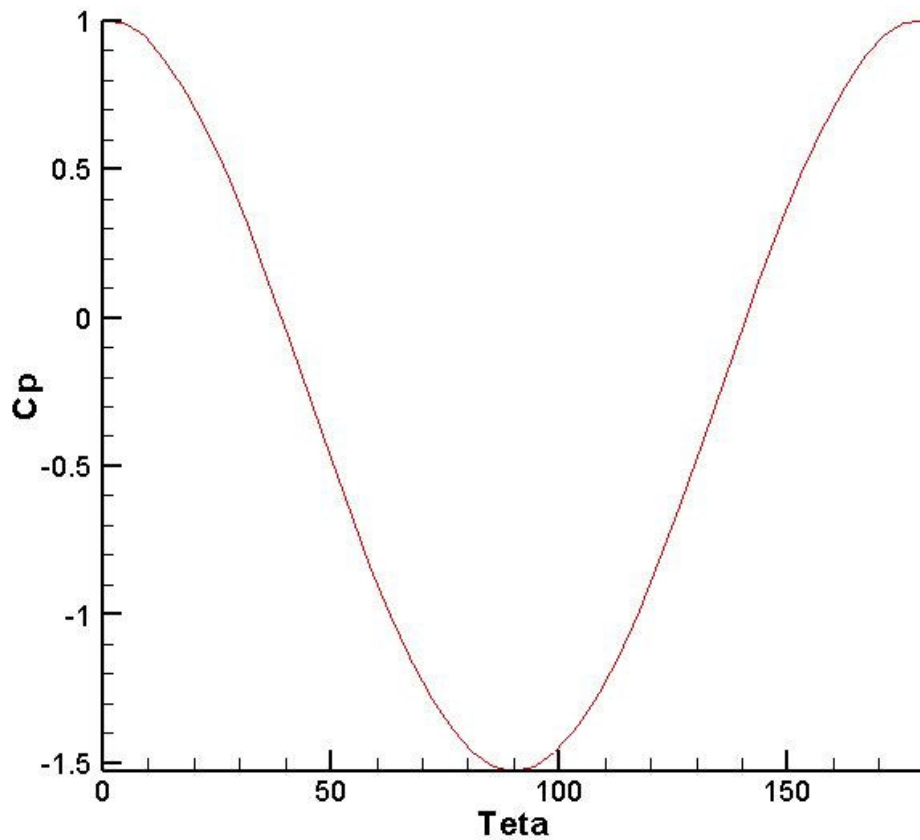


Figure 5.22: Pressure Coefficient Around a Sphere

Figure (5.22) graph shows pressure coefficient distribution around sphere body. As it seen from the graph, entrance and end point of the sphere is equal to 1 and it means there are two stagnation points while proceeding on the surface of the iner body. According to the graph maximum velocity is observed on 90°. Moreover, symmetrical pressure coefficient distribution according to 90° axis is clearly seen on Figure (5.22). It is the proof of the right working algorithm. Verification of the graph is going to be done in section 6.

5.4 Solution of 3-D Potential Flow in Prolate Spheroidal Coordinates

Now the last case of the problem will be intruded. In this subsection, same physical space which was used in heat conduction problem around prolate body – Subsection (5.2)- is going to be used but, this time external flow evaluation will be investigated. Prolate spheroidal body is again considered to be immersed in a uniform flow which is infinite extent. The flow passes over the outside surface of the body and is unconfined.

In this example again boundaries of the problem are not steady, therefore Neumann Boundary Condition will be used. Same as the sphere flow problem -Subsection (5.3)- inner sphere is presumed as solid. Therefore there will not be any penetration into inner body. The outer body is taken as sphere and it has been contemplated as control volume. Equation (5.7) and (5.10) will be implemented as boundary conditions.

Main iteration for the velocity potential around sphere is deduced in Section 3. Revert back and recall discretized velocity potential in prolate spheroidal coordinates,

$$\begin{aligned}
 Z(\eta, \theta) \left[\text{Sin}(\theta) \left(\frac{\Psi_{i+1,j,k} - 2\Psi_{i,j,k} + \Psi_{i-1,j,k}}{(\Delta\eta)^2} \right) + \text{Sin}(\theta) \text{Coth}(\eta) \left(\frac{\Psi_{i+1,j,k} - \Psi_{i-1,j,k}}{2\Delta\eta} \right) \right. \\
 \left. \text{Sin}(\theta) \frac{\Psi_{i,j+1,k} - 2\Psi_{i,j,k} + \Psi_{i,j-1,k}}{(\Delta\theta)^2} + \text{Cos}(\theta) \frac{\Psi_{i,j+1,k} - \Psi_{i,j-1,k}}{2\Delta\theta} \right] \\
 + \text{Sin}(\theta) \frac{\Psi_{i,j,k+1} - 2\Psi_{i,j,k} + \Psi_{i,j,k-1}}{(\Delta\phi)^2} = 0 \quad (5.31)
 \end{aligned}$$

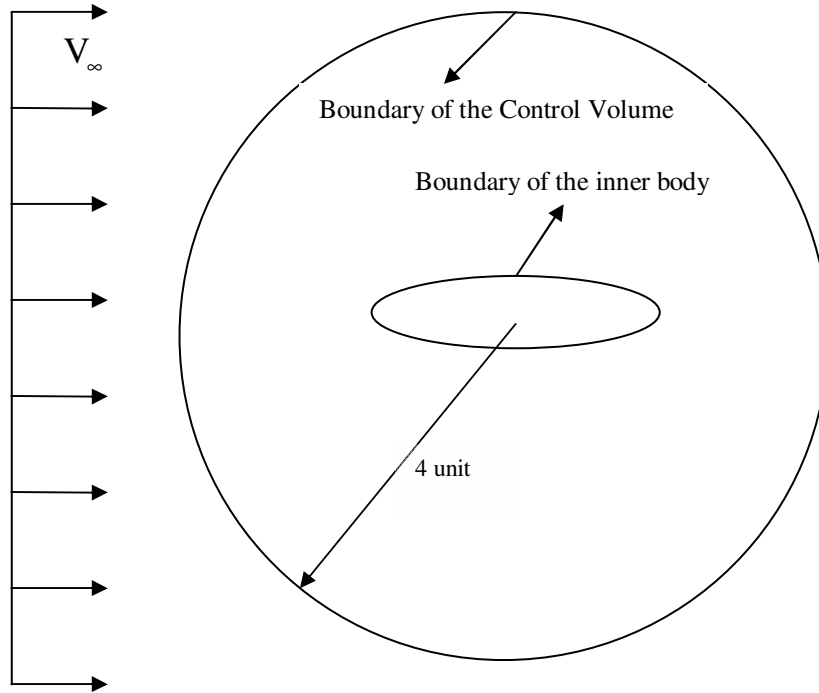


Figure 5.23: Schematic 2-D view of Subsection (5.4).

If Gauss-Seidel iteration schema with same notation and coefficients, which was used in section 3 is applied for the velocity potential which is opened in prolate spheroidal coordinate system, Equation (5.31) takes the form,

$$\psi_{i,j,k}^{m+1} = \frac{-1}{PP} \left[PW \cdot \psi_{i-1,j,k}^{m+1} + PE \cdot \psi_{i+1,j,k}^m + PS \cdot \psi_{i,j-1,k}^{m+1} + PN \cdot \psi_{i,j+1,k}^m + PL \cdot \psi_{i,j,k-1}^{m+1} + PU \cdot \psi_{i,j,k+1}^m \right] = 0 \quad (5.32)$$

Open forms of the coefficients PW, PE, PN, PS, PU, PL and PP have already been given in Chapter 3.

Fortran code has been developed to execute the iteration cycle of Equation (5.32). Algorithm of the problem for the potential flow around prolate spheroidal body case is depicted in Figure (5.14). The code generates the 3-D grid in desired type and calculates velocity potential values for all nodes within the desired volume. Then, gives graph of the velocity vectors and pressure coefficient distribution around prolate spheroidal body.

Grid algorithm which is used in potential flow around prolate spheroidal body is the same as the heat conduction problem for prolate body so there is no need to mention

and present any view of the domain. If 41x41x41 nodes used for the domain; velocity potential lines and contour representation are shown in Figure (5.24) and Figure (5.25). Figure (5.24) illustrates 2 dimensional cross-sectional view of the domain.

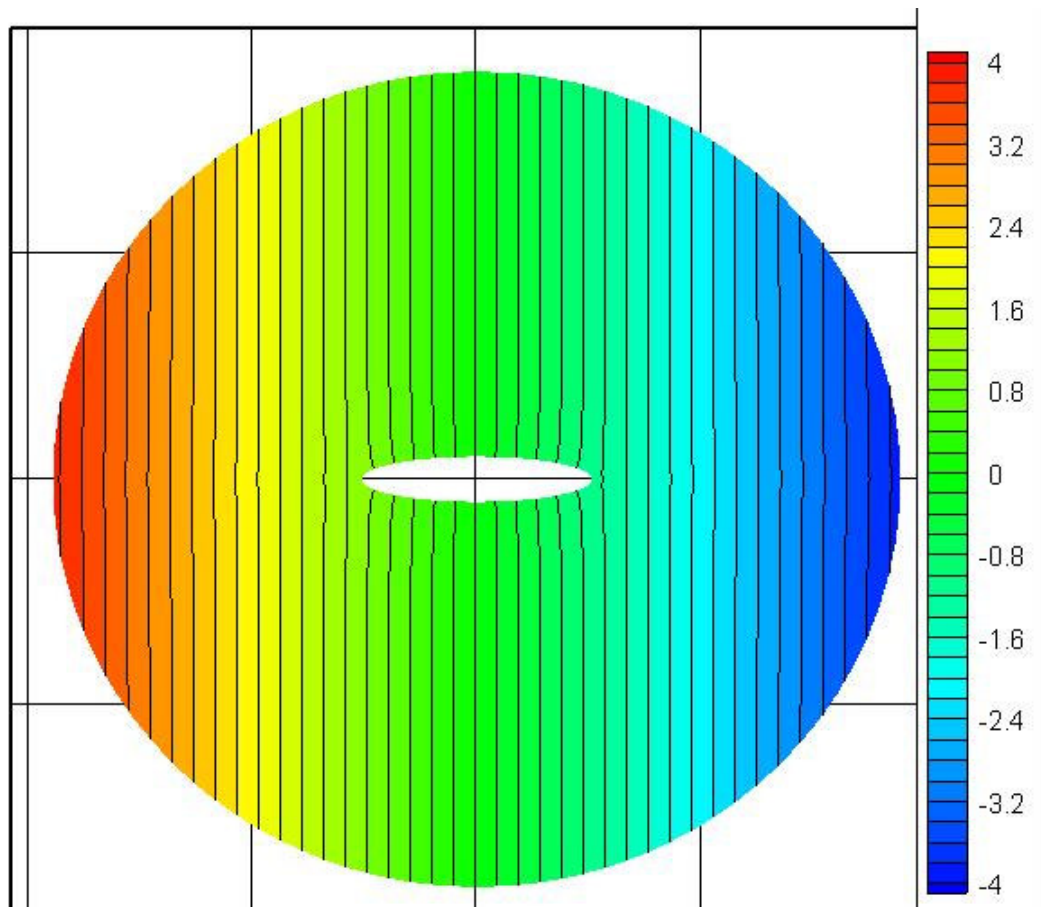


Figure 5.24: 2-D Presentation of Velocity Potential.

Regions shown in red color represents high potential values while regions having lower potential values are represented with blue colour. Moreover, velocity potential function gradually decreases while advancing to the outlet of the flow. The expected colour distribution is seen obviously via legend. Another view of the domain is given in Figure (5.25). That figure illustrates 3 dimensional view of the 1/8th portion. Symmetrical distribution in 3-D is clearly shown in Figure (5.16).

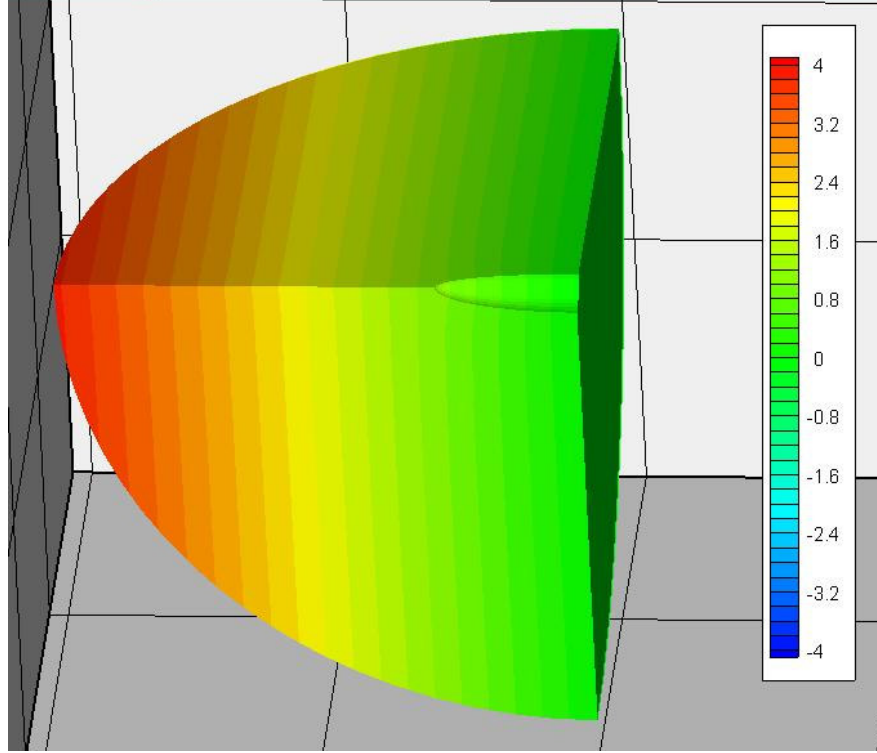


Figure 5.25: 3-D Presentation of Velocity Potential.

In order to determine the velocity components in prolate spheroidal coordinate system, gradient of the velocity potential function (ψ) has to be investigated, which is given in **Moon (1988)** as;

$$\text{grad}\psi = \frac{1}{a(\sinh^2 \eta + \sin^2 \theta)^{1/2}} \left[a_\eta \frac{\partial \psi}{\partial \eta} + a_\theta \frac{\partial \psi}{\partial \theta} \right] + \frac{a_\phi}{a \sinh \eta \sin \theta} \frac{\partial \psi}{\partial \phi} \quad (5.33)$$

If Equation (5.33) separated into velocity components, we obtain;

$$V_\eta = \frac{1}{a(\sinh^2 \eta + \sin^2 \theta)^{1/2}} \frac{\partial \psi}{\partial \eta} \quad (5.34)$$

$$V_\theta = \frac{1}{a(\sinh^2 \eta + \sin^2 \theta)^{1/2}} \frac{\partial \psi}{\partial \theta} \quad (5.35)$$

$$V_\phi = \frac{1}{a \sinh \eta \sin \theta} \frac{\partial \psi}{\partial \phi} \quad (5.36)$$

If Equations (5.34) (5.35) and (5.36) are discretized with first order central differencing approximation, velocity components will be obtained as,

$$V_{\eta} = \frac{1}{a(\sinh^2 \eta + \sin^2 \theta)^{1/2}} \left(\frac{\Psi_{i+1,j,k} - \Psi_{i-1,j,k}}{2\Delta\eta} \right) \quad (5.37)$$

$$V_{\theta} = \frac{1}{a(\sinh^2 \eta + \sin^2 \theta)^{1/2}} \left(\frac{\Psi_{i,j+1,k} - \Psi_{i,j-1,k}}{2\Delta\theta} \right) \quad (5.38)$$

$$V_{\phi} = \frac{1}{a \sinh \eta \sin \theta} \left(\frac{\Psi_{i,j,k+1} - \Psi_{i,j,k-1}}{2\Delta\phi} \right) \quad (5.39)$$

As mentioned before, for the postprocessing Tecplot program will be used. For the meaningful assessment of the for velocity vectors results, velocity vectors have to be expressed in cartesian coordinates. Therefore, Fortran velocity output datas have to be given in cartesian coordinates.

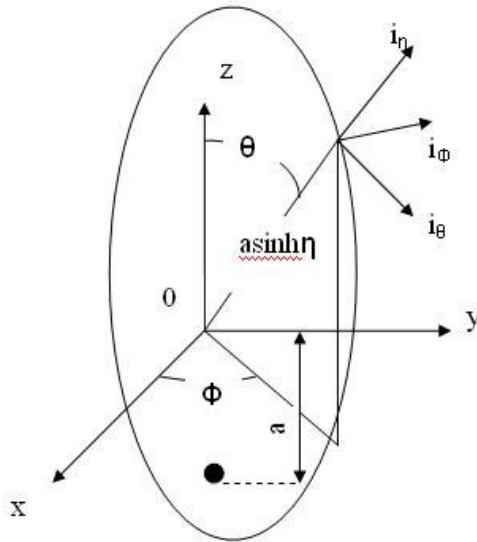


Figure 5.26: Transformation from Prolate Spheroidal Coordinates to Cartesian Coordinates.

Vectors in Prolate Spheroidal Coordinates is depicted in Figure (5.26). Conversion in η -direction in prolate spheroidal coordinates to x-direction in cartesian coordinates is given specifically in Figure (5.27). Attention should be paid to the fact that focus distance a is the multiplier of the variable in η -direction so it will be in every conversion step.

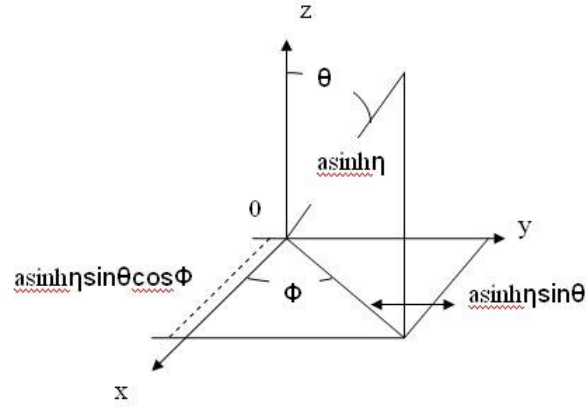


Figure 5.27: Transformation for η -Direction.

If same conversion is applied for other variables y and z , below mentioned equations are obtained,

$$y = a \sinh \eta \sin \theta \sin \phi \quad (5.40)$$

$$z = a \sinh \eta \cos \theta \quad (5.41)$$

Transformation for r -component briefly summarized above, but vector transformations can be done only after by resolving each of unit vectors i_η , i_θ , i_ϕ in terms of unit vectors in cartesian coordinates. Exact formulas regarding to transformation can be given as;

$$i_x = a \sinh \eta \sin \theta \cos \phi i_r + a \sinh \eta \cos \theta \cos \phi i_\theta + a \sinh \eta \sin \phi i_\phi \quad (5.42a)$$

$$i_y = a \sinh \eta \sin \theta \sin \phi i_r + a \sinh \eta \cos \theta \sin \phi i_\theta + a \sinh \eta \cos \phi i_\phi \quad (5.42b)$$

$$i_z = a \sinh \eta \cos \theta i_r - a \sinh \eta \sin \theta i_\theta \quad (5.42c)$$

within the path of obtained vectorial transformation formulas (Equation 5.42a to 5.42c) let's settle them to velocity components in cartesian coordinates. Focus distance a is simplified.

$$\begin{aligned} V_x = & \sinh \eta \sin \theta \cos \phi \frac{1}{(\sinh^2 \eta + \sin^2 \theta)^{1/2}} \left(\frac{\Psi_{i+1,j,k} - \Psi_{i-1,j,k}}{2\Delta r} \right) \\ & + \sinh \eta \cos \theta \cos \phi \frac{1}{(\sinh^2 \eta + \sin^2 \theta)^{1/2}} \left(\frac{\Psi_{i,j+1,k} - \Psi_{i,j-1,k}}{2\Delta \theta} \right) \end{aligned}$$

$$+ \sin \phi \frac{1}{\sin \theta} \left(\frac{\Psi_{i,j,k+1} - \Psi_{i,j,k-1}}{2\Delta\phi} \right) \quad (5.43)$$

$$\begin{aligned} V_y = & \sinh \eta \sin \theta \sin \phi \frac{1}{(\sinh^2 \eta + \sin^2 \theta)^{1/2}} \left(\frac{\Psi_{i+1,j,k} - \Psi_{i-1,j,k}}{2\Delta r} \right) \\ & + \sinh \eta \cos \theta \sin \phi \frac{1}{(\sinh^2 \eta + \sin^2 \theta)^{1/2}} \left(\frac{\Psi_{i,j+1,k} - \Psi_{i,j-1,k}}{2\Delta\theta} \right) \\ & + \cos \phi \frac{1}{\sin \theta} \left(\frac{\Psi_{i,j,k+1} - \Psi_{i,j,k-1}}{2\Delta\phi} \right) \end{aligned} \quad (5.44)$$

$$\begin{aligned} V_z = & \sinh \eta \cos \theta \frac{1}{(\sinh^2 \eta + \sin^2 \theta)^{1/2}} \left(\frac{\Psi_{i+1,j,k} - \Psi_{i-1,j,k}}{2\Delta r} \right) \\ & - \sinh \eta \sin \theta \frac{1}{(\sinh^2 \eta + \sin^2 \theta)^{1/2}} \left(\frac{\Psi_{i,j+1,k} - \Psi_{i,j-1,k}}{2\Delta\theta} \right) \end{aligned} \quad (5.45)$$

Obtained equations will be used for the vectorial representation of the velocity components. Figure (5.19) illustrates the 2-D cross-sectional slice of the domain.

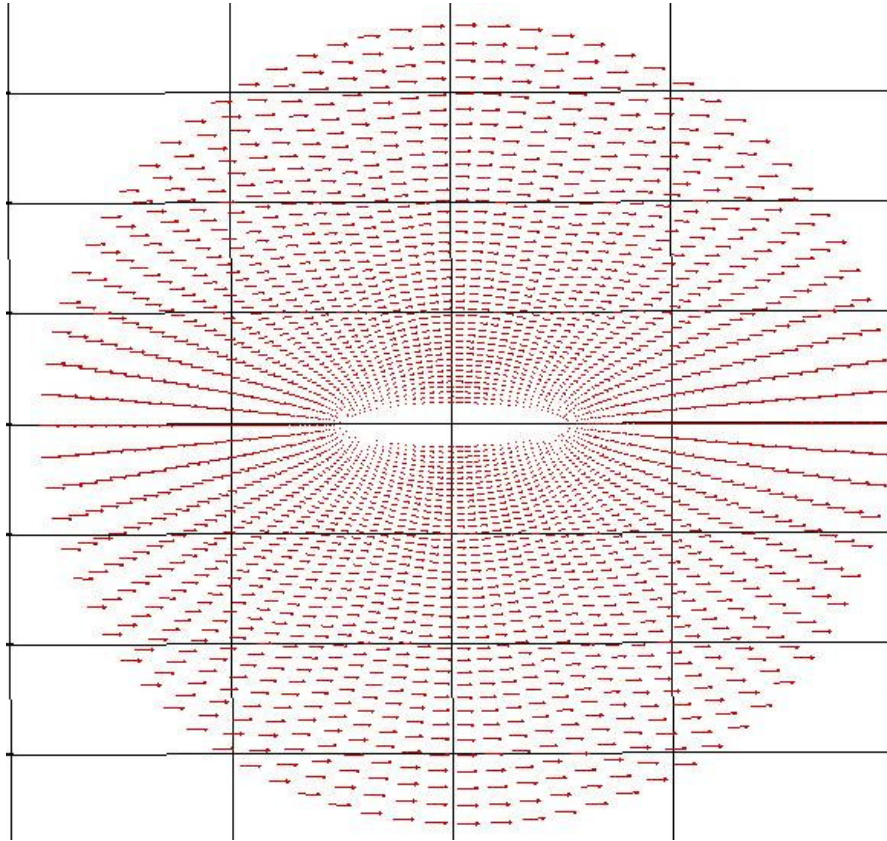


Figure 5.28: Velocity Distribution in the Domain

Figure (5.28) prove that selection of control volume and application of outer boundary condition is perfectly provided. Because the directions and magnitudes of the vectors on the outer sphere are same.

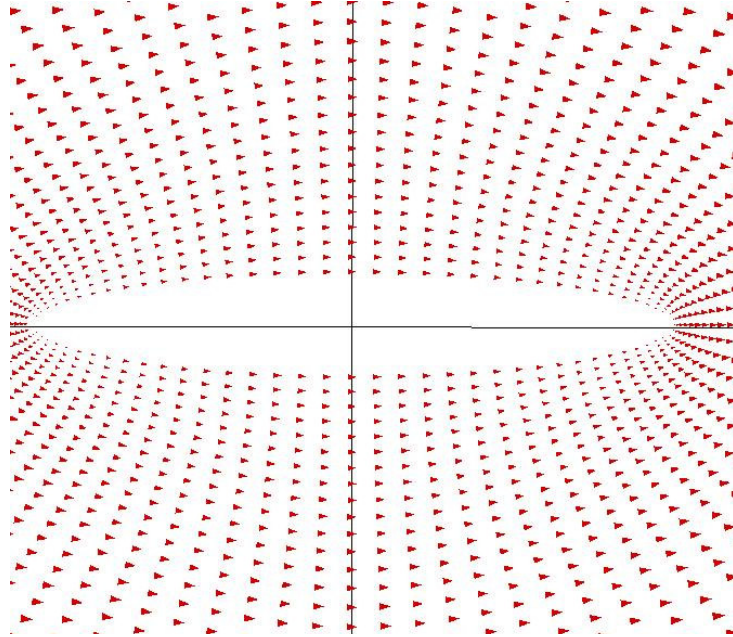


Figure 5.29: Another View of Velocity Distribution

Closer view of the inner body is shown in Figure (5.29). In this Figure, velocity vectors is represented with arrow heads to obtain better view. Shown velocity vectors in Figure (5.20) prove that there is no penetration into the innerbody and parallel flow to the surface condition is provided. Therefore, compliance of the algorithm for inner boundary condition is guaranteed.

For the contoural representation resultant velocities have to be calculated. Resultant velocity can be obtained by Equation (5.46),

$$|V| = \sqrt{V_x^2 + V_y^2 + V_z^2} \quad (5.46)$$

Velocity distribution between two sphere shells is shown in Figure (5.30). Red colour represents the speedy flows and the blue colour represents stagnation points. Symmetrical velocity distribution can be monitored via contours.

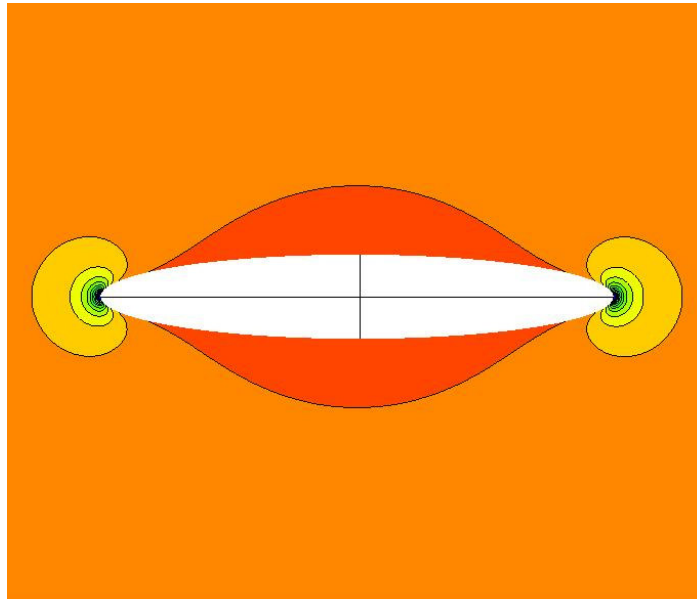


Figure 5.30: Velocity Distribution Contours Around a Prolate Spheroidal Body.

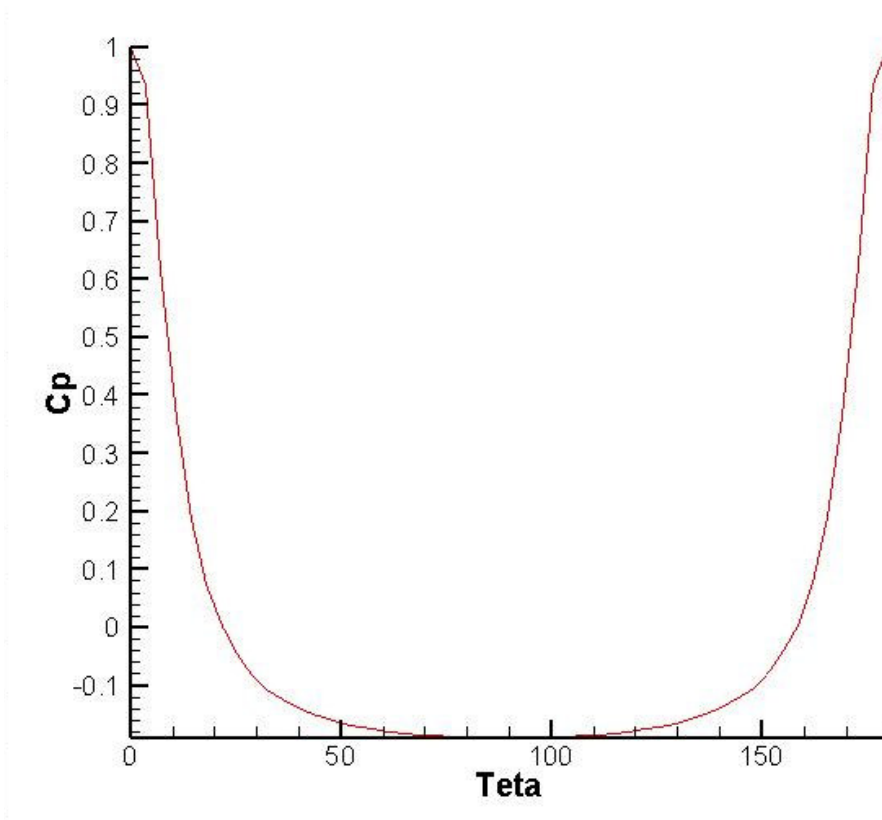


Figure 5.31: Pressure Coefficient Around a Prolate Spheroidal Body

Figure (5.31) graph shows pressure coefficient distribution around prolate spheroidal body. As it seen from the graph, entrance and end point of the sphere is equal to 1 and it means there are two stagnation points while proceeding on the surface of the iner body. According to the graph maximum velocity is observed on 90° . Moreover,

symmetrical pressure coefficient distribution according to 90° axis is clearly seen on Figure (5.22). It is the proof of the right working algorithm. Verification of the graph is going to be done in section 6.

6. COMPARISON OF RESULTS

Potential flow over a sphere is the well-known and popular example for the external flow problems and it's effortless to find analytic solution of velocity potential graph, velocity vectors and pressure distributions results even in the fundamental fluid mechanics books (**White 1995, Panton 1984, Owczarek 1968, etc.**) but it is hard to express the same for a prolate spheroidal shape. Therefore only pictural comparison for sphere domain is made with literature sources. Notwithstanding comparison of results between in house codes and two commercial codes Fluent, SymLab are presented in this section.

6.1 In House Code Versus Fluent and Symlab for a Sphere

In this subsection, analytic velocity potential result for the sphere body is compared with obtained results (in-house, Fluent and Symlab). Figure 6.1 illustrates combination of a uniform stream and a point doublet at the origin. It is taken from White (1995).

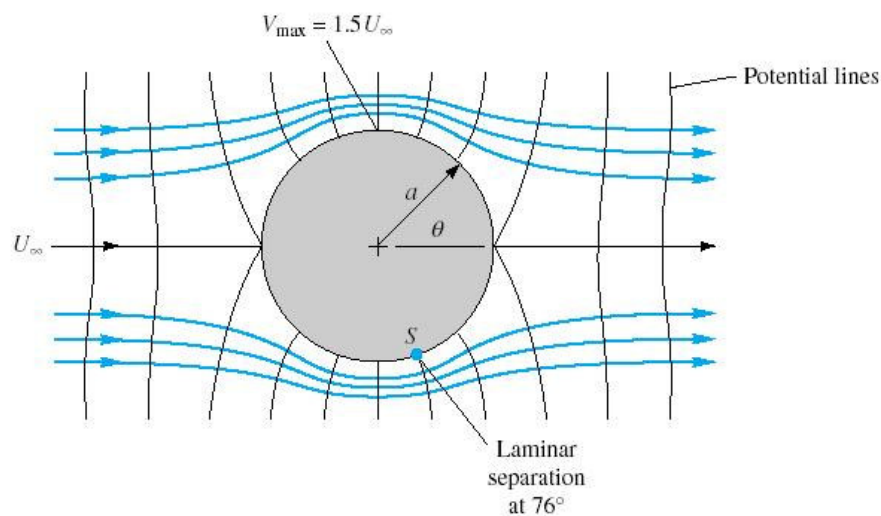


Figure 6.1: Streamlines and Potential Lines for Inviscid Flow Past a Sphere (White 1995. p.538)

In this figure, potential lines, streamlines, stagnation points and maximum velocity value and location point around the sphere is shown. There are two stagnation points one at the front (when θ equals to π) and the other at the rear (when θ equals 0) of the sphere. The maximum velocity occurs at the top (when θ equals to $\frac{\pi}{2}$) and at the bottom (when θ equals to $-\frac{\pi}{2}$) of the sphere. **White (1995)** state that velocity distribution on the surface of the sphere can be found with Equation (6.1).

$$V_s = \frac{3}{2} V_\infty \sin \theta \quad (6.1)$$

Additionally, seperation point is shown in Figure (6.1), but laminar-boundary layer theory is not involved in this thesis content. Therefore, the proof of the seperation point is not investigated. Further details about seperation point on the sphere can be found in White (1991).

Same geometry which is shown in Figure 5.12 is constructed in Fluent and Symlab programmes. Then the grid is generated and domain is solved with same boundary conditions. Various results which were obtained by using both Fluent and Symlab are given in Figure 6.2 to Figure 6.9.

In Figure (6.1) a closer view of velocity vectors around a sphere is presented. This figure is the output of the Fluent programme. Location of the stagnation points and proportional view of the vectors can be monitored within the figure.

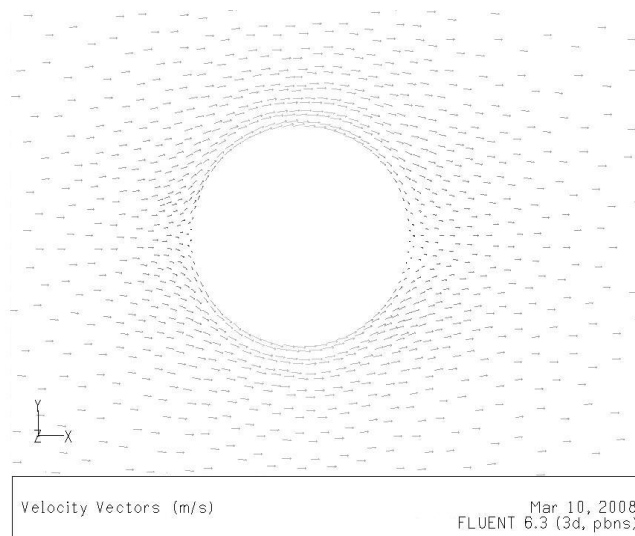


Figure 6.2: Vectorial Presentation of Velocity Results Around a Sphere

When comparison between in-house code vectorial result (Figure 5.21) and Fluent vectorial result (Figure 6.2) is executed, similar vectorial distribution around the sphere is seen. We see both in Figure 5.21 and Figure 6.2 that, velocity vanishes at the front and the rear ends, same stagnation locations are shown in the analytical result which is shown in Figure 6.1.

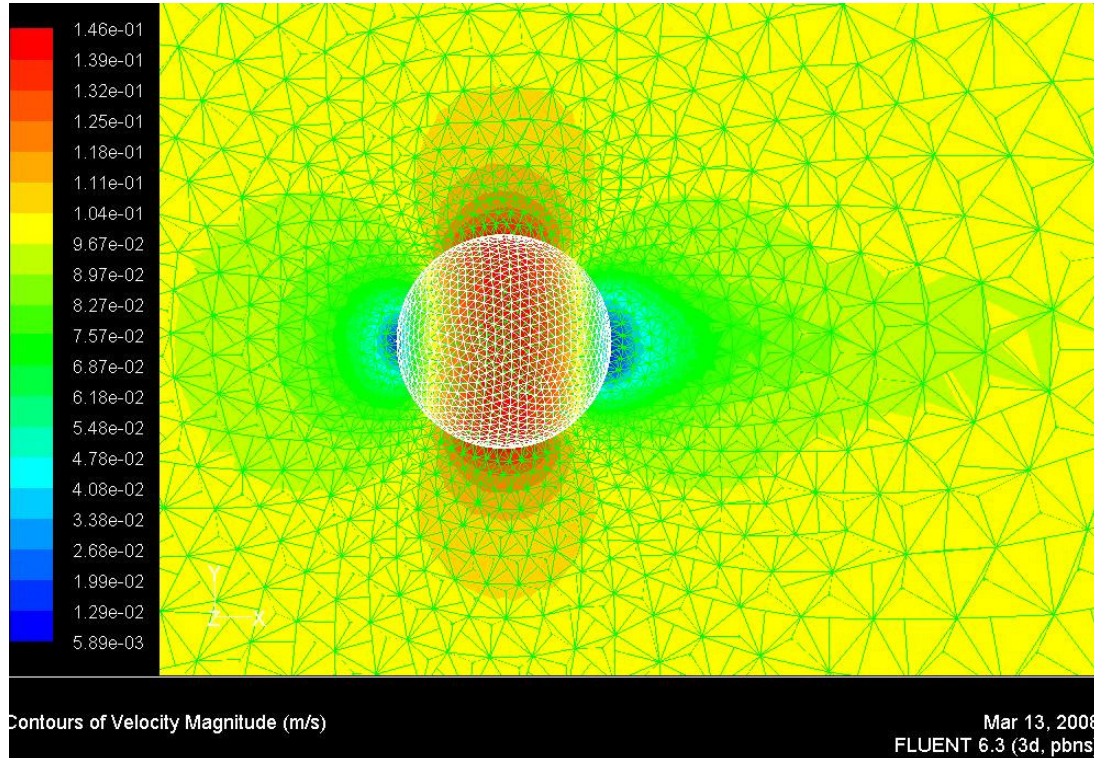


Figure 6.3: Contoural Presentation of Velocity Results Around a Sphere

Contoural velocity distribution inside the domain which is obtained with Fluent, is shown in Figure (6.3). Red colour represents the faster flow and the blue colour represents stagnation points. Variation of the velocity values on the sphere surface can be monitored via the legend.

Another comparison can be made for the contoural presentations of the results - between Figures 5.21 and 6.3, again consistent distributions are seen. Legends of these pictures show us;

- 1-) Maximum velocity is obtained when θ equals to $\frac{\pi}{2}$ and $-\frac{\pi}{2}$ radians.
- 2-) Maximum velocity value is approximately $1.5U_{\infty}$.
- 3-) Stagnation points are obtained when θ equals to 0 and π radians.
- 4-) Velocity values, when θ equals to 0 and π radians, are equal to 0.

5-) Symmetrical velocity distribution around sphere is obtained around the sphere.

Accordance with the analytical results is obviously seen through the above mentioned results. For the item 2, approximately term is used because, unfortunately precise $1.5U_{\infty}$ value could not be reached neither with Fluent nor with the in-house code. One of the Reasons of this problem is investigated in subsection 6.3. Other reasons summarized at the end of this subsection.

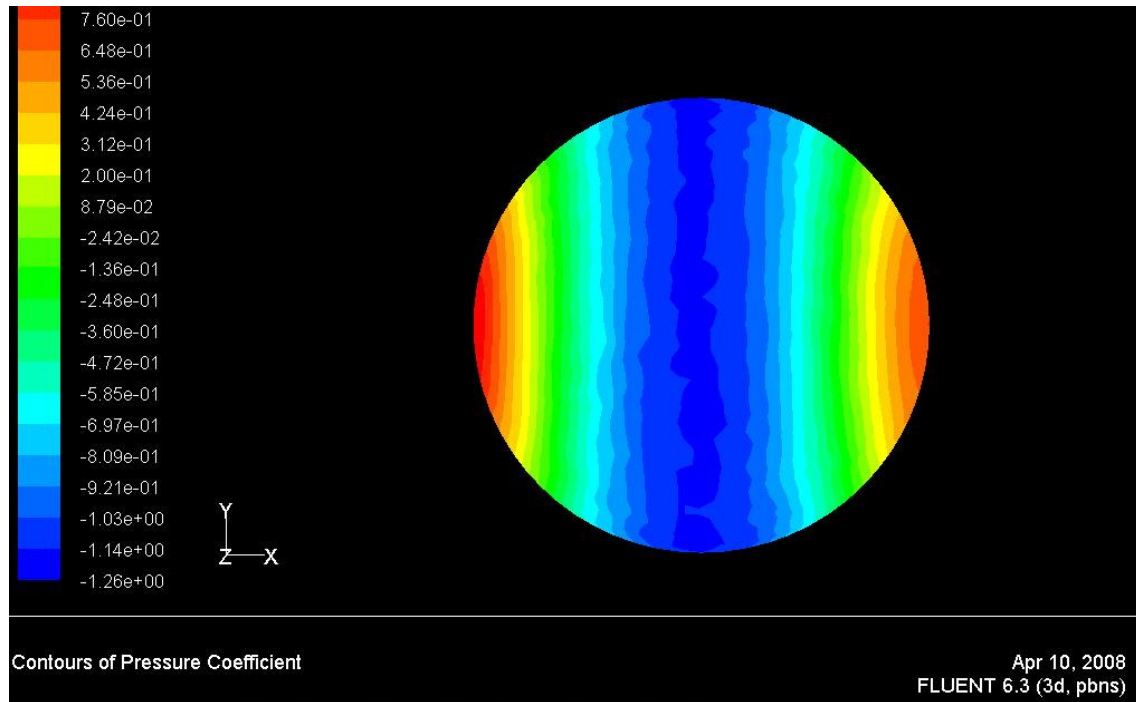


Figure 6.4: Fluent Pressure Coefficient Distribution Results Around a Sphere

Pressure Coefficient distribution results around the sphere which are both obtained with Fluent and Symlab, is shown in Figure (6.4) and Figure (6.5). Red colour represents the higher C_p values and the blue colour represents lower C_p values both in both Figures. Graphical results of these Figures and comparison of the C_p results on the sphere surface with different programmes and analytic results are given in page 69.

Surface velocity distribution along the sphere is given in Equation (6.1). Datas which are used in Analytic curve is given in Appendix A. In all the graphs X-axis states θ -angle except in Figure (6.6). Fluent curve X-axis denotes proportional location of the node point relative to center of the sphere. Because of the additional option theoretical datas are given with red circles in Figure (6.7) which ease the comparison. As you

see from the different graphs, the general slope of the C_p function is similar. Unfortunately, they have small differences.

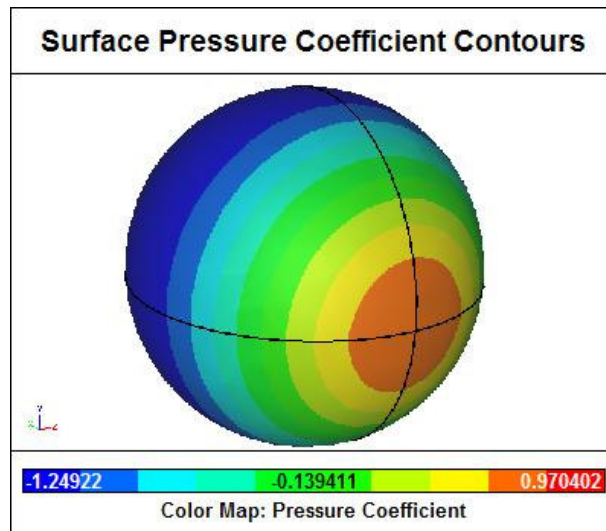


Figure 6.5: Symlab Pressure Coefficient Distribution Results Around a Sphere

Now, we have to mention another detail regarding to programmes' infrastructures to gain better understanding of the small differences which were encountered in the graphics. As known, partial differential equations can be solved either by discretizing the equation or by bringing it into a finite dimensional subspace. Different discretization methods can be given as,

- 1.) Finite Difference Method (FDM)
- 2.) Finite Volume Method (FVM)
- 3.) Boundary Element Method (BEM)
- 4.) Finite Element Method (FEM)

Programs that are used in this thesis use different discretization methodologies. For example Fluent, which is one of the best known CFD commercial code in the world, uses Finite Volume Method for analysis and Symlab uses Boundary Element Method for solving partial differential equations. It is a kind of panel code. On the other hand, in-house code uses Finite Difference Method. Nonetheless, convergence criteria, number of iteration steps, relaxation parameters, used grid type, number of nodes, etc. each affect the results. Therefore, it is very normal to see such minor discrepancies while using different algorithms even applied to the same geometry.

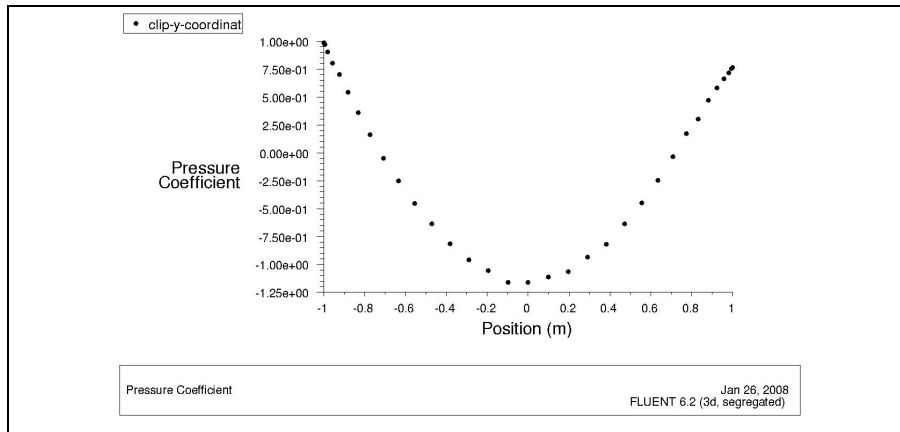


Figure 6.6: Fluent Graphical Pressure Coefficient Distribution Around a Sphere

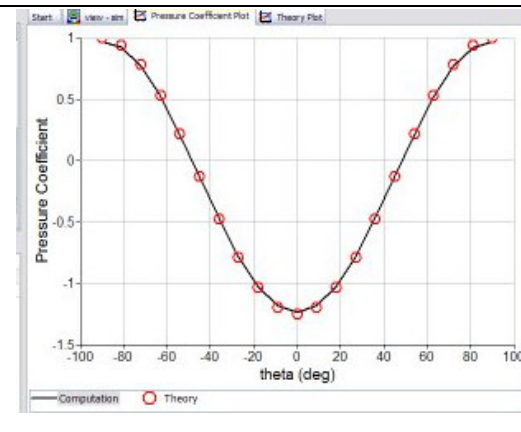


Figure 6.7: Symlab Graphical Pressure Coefficient Distribution Around a Sphere

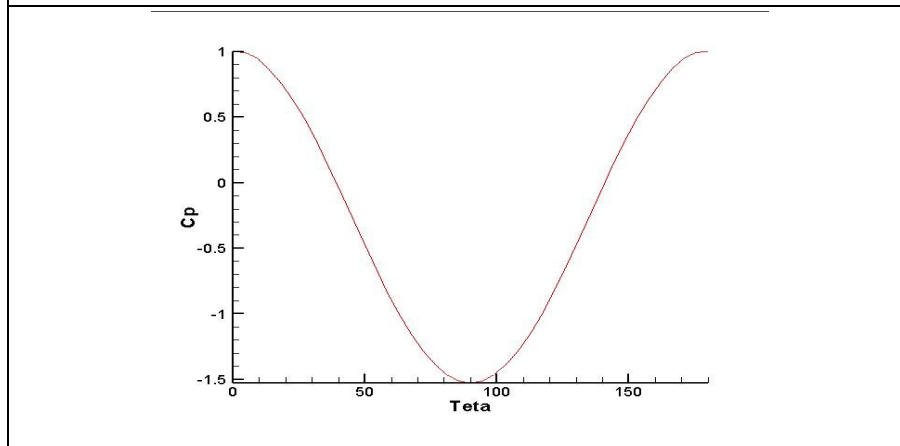


Figure 6.8: In-House Code Graphical Pressure Coefficient Distribution Around a Sphere

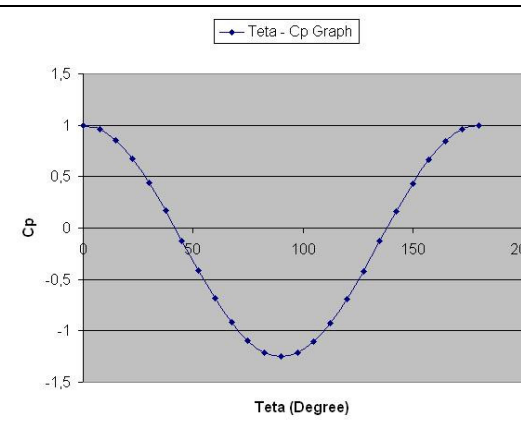


Figure 6.9: Theoretical Graphical Pressure Coefficient Distribution Around a Sphere

6.2 In House Code Versus Fluent and Symlab for Prolate Spheroidal Body

In this subsection, commercial codes spheroidal body results are compared with the results obtained in-section 5.

Same geometry which is shown in Figure 5.23 is constructed in Fluent and Symlab programmes. Then the grid is generated and the domain is solved with same boundary conditions. Various results which were obtained by both Fluent and Symlab are given in Figure 6.10 to Figure 6.16.

In Figure (6.10) a closer view of velocity vectors around a prolate spheroidal body is presented. This figure is the output of the Fluent programme. Location of the stagnation points and proportional view of the vectors can be monitored within the Figure.

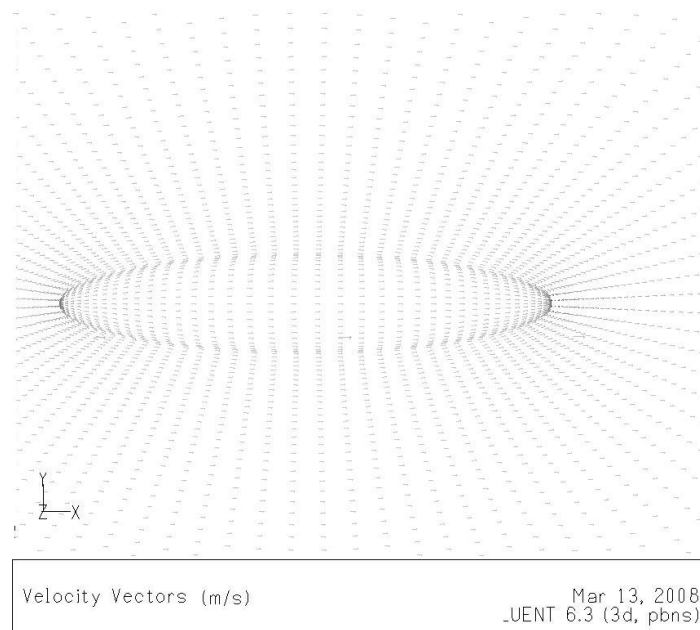


Figure 6.10: Vector Presentation of Velocity Results Around Prolate Spheroidal Body

When comparison between in-house code vectorial result (Figure 5.29) and Fluent vectorial result (Figure 6.10) is made, similar vectorial distribution around the Prolate spheroidal body is seen. We see both in Figure 5.29 and Figure 6.10 that velocity vanishes at the front and the rear ends.

Contoural velocity distribution around a prolate spheroidal body which is obtained by Fluent, is shown in Figure (6.11). Red colour represents the faster flow and the blue colour represents stagnation points. Variation of the velocity values on the surface can be monitored via legend.

Another comparison can be made for the contoural presentations of the results - between Figures 5.30 and 6.11, again consistent distributions are seen. Legends of these pictures show us;

- 1-) Maximum velocity is obtained when θ equals to $\frac{\pi}{2}$ and $-\frac{\pi}{2}$ radians.
- 2-) Maximum velocity value is approximately $1.1U_{\infty}$.
- 3-) Stagnation points obtained when θ equals to 0 and π radians.
- 4-) Velocity values, when θ equals to 0 and π radians, are equal to 0.
- 5-) Symmetrical velocity distribution is obtained around the body.

Accordance with the analytical results is obviously seen through the above mentioned results. For the item 2, approximately term is used because, unfortunately precise $1.1U_{\infty}$ value could not be reached neither by Fluent nor by the in-house

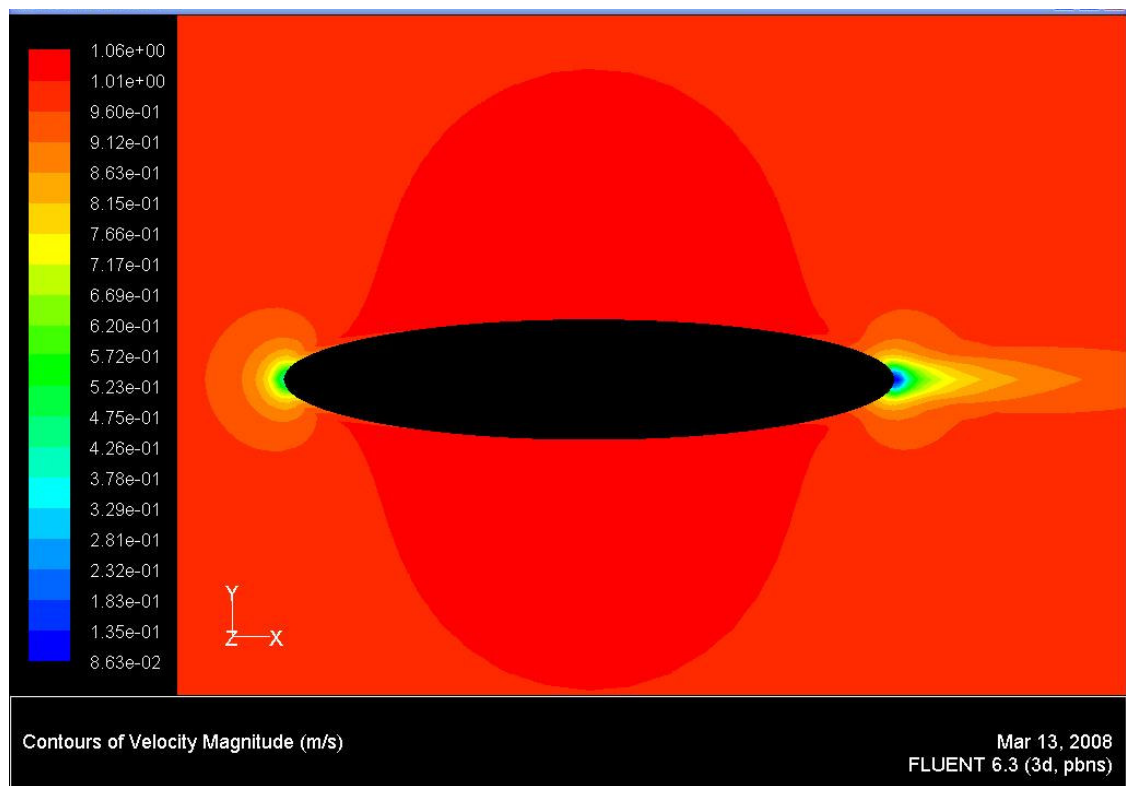


Figure 6.11: Contoural Representation of Velocity Results Around Prolate Spheroidal Body.

Pressure Coefficient distribution results around the sphere which are both obtained by Fluent and Symlab, are shown in Figure (6.4) and Figure (6.5). Red colour represents the higher C_p values and the blue colour represents lower C_p values in both Figures. Graphical results of these Figures and comparison of the C_p results on the prolate spheroidal surface with different programmes and analitic result are given in subsequent page.

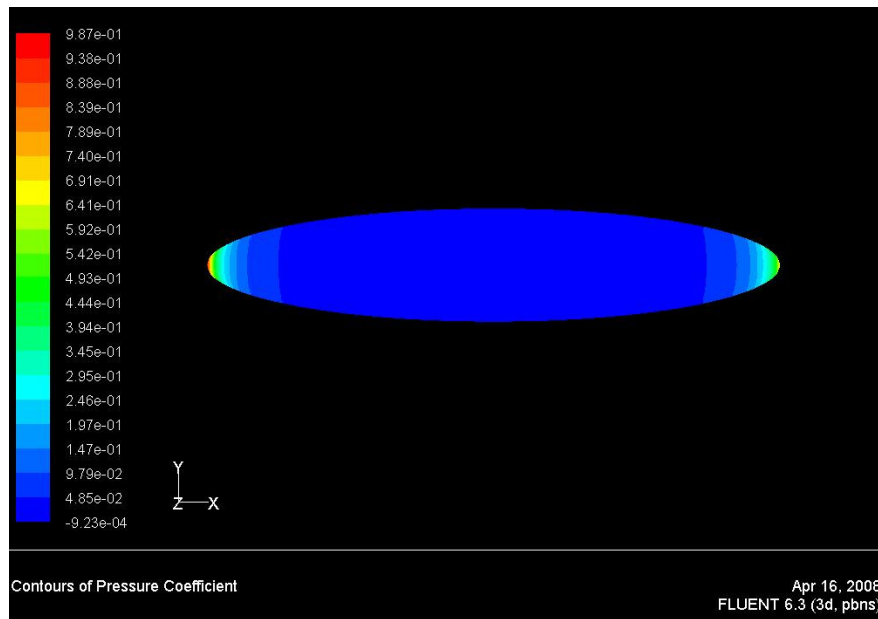


Figure 6.12: Fluent Pressure Coefficient Distribution Results Around Prolate Spheroidal Body

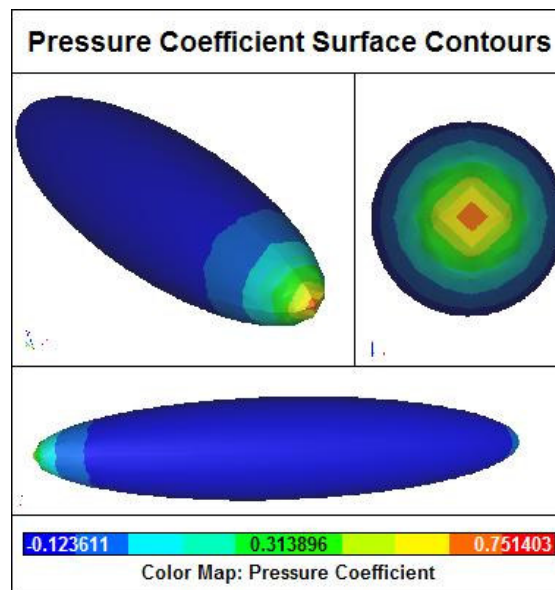


Figure 6.13: Symlab Pressure Coefficient Distribution Results Around Prolate Spheroidal body

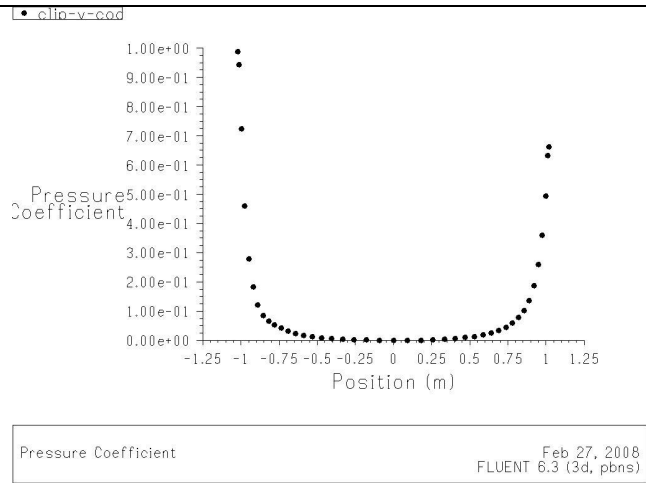


Figure 6.14: Fluent Graphical Pressure Coefficient Distribution Around Prolate Spheroidal Body

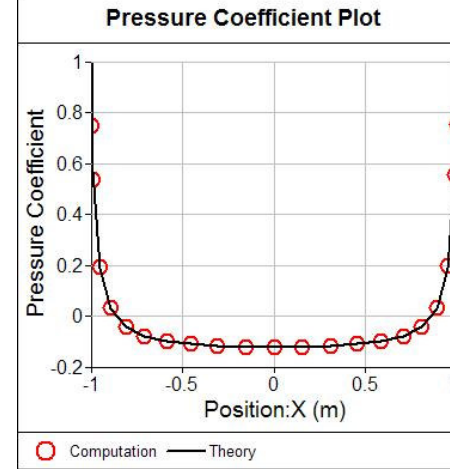


Figure 6.15: Symlab and Theoric Graphical Pressure Coefficient Distribution Around Prolate Spheroidal Body

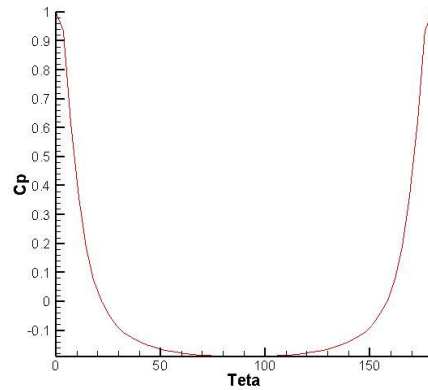


Figure 6.16: In-House Code Graphical Pressure Coefficient Distribution Around Prolate Spheroidal Body

This time in both Fluent and Symlab curves X-axis denotes proportional location of node point relative to the center of the sphere. Because of the additional option in Symlab theoretical datas are given with red circles in Figure (6.15) which ease the comparison between Symlab result and theoretical values. As you see from the different graphs, the general slope of the Cp function is similar. Unfortunately, they have small differences. Reasons of the small difference are briefly summarized in the previous subsection.

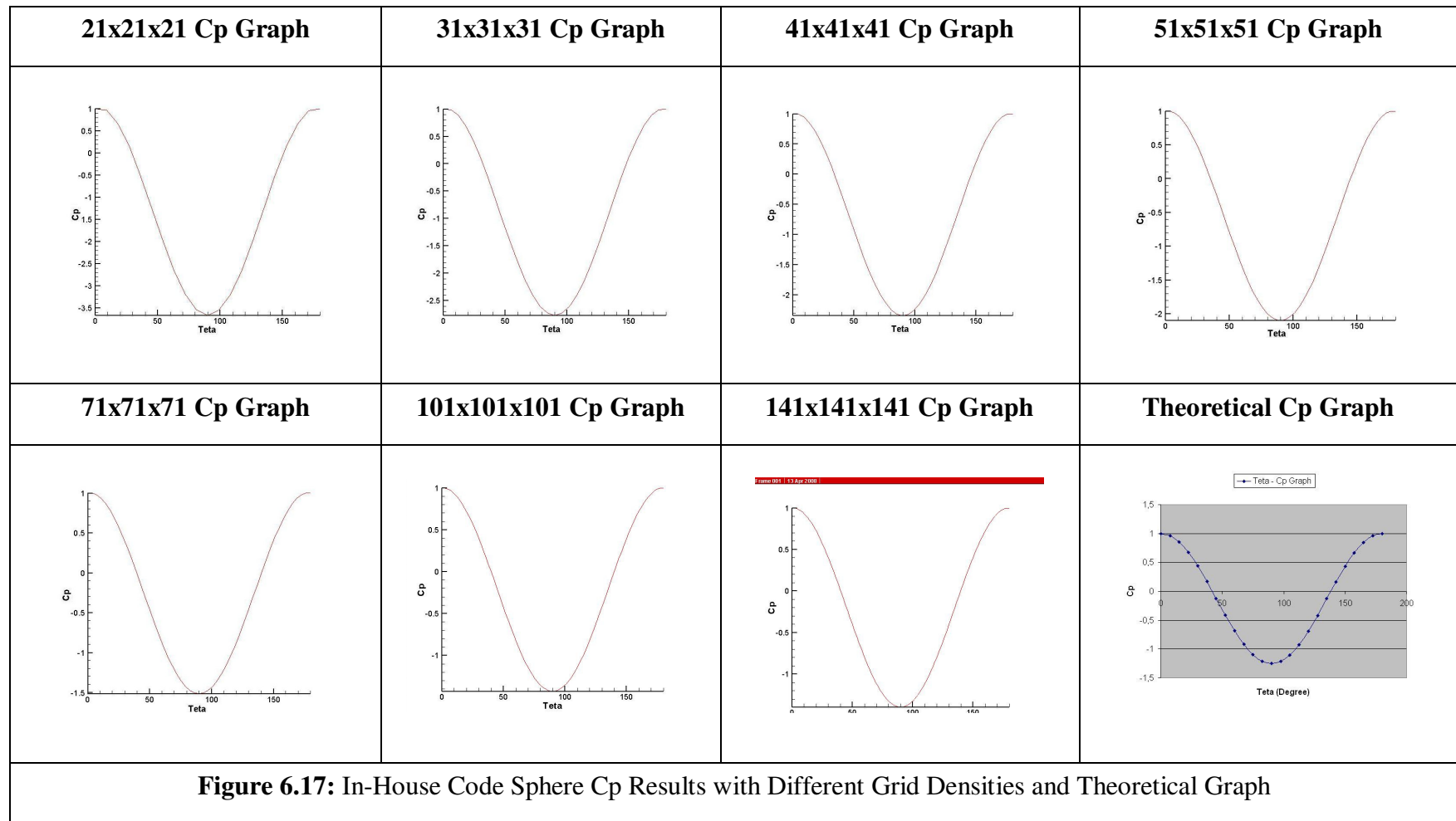
6.3 Comparison of In House Code Results for Different Grid Densities

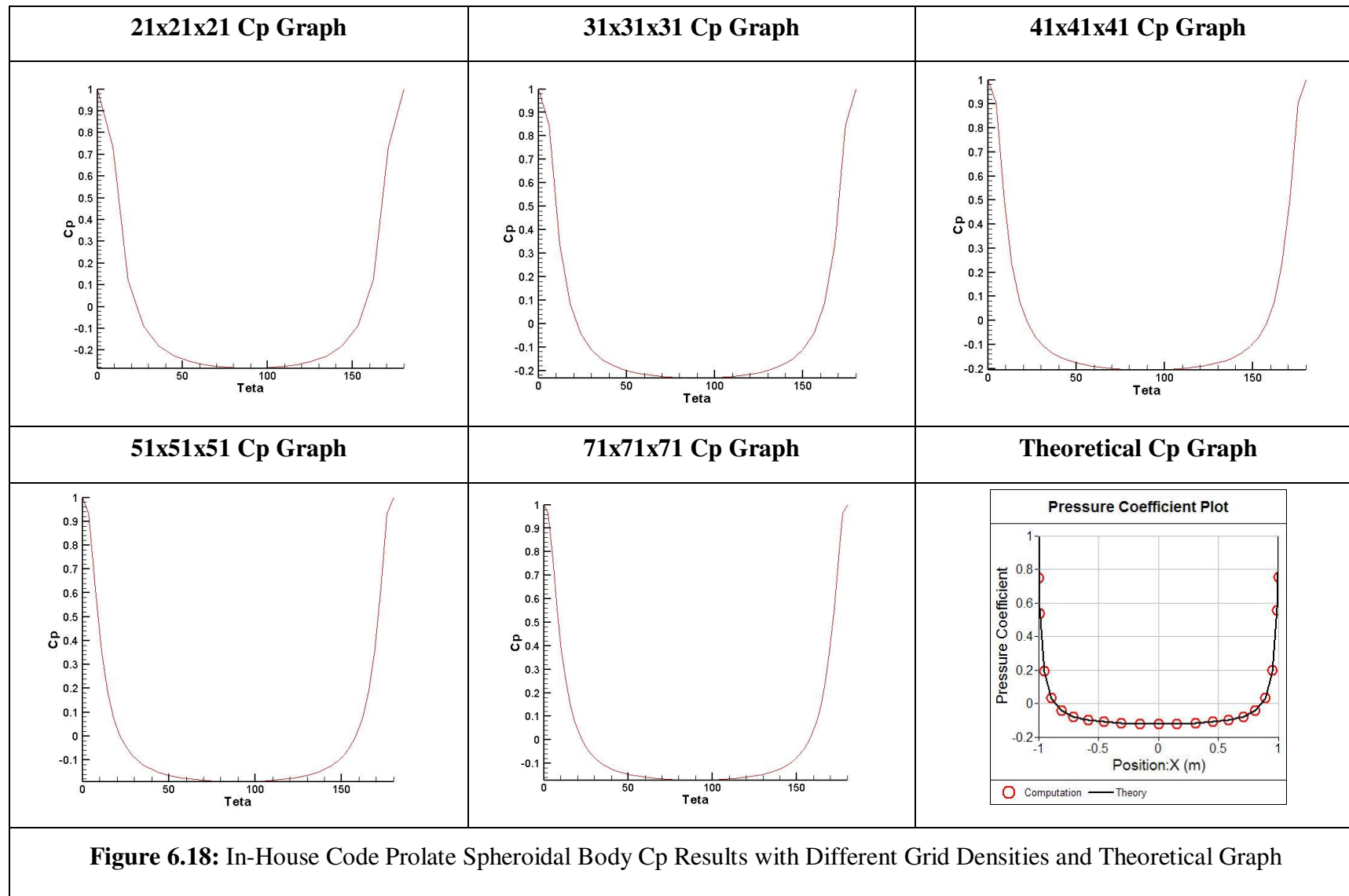
In present dissertation last comparison is made between different grid density results of in house code. Figure (6.17) presents Cp distribution graphics of sphere with different grid trials. According to Figure 6.17, It has been proven that finer grid schema results in more approximate output to teorical results. Remember that minimum Cp value on sphere surface is -1.25 and -1.1 on prolate spheroidal body. On the other hand, using finer grid schema extents computational time. If physical space for a sphere body is solved for potential flow with different grid densities, results are shown in Table (6.1);

Table 6.1: Sphere Flow Comparison for Different Grid Densities

	Grid Dimension	Node Number	Solution Time (seconds)	Error (%)
Experiment 1	21x21x21	9261	12	107.1
Experiment 2	31x31x31	29791	126	66.7
Experiment 3	41x41x41	68921	663	48
Experiment 4	51x51x51	132651	2463	36.4
Experiment 5	61x61x61	226981	7054	22
Experiment 6	71x71x71	357911	18323	11.6
Experiment 7	101x101x101	1030301	108105	7.6
Experiment 8	141x141x141	2803221	616202	5.8

Figure (6.18) presents Cp distribution graphics for Prolate Spheroidal Body with different grid trials. Graphs of node number versus solution time and error versus node number are given in Appendix-B.1 and Appendix-B.2. Analysis are executed on computer which has a pentium 4 processor and 512 megabyte DDR RAM.





7. CONCLUSIONS

In this thesis Fortran Codes are developed that form three dimensional control volume, grid and solve potential flow equation for a sphere and a 3-D prolate spheroidal body. Post-processing step is done with Tecplot program which is an extensive postprocessing software that enables visualization and plotting for various shapes.

Nowadays, there are plenty of programming languages to calculate results for scientific computing. Fortran is one of the software tools for obtaining the results. However, it only gives the outcome in numerical order even it is arranged in matrix form. Figure out the trouble with observing the data is a gruelling process. Therefore, it is determined that, to assign the values to the right place in physical space is a necessity to gain time during the supervision time. This is the main reason for employing a post-processor software like Tecplot for Fortran codes output data. As a consequence, right connection between the two different programs is successfully achieved. Establishment of connection between Fortran and Tecplot with arrangement of Fortran code output data assumed as a first achievement of the thesis.

Next achievement, to obtain form-fitted and hexagonal shaped grid type within the specified control volume is provided in both spherical coordinate system and prolate spheroidal coordinate system. Form-fitted grid allowed us to simulate the inner borders with increased accuracy. On the other hand, hexagonal shaped grid schema removes the necessity of interpolation during the calculation phase. Both applications result in reduction in code length and additional calculation time. Moreover, it has been found that selection of prolate spheroidal coordinates brings further advantages like grid clustering and far field span increment. Presence of sinus hyperbolic function in eta (η) direction results in non-uniform mesh distribution in the physical space. When increment is executed only in eta (η) direction (θ and Φ values are same), distance between the node point and the origin represent a hyperbolic curve while approaching to infinity. Therefore it results in finer grid close to the inner body and coarser grid

close to the outer body. This is especially very advantageous in cases where an external flow is investigated and mesh spacing in far fields is much less important than mesh spacing in the center of the domain.

In the present dissertation another achievement is about the density of the mesh. It has been proven that finer grid schema results in more approximate output to teorical results. On the other hand, using finer grid schema extents computational time. Despite extention in computational time, CFD analysis scheme has to be made with a finer grid as possible as it can be.

Last and the major achivement is, the consistency of in-house code results and teoretical results are achieved for the heat conduction and the potential flow problems although considered bodies are not suitable for the analysis in the Cartesian coordinate system. Presented results which are the output of the in-house code are very approximate to the commercial code and teoretical results. Comparative presentation of all obtained results are given in Appendix C. It has been showed that written codes for a 3-D incompressible potential flow run successfully. So, it has been considered that present thesis solution methodology which is aspired to establish the basic logic and to utilize the computer technology in most efficient manner will be the lighthouse for the further similar investigations and nowadays problems that will require numerical solutions of sophisticated differential equations.

REFERENCES

- Anderson, J.D. Jr.**, 1995. Computational Fluid Dynamics The Basics with Application, R.R. Donneley & Sons, New York.
- Blazek, J.**, 2001. Computational Fluid Dynamics, Principles and Applications, Elsevier, Oxford.
- Chesnakas, C.J. and Simpson. R.L.**, 1997. Detailed Investigation of the Three-Dimensional Separation About a 6:1 Prolate Spheroid, *American Institute of Aeronautics and Astronautics Journal -AIAA-*, **Volume 35**, **No. 6**, 990-999.
- Coirier, W.J. and Powell, K.G.**, 1995. An Accuracy Assessment of Cartesian Mesh Approaches for the Euler Equations, *J. Computational Physics* (**117**); 121-131.
- Deng, G., Piquet, J. and Queutey, P.**, 1990. Navier-Stokes Computation of Vortical Flows, *AIAA Journal*, **90**, 1628.
- Ferziger, J.H. and Peric, M.**, 2002. Computational Methods for Fluid Dynamics, Springer-Verlag, New York.
- Gee, K., Cummings, M. and Schiff, L.**, 1992. Turbulence Model Effects on Separated Flow About a Prolate Spheroids, *AIAA Journal*, **Vol 30**, **No.3**, 655-664.
- Goody, M.C., Simpson, R.L. and Chesnakas, C.J.**, 2000. Separated Flow Surface Pressure Fluctuations and Pressure-Velocity Correlations on Prolate Spheroid, *AIAA Journal*, **Volume 38**, **No.2**, 266-274.
- Gören, Ö.**, 2007. Hydrodynamics of floating bodies lecture notes.
- Habermann, R.**, 1983 Elementary Applied Partial Differential Equations with Fourier Series and Boundary Value Problems, Prentice-Hall, New Jersey.
- Hirsch, C.**, 1991. Numerical Computation of Internal and External Flows, John Wiley & Sons, Chichester.
- Hoffmann, K.A., Chiang. S.T.**, 1989. Computational Fluid Dynamics for Engineers, Engineering Education System.
- Kim, S.E., Rhee S.H. and Cokljat D.**, 2003. High-Incidence and Dynamic Pitch-Up Maneuvering Characteristics of a Prolate Spheroid, *24th Symposium on Naval Hydrodynamics*, Fukuoka, Japan, July 8-13.
- Kim, S.E. and Patel V.C.**, 1991. Flow Separation on a Spheroid at Incidence: Turbulent Flow, Process, *Viscous Fluid Dynamics in Ship and Ocean Technology Colloquium 91*, Osaka, Japan.
- Knupp, P., and Steinberg, S.**, 1993. The Fundamentals of grid generation, Boca Raton, CRC Press.

- Lomax, H., Pulliam, T. and Zingg, D.W.**, 1999. Fundamentals of Computational Fluid Dynamics, NASA Ames Research Center.
- Meier, H.U., Kreplin, H.P., Landhausser, A., and Baumgartem, D.**, 1984. Mean Velocity Distribution in Three-Dimensional Boundary Layers Developing on a 6:1 Prolate Spheroid with Natural Transition, *DFVLR-Data Report International Bulletin*, **222-84**, A11.
- Meier, H.U., Kreplin, H.P. and Landhausser, A.**, 1986. Wall Pressure Measurement on a 6:1 Prolate Spheroid in the DFVLR Low Speed Wind Tunnel, *DFVLR Data Report International Bulletin*, **222-86**, A04.
- Mironer, A.**, 1979. Engineering Fluid Mechanics, Mc Graw-Hill, New York.
- Moon, P. and Spencer, D. E.**, 1988. Field Theory Handbook: Including Coordinate Systems, Differential Equations and Their Solutions, Springer-Verlag, New York.
- Owczarek, J.A.**, 1968. Introduction to Fluid Mechanics, International Textbook Company, Pennsylvania
- Panton, R.L.**, 1984. Incompressible Flow, John Wiley & Sons, New York.
- Plewa T., Linde T.J. and Weirs V.G.**, 2003. Adaptive Mesh Refinement, Theory and Applications, Springer, Berlin.
- Rhee S.H. and Hino , T.**, 2000. Computational Investigation of 3D Turbulent Flow Separation around a Spheroid using Unstructured Grid Method, *Journal of the Society of Naval Architects of Japan*, **Volume 188**, 1-9.
- Sabuncu, T.**, 1962. Some Predictions of the Values of the Wave Resistance and Moment Concerning the Rankine Solid under Interfacial Wave Conditions, Norwegian Ship ModelExp. Tank Publ. **No.65**.
- Thomas, B.G. and Finney, L. R.**, 1998. Calculus and Analytic Geometry, Addison-Wesley Publishing Company, Reading, Massachusetts.
- Thomson, J.F., Warsi, Z.U.A. and Mastin, C.W.**, 1985. Numerical Grid Generation: Foundation and Applications, North-Holland: Elsevier Science Publication Company, New York.
- Vatsa, V.N., Thomas, J.L. and Wedan, B.W.**, 1989. Navier-Stokes Computation of a Prolate Spheroid at Angle of Attack, *Journal of Aircraft*, **Volume 26**, **No.11**, 986-993.
- Versteeg, H.K. and Malalasekera, W.**, 1995. An Introduction to Computational Fluid Dynamics, John Wiley & Sons, New York.
- Wetzel, T.G., Simpson, R.L. and Chesnakas, C.J.**, 1998. Measurement of Three-Dimensional Crossflow Separation, *AIAA Journal*, **Volume 36**, **No.4**, 557-564.
- White, F.M.**, 1991. Viscous Fluid Flow, McGraw-Hil, New York.
- White, F.M.**, 1995. Fluid Mechanics, McGraw-Hill, Boston.
- Zheng, X., Liao, C., Liu, C., Sung, C.H., and Huang, T.T.**, 1997. Multigrid Computation of Incompressible Flows Using Two-Equation Turbulence Models: Part I –Numerical Method, *Journal of Fluids Engineering*, **Volume 119**, 893-899.

APPENDIX A

Theoretical Pressure Coefficient Variation

Table A: Angle-Theoretical Pressure Coefficient Variation Datas

θ (degree)	$\sin \theta$	$V_s = \frac{3}{2} V_\infty \sin \theta$	$C_p = 1 - \frac{V_s^2}{V_\infty^2}$
0	0.000	0.000	1.000
7.5	0.130	0.196	0.962
15	0.259	0.388	0.849
22.5	0.382	0.574	0.671
30	0.500	0.750	0.438
37.5	0.608	0.913	0.167
45	0.707	1.060	-0.124
52.5	0.793	1.190	-0.415
60	0.866	1.299	-0.686
67.5	0.924	1.385	-0.920
75	0.966	1.449	-1.099
82.5	0.991	1.487	-1.211
90	1.000	1.500	-1.250
97.5	0.991	1.487	-1.212
105	0.966	1.449	-1.100
112.5	0.924	1.386	-0.922
120	0.867	1.300	-0.690
127.5	0.794	1.191	-0.419
135	0.708	1.062	-0.128
142.5	0.610	0.915	0.163
150	0.500	0.752	0.435
157.5	0.384	0.576	0.668
165	0.260	0.390	0.848
172.5	0.132	0.198	0.961
180	0.000	0.000	1.000

APPENDIX B

Node Number, Error, Computational Time Graphs

Node Number/Error

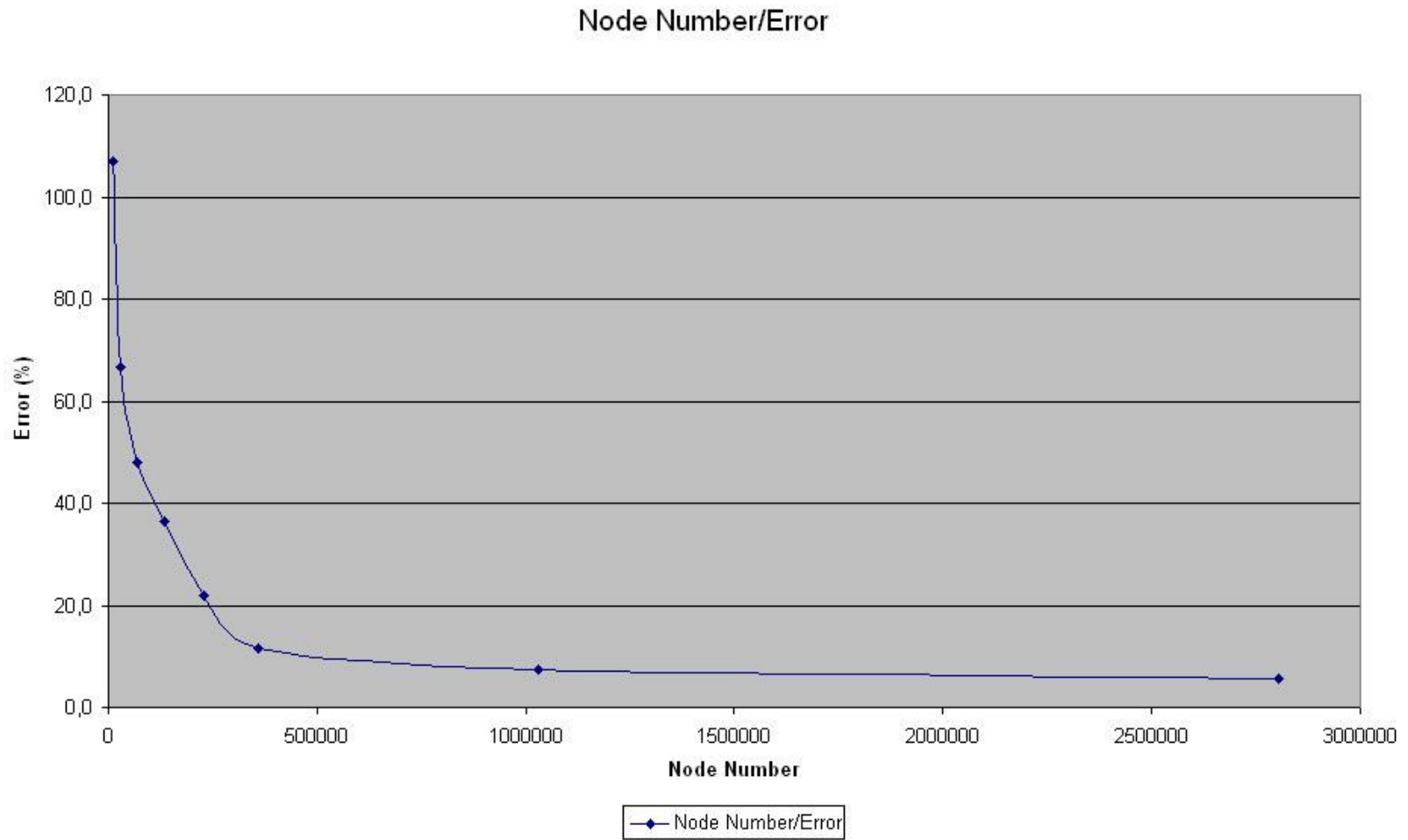


Figure B.1: Node Number/Error Graph

Node Number/Computational Time

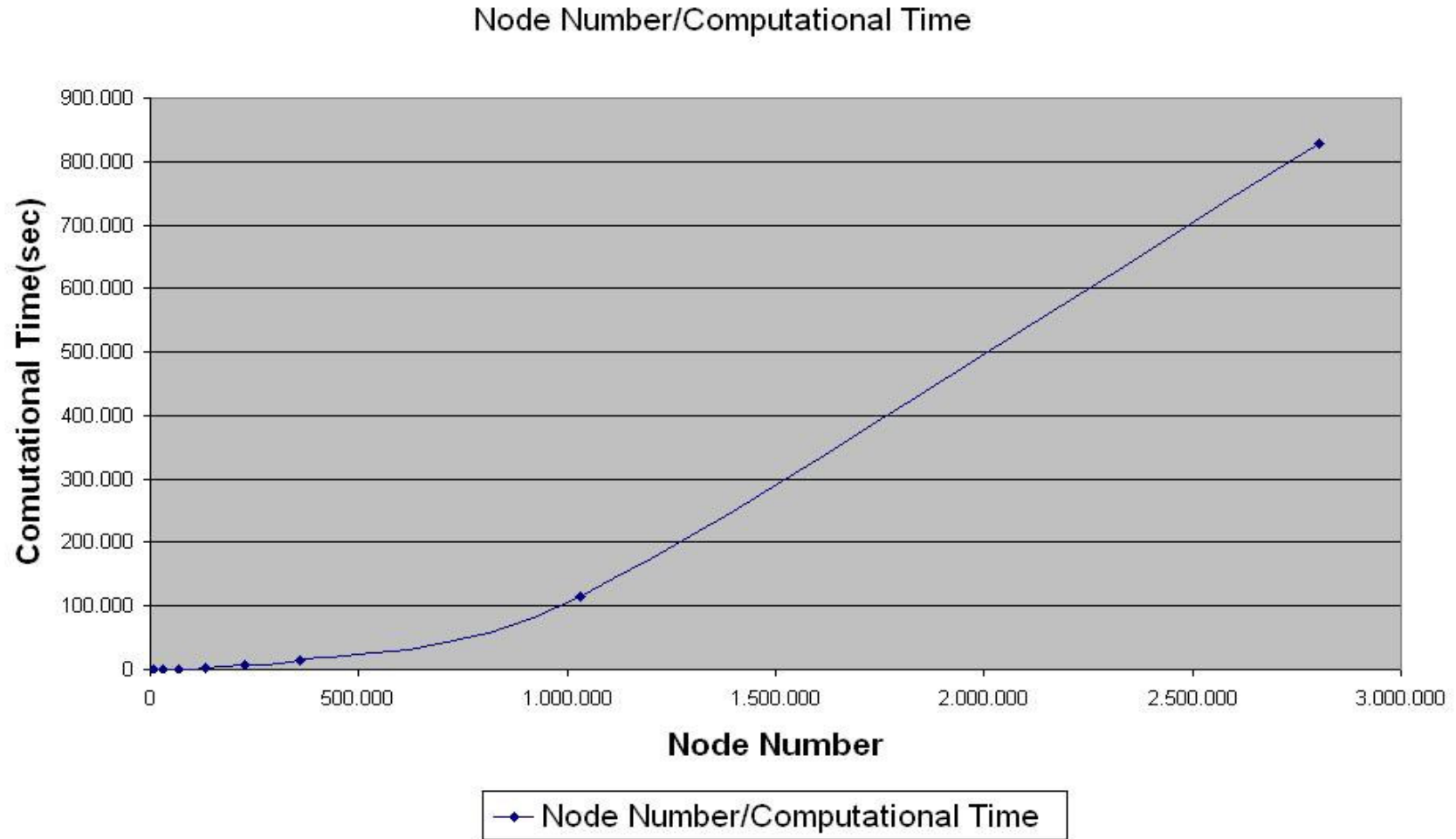


Figure B.2: Node Number/Computational Time Graph

APPENDIX C

Comparative Cp Presentation of Sphere Results

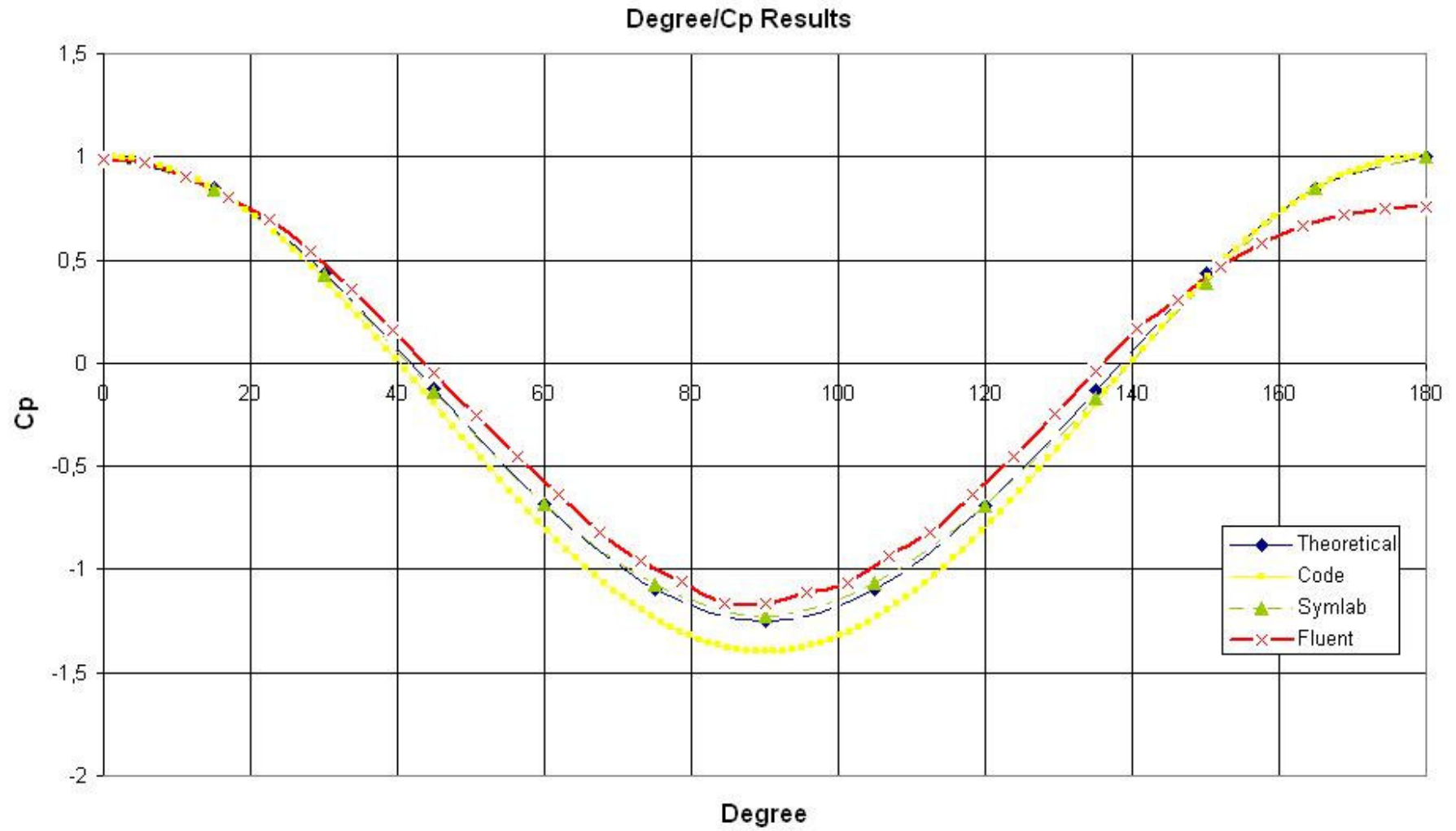


Figure C: Degree/Cp Results of Sphere

CURRICULUM VITAE

Onur Ölmez. is born in Kırıkkale, on the 5th of May 1981, and he is son of Kemal Ölmez who is the trade manager of MKE (Mechanical and Chemical Industry Corporation) Silahsan A.Ş at Kırıkkale and Serpil Ölmez who is an accountant. He finished his elementary School and High School in Kırıkkale. He won both Government Fund and Science Lycee Examination then started Sivas Science Lycee as boarding student. In 1999 he took admission to Istanbul Technical University Naval Architecture and Ocean Engineering Faculty and in 2004 he graduated as Naval Architect and Ocean Engineer.

After graduation in 2004, he started in FİGES A.Ş as a CAD/CAE (Computer Aided Design/Computer Aided Engineering) Engineer at Research & Development Department. His familiarity to Finite Element Softwares like Ansys, Ansys/Workbench and to Finite Difference/Volume Softwares like Ansys/CFX, Fluent are come from gained experience of executed analysis for projects in Figes A.Ş.

One year later in 2005, he resigned from Figes A.Ş and started working at SSM (Undersecretariat for Defense Industries) Quality, Test and Certification Department. Meanwhile, he took admission as a graduation student in aforementioned faculty. From 2005, he has been working as a Government Quality Assurance Representative for Undersecretariat for Defense Industries to control the advancement of the production progress and the quality topics stated in various navy projects in different shipyards.